MAPPING THE MARGIN OF THE BARNES ICE CAP USING SAR IMAGERY

NAOMI SHORT

INFORMATION TO USERS

Mapping the Margin of the Barnes Ice Cap using SAR Imagery

by

Naomi Short

A thesis submitted to the

School of Graduate Studies

in partial fulfillment of the

requirements for the degree of

Master of Science

Department of Geography

Memorial University of Newfoundland

1999

St. John's   Newfoundland

Abstract

The limit of active ice, accurate to within 49 m, is extracted from SAR imagery of the Barnes Ice Cap, using a sequence of image speckle filtering, image texture analysis, supervised image classification, image segmentation and edge detection. Overall classification accuracies of the ice marginal environment are between 42 and 53%. Despite misclassification of some proglacial landforms it is possible to detect the limit of active ice as these surfaces are separated from the ice cap by supraglacial debris cover, an elevated ice cored debris ridge and perennial snowbeds.

Comparisons of opposing look angles reveal that 'downglacier' illumination produces the highest classification accuracies of ice marginal features and debris covered ice surfaces, whereas illumination from an off-ice perspective, looking 'upglacier', is found to produce higher classification accuracies for proglacial surfaces. Comparisons of standard and fine mode imagery conclude that 25 m spatial resolution yields higher classification accuracies than 8 m spatial resolution. Quantitative analysis of surface roughness demonstrates that the dominant grain size of surficial materials is the best method for relating surface cover to radar brightness.

Second order texture measures mean, homogeneity and correlation are found to be effective variables for maximum likelihood classification of ice marginal SAR imagery. Texture window size should be as large as the smallest feature to be identified, in this case approximately 85 x 85 m for the mean and homogeneity measures and 185 x 185 m for the correlation measure.

Acknowledgments

Table of Contents

List of Tables

List of Figures

List of Plates

List of Symbols

λ : Wavelength

μ : Mean

$\theta_.$: Incidence angle

π : 3.14

σ : Variance

δ : Displacement or spatial function

β° : Radar brightness

$[]^T$: Transpose of matrix

$[]^{-1}$: Inverse of matrix

$()^{det}$: Determinant of matrix

A2 : Scaling gain value

A3 : Offset

CP : Central pixel in window

Damp : Dampening factor

g : row in grey level cooccurrence matrix

h : column in grey level cooccurrence matrix

(g, h) : Grey level cooccurrence matrix element

p(g, h) : Normalised grey level cooccurrence matrix element

G_g : Grey level

h : Root mean square of surface height variation

J : Jeffries-Matusita separability

L : Correlation length

M : Mean vector

MP : Probability of class membership

Pi : a priori probability

R : speckle filter output

Sh : Standard deviation of surface height

Si : covariance matrix

Sp : standard deviation of surface height slope

T : absolute distance of centre pixel to neighbours

List of Abbreviations and Acronyms

ADRO : Application Development and Research Opportunity
a.s.l : above sea level
DN : Digital number
dB : Decibels
DEM : Digital elevation model
ELA : Equilibrium line altitude
ERS-1 : European Remote Sensing Satellite
ERTS : Earth Resources Technology Satellite
F1 : Fine mode one of RADARSAT SAR
GCP : Ground control point
GLCM : Grey level cooccurrence matrix
GPS : Global positioning system
HRV : High resolution visible
ICDR : Ice cored debris ridge
KHAT : Kappa statistic
TM : Landsat Thematic Mapper
L&A : Løken and Andrews moraines
MLC : Maximum likelihood classifier
NASA : National Aeronautics and Space Administration
NTS : national topographic series
RMS : residual mean square
SAR : Synthetic Aperture Radar
SDC : Supraglacial debris cover
SPOT : Satellite pour l'Observation de la Terre
S4 : Standard mode four of RADARSAT SAR
UTM : Universal Transverse Mercator

1. Introduction

This research examines the issue of ice margin mapping using spaceborne radar data. The topic of ice margin placement is explored and the mechanics of radar image mode selection and image processing procedure are investigated.

Ice masses form a vital component of global climate. They contain large volumes of the earth's freshwater resources and their presence is a controlling factor in global atmospheric circulation. Ice mass shrinkage as a function of global warming has important implications both for sea level rise and global circulation (Houghton *et al.*, 1996). In order to model global climate and glacio-eustasy the contributory changes of ice mass balance must be quantified. Fluctuations in mass balance are manifested primarily as a raising or lowering of an ice surface, and an advance or retreat of the ice front. Thus accurate mapping of ice front position forms a part of any ice mass monitoring program.

Observations of ice front position have traditionally been carried out by manual survey and aerial photography. These methods are expensive, time consuming, limited in scale of application and constrained by weather conditions. Spaceborne remote sensing offers an alternative method of monitoring ice margins, which can be applied at a large scale, in remote areas, and at frequent time intervals.

RADARSAT synthetic aperture radar (SAR) is an active microwave satellite sensor that was launched in 1995. It transmits pulses at the C-band wavelength of 5.6 cm and has horizontal-like polarization. It offers a range of beam modes with spatial resolutions between 8 m and 100 m, and look angles between 20° and 60°. As an active remote sensing system, data collection is independent of solar illumination. This is especially important for the regular imaging of ice masses at high latitudes which experience polar night. The wavelength of the radar pulse allows penetration of rain and cloud cover and means that image acquisition schedules are reliable. These advantages of all-time and weather independent imaging make radar imagery particularly suitable for ice mass monitoring (Massom, 1991).

Radar data contain information about surface roughness, relief, moisture content and the dielectric properties of the surface materials at a relatively fine spatial resolution. Despite many years of radar image acquisition over ice marginal environments there is no scientific agreement on the best sensor mode to be employed, and no standard method of image analysis and ice margin extraction. This research seeks to address this disparity and, through the development of a methodology, to broaden the application of spaceborne synthetic aperture radar (SAR) in contemporary glacial environments.

One of the objectives of remote sensing is to perform mapping tasks automatically and hence, convert data into information in an efficient and timely manner

(Jensen, 1996). Image classification methods assign image pixels to landcover classes of interest in order to produce thematic maps, but these have typically been designed for use with multispectral imagery. As radar data are monoband data, an alternative strategy for the development of a classification method is required. Image texture analysis examines the spatial relationship of pixel values rather than the individual pixel values. Texture images are derived from the original image using texture measure algorithms to quantify the spatial variation in pixel values. Texture images may be used as input to a classification method and therefore provide a suitable automated technique of radar image analysis.

The purpose of this research is to develop an automated technique of SAR image analysis for an ice marginal environment, from which an accurate map of ice extent can be produced. The technique is developed for a section of the margin of the Barnes Ice Cap in the Canadian Arctic. In addition to the ice cap margin itself the study examines proglacial landforms, their surface characteristics in terms of radar parameters, and the capabilities of SAR for mapping the proglacial zone.

The background chapter introduces the context of ice margin mapping, the associated glacial geomorphology, and describes the specific challenge of identifying the active ice margin. The nature of radar data is explained and the approach of remote sensing to glaciology and its progress to date are outlined. The concepts of image processing for radar image analysis and thematic map production are described. The third

chapter summarizes the problems specific to the remote mapping of ice margins and states the objectives of this thesis. The Barnes Ice Cap study area is presented in chapter four. The methodology employed in the fieldwork and the image analysis is described in chapter five. The results of the field investigations are given in chapter six and the image processing results are given in chapter seven. Chapter eight discusses the results, the success of the methodology, and makes comparisons with other research. Chapter nine concludes with a summary of the achievement of the research objectives and recommendations for further studies.

2. Background

The remote mapping of a glacial environment using SAR imagery requires an understanding of glaciology in the context of radar image interpretation and classification. This chapter presents the fundamentals of each of these topics. In the first section the glaciology and the geomorphology of the ice marginal environment, with specific reference to the Barnes Ice Cap study area are presented. The second section reviews the current literature on glaciological applications of remote sensing. The third section explains the nature of synthetic aperture radar (SAR) data and gives examples of how the glacial environment responds to SAR. The fourth section is a review of ice margin mapping applications using SAR. The creation of thematic maps from radar data requires extensive image processing. This chapter provides explanations of image processing procedures. Section five describes the concept of radar noise, known as 'image speckle' and the methods used to remove this noise. Section six reviews the concept of image texture and the methods for extraction of texture from radar imagery. Section seven presents the various procedures of image classification and the creation of maps from images. Section eight explains image edge detection and how this is used to extract linear or boundary features of interest from an image.

2.1 Glaciology

The mapping of ice front position is a component of monitoring overall ice mass changes. This section explains the concept of glacier mass balance and briefly reviews the role of remote sensing in monitoring mass balance. The second subsection presents

basic ice margin dynamics and describes the margin of the Barnes Ice Cap. The final subsection describes the glacial geomorpholgy of the proglacial zone with specific focus on the conditions prevalent in the Canadian Arctic.

2.1.1 Glacier mass balance

Glacier mass balance is the concept used to describe the balance between annual ice mass gains (accumulation) and losses (ablation) (Hambrey, 1994). Changes in ice volume are manifested as a raising or lowering of the ice surface, and/or a retreat or advance of the ice front. Changes in ice thickness may be measured using ground penetrating radar, radar altimetry or manual survey of ice surface transects. Movement of the ice front may be monitored by manual survey or by remote observation. Proxy measures for monitoring mass balance have been developed which use shifts in the equilibrium line altitude (ELA) to quantify ice volume changes (Østrem, 1975; Orheim and Lucchitta, 1987). The ELA is the divide between the accumulation zone (the area where there is net annual gain of ice primarily through precipitation and refreezing) and the ablation zone (the area that experiences net annual ice mass loss through melt and iceberg calving) at the end of the melt season (Paterson, 1994). The ELA represents where the glacier is a constant thickness as ice input balances ice loss. The extent of the accumulation zone is identified in imagery as the lower limit of the snowpack at the end of the ablation season, referred to as the 'snowline'. The end of melt season snowline is sometimes used as the proxy for the ELA (Krimmel and Meier, 1975; Paterson, 1994). There has been some doubt expressed about this method particularly for ice masses with

a significant portion of their accumulation through the formation of superimposed ice (Parrot *et al.*, 1993) and this technique was rejected by Jacobs *et al.* (1993) for the Barnes Ice Cap for this reason. Moreover, snowpack extent is highly variable from year to year, therefore, ice thickness and ice front position are more reliable and robust indicators of long term ice volume changes. In light of these two factors this research focuses solely on monitoring the position of the ice front.

It has been suggested that for glacier mass balance studies, the ice front should be placed with an accuracy of 50 to 75 m (Adam *et al.*, 1997). Such accurate mapping of the ice front requires recognition of the characteristics of the marginal ice and the area directly in front of the ice mass, the proglacial zone. Where the ice front is obscured by debris an examination of the local geomorphology is necessary to identify the extent of the ice.

2.1.2 Ice margin morphology

Ice margins occur in many different forms as a function of the subglacial surface combined with the internal glacial dynamics and sediment transport mechanisms. The type of flow and the nature of the sediment in transport will characterize the morphology of the ice surface and front. Flow is broadly the result of gravity forces which cause the ice to spread by the process of creep under its own weight (Drewery, 1986). For ice surface morphology longitudinal variations in velocity are of interest. Two flow states are possible and these are extending and compressing flow (Nye, 1957). Extending flow, or

thinning, occurs as a result of the ice accelerating and causes crevassing. Ice acceleration is due to either, an increase of ice mass in the accumulation area, or an increase in the gradient of the subglacial surface. Glaciers confined to a channel demonstrate extending flow on the outside of bends and where side streams join the glacier. Compressing flow is due to deceleration of the ice and is manifested as bulges and compression ridges on the ice surface. Compressing flow occurs where the subglacial surface gradient decreases, toward the ice margin where ablation causes ice mass loss, on the inside of valley glacier bends and where a confined channel widens (Hambrey, 1994).

Compressing flow permits the flow of debris-laden basal ice up toward the ice surface along shear planes. This debris is exposed and released by ablation at the surface, where it contributes to the volume of supraglacial material and eventually to the formation of moraines. Other contributors of supraglacial debris are nunataks and valley sides. Lateral and medial morainic material may obscure the ice surface both upstream and where the debris becomes concentrated toward the margin. Figure 2.1 illustrates the paths of debris transport within a glacier and how englacial and basal debris becomes supraglacial debris at the margin of a glacier. Supraglacial debris causes ice margins to be significantly different from clean upglacier ice and snow.

Also shown in Figure 2.1 are the formation processes of tills. Tills are one of the final deposits of glacially transported debris. These sediments are deposited by the direct action of ice, either in the process of ice melt, producing meltout till or by accretion

under a moving glacier, producing lodgement till. Tills modified by post-depositional processes are referred to as flow and deformation tills. Tills are key components of the deglaciated landscape. If they were deposited subglacially by active ice they may contain evidence of ice flow direction such as drumlins, flutes or lineations (Hart, 1995), and their composition controls local sediment supply and consequently contemporary geomorphological processes. Examination of till composition is a key methodology in reconstructing ice dynamics of previous glaciations (Dreimanis, 1971).
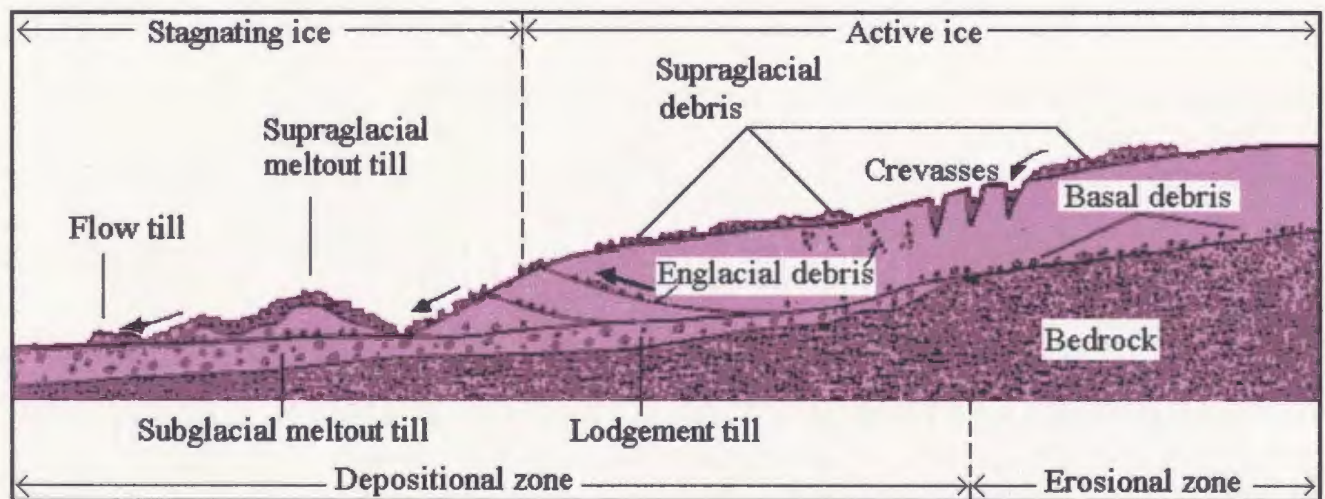
(Source: Modified from Hambrey and Alean, 1992)

Figure 2.1 Longitudinal profile through a retreating valley glacier

In addition to debris, meltwater is an important factor in ice margin morphology. Supraglacial meltwater channels vary from very shallow and narrow, in the order of centimeters, to deeply incised, with pools and moulins with dimensions of meters. Patterns of meltwater flow will not only modify the form of the ice but will also influence the distribution of supraglacial sediment. Supraglacial streams may deposit or erode debris from the ice surface depending on the flow regime, resulting in cleaner or debris

covered surfaces along the edges of the channel. Where meltwater collects at the margin in topographical depressions, glaciolacustrine environments develop. Lacustrine ice margins may be in cliff form, with ablation loss occurring predominately through iceberg calving, or floating ice lobes which thin distally due to basal melt and surficial ablation.

Land based ice margins produce a wide variety of ice margin forms. These range from gentle gradient ice fronts to sheer ice cliffs. Supraglacial debris may be present or absent due to local sediment supply and glacial transport mechanisms. Lengthy ice margins such as the edges of ice sheets, as opposed to confined valley glacier snouts, are more complex due to spatial variations in the local topography and substrate geology, mass balance fluctuations and localized ice flow patterns.

2.1.3 Ice cored moraines of the Barnes Ice Cap

The active processes at the Barnes Ice Cap margin have been the source of some debate on account of the presence of a large and dominant ice cored moraine. Goldthwait (1951) and Hooke (1973) have studied the moraines of the Barnes Ice Cap and provide two theories of formation which include ice shear planes, phases of retreat and advance and the development of perennial snowbeds along the margin. The presence of this ice cored moraine has important implications for the mapping of the ice margin.

The focus of this study is the delineation of the currently active ice margin. The active ice margin is defined here as the distal limit of ice that is still adjoined to and supplied by flow from the main ice mass. Ice cored moraines are separated from the main

body of ice by a trough containing debris and typically a stream, see Figure 2.2a. These are therefore considered to be detached from the ice mass and distal to the present active ice margin. In contrast, a covering of supraglacial debris merely overlies the marginal ice and does not segregate blocks of ice from the main body, the structure is shown in Figure 2.2b. It is thus still possible for the main ice mass to supply the underlying ice and so the active ice margin is judged to lie beneath the supraglacial debris cover. The limit of active ice is shown in Figure 2.2 a and b to be just inside the actual extent of the glacier ice. This is in accordance with the division between active and stagnant ice as defined by Hambrey and Alean (1992) and shown in Figure 2.1. On account of confusion at the ice margin it is necessary to examine both the ice cap itself and the landforms of the adjacent land surface, in order to determine the exact position of the limit of active ice, as this is considered here to be the ice margin.
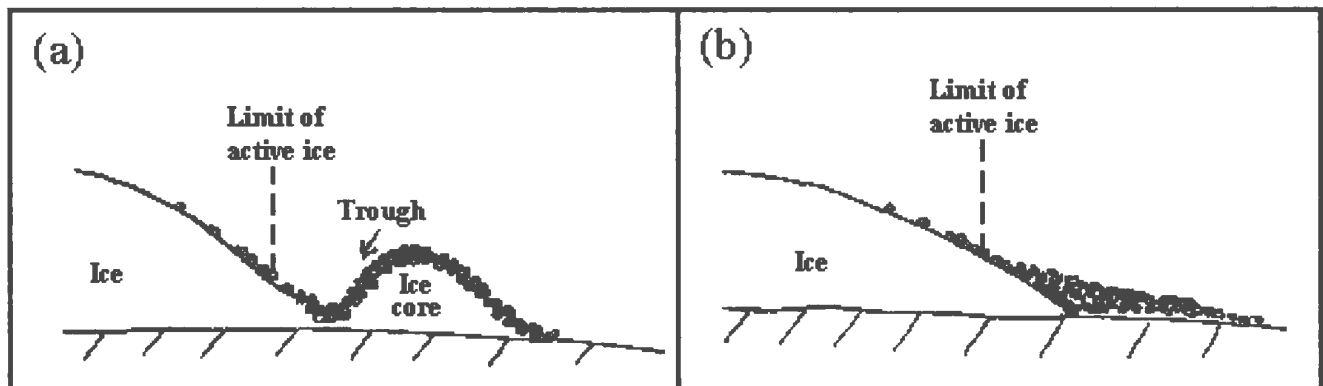
Figure 2.2 (a) Margin with ice cored moraine (b) Margin with supraglacial debris cover

2.1.4 The proglacial zone

The proglacial zone is the land area directly adjacent to the ice front. It has distinctive geomorphology on account of the unique interactions between ice, water and

sediments. The deglaciated terrain is either a glacial erosion surface such as exposed bedrock, or a combination of glacial depositional features and glaciofluvial sediments. The present day landscape is a result of the regional geology, the thermodynamics of the glacier that covered the area (Sugden, 1978; Shaw, 1994) and contemporary geomorphic processes. The Barnes Ice Cap is located on Baffin Island in the Canadian Arctic. The Canadian Arctic Archipelago is typically characterised by cold-centered arctic ice caps. Cold based glaciers have no significant basal meltwater and so basal sliding is impossible, thus capacity for basal erosion and debris transport is limited. On account of this it is common for periglacial surfaces and landscapes of previous glaciations to be preserved under a cold-centered ice cap. The deglaciated terrain is characterised mainly by residuum and colluvium with a notable absence of streamlined and ice molded structures (Dyke, 1993). Residuum is rubble or felsenmeer with in-situ weathered boulders, the angular clasts indicative of periglacial weathering rather than subglacial erosion. Colluvium is fine grain size material that is derived from movement and vertical accretion of components of residuum; it collects in depressions and may demonstrate tundra patterned ground characteristics.

The cold ice cap center may besurrounded entirely, or in part, by a warm-based periphery. Meltwater activity is constrained to the warm-based periphery where it creates erosional or depositional surfaces. Bedrock scour and washing produces rock surfaces with boulder lag and scoured ponds. Depositional processes are responsible for the construction of several glacial landforms, in particular kames, eskers and kettle holes.

Kames are ice contact glaciofluvial landforms which occur as isolated hummocks or broad plateau areas. They consist of well sorted stratified sand and gravel and vary from 100 to 1000 meters in length and tens of meters in width. Eskers are sinuous ridges of glaciofluvial deposits formed by the deposition of sub-, supra- and englacial stream material. They are distinctive on account of their orientation parallel to the ice flow direction. Kettle holes are steep sided water filled pits formed by the melting of detached blocks of ice. They may be tens of meters in diameter and although cone shaped when freshly formed, slumping over time causes infill and shape modification (Hambrey, 1994).

Large quantities and seasonal fluctuations in melt-water discharge cause the formation of extensively braided river systems. Unless the river is confined by valley walls these outwash rivers deposit vast quantities of glaciofluvial material which are known as outwash plains. Alluvial fans form where decreases in stream channel velocity cause abrupt sediment deposition. Where meltwater channels enter proglacial lakes or larger river systems, sediment deposition creates deltas. Major phases of glacier retreat result in reduction in meltwater volume and lowering of lake levels, this produces abandoned lake shorelines and river terrace systems which may be dated and used in the reconstruction of glacial chronology. This has been done for the Barnes Ice Cap by Barnett (1967).

The reconstruction of glacial chronology may also be achieved through the mapping of moraines. Moraines are arguably the most significant of all proglacial landforms as they are formed by the direct interaction of ice and sediments at the ice front, and are therefore indicative of former ice extent. End moraines form parallel to the ice front and perpendicular to the ice flow direction. They are created by a variety of processes depending on the nature of the transport of glacigenic sediments and the method of deposition (Sugden and John, 1976). Cold based ice masses are limited in the manner in which they build end moraines. Minimal subglacial meltwater precludes the processes of proglacial tectonic deformation (Hart, 1994), instead the process of shear planes and the deposition of debris from a supraglacial position are more likely (Goldthwait, 1951; Weertman, 1961). Unless there is in-situ stagnation to form ice cored moraines, there is 'dumping' of material down the ice front. Figure 2.3 shows the formation of a 'dump moraine' (Small, 1983).

When the ice retreats the resultant deposit is termed an 'end moraine'. These features are usually curvilinear in form and vary in dimensions from a few meters to tens or even hundreds of meters depending on the sediment supply and the length of time the ice remained at the one location. As they are indicative of previous ice margin positions, end moraine mapping allows the extrapolation of patterns of ice mass shrinkage. Where the moraines can be dated using lichenometry the calculation of retreat rates is facilitated.
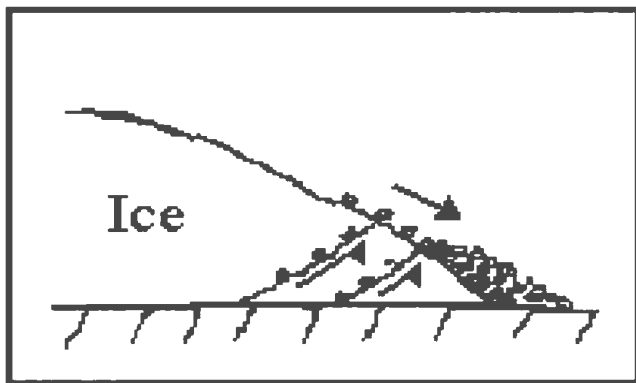
Figure 2.3 Dump moraine formation

In contrast to end moraines, ice cored moraines decay unevenly due to ice exposure, core melt and dissection by meltwater streams, to form linear hummocky moraine. Hummocky moraine is produced by the slow and uneven downwasting of debris covered stagnant ice beyond the currently active ice margin. It is characterized by chaotic uneven topography with undulations, mounds and water filled hollows or kettle holes. The dimensions of the components of hummocky moraine are usually in the order of meters and tens of meters (Sugden and John, 1976). The presence and absence of ice cored moraines may vary along the length of the ice margin according to the glacier thermal regime. Ice cored moraines develop where the glacier is frozen to the subsoil but are absent where persistent meltwater channels create local temperate basal conditions (Tatenhove, 1996). Consequently the observation of ice cored moraines, end moraines and hummocky moraine provide clues to the basal thermal regime of the glacier and meltwater flow patterns.

2.2 Applications of remote sensing to glaciology

Released from the logistical constraints of fieldwork in inaccessible and inhospitable environments, remote sensing offers an attractive alternative method of glaciological data collection. Remotely sensed data may be collected using airborne or spaceborne platforms and applications are constrained mainly by the resolution and the nature of the data. For small scale studies such as alpine valley glaciers, airborne imagery can be used to give ground resolution in meters. Airborne imagery is however, still restricted by weather and the expense of frequent flights. Spaceborne data acquisition offers the advantages of data collection at frequent time intervals irrespective of the weather and season. Satellite imagery is much coarser in resolution, typically tens to hundreds of meters and is suitable for large glaciers, ice caps and ice sheets.

The first satellites measured reflectance of solar radiation in the optical range of the electromagnetic spectrum (0.4 to 0.7 µm wavelength). In glacial environments these sensors distinguish between snow, slush, and bare ice using decreasing levels of spectral reflectance (Williams *et al.*, 1991), but saturation of the sensor at the short wavelengths due to high albedo, has restricted the effectiveness of this method. Sensors such as Landsat Thematic Mapper (TM), which record reflectance at the near infra-red and the thermal infra-red regions of the spectrum significantly increased the capabilities of snow and ice cover assessment. Hall *et al.* (1987) and Hall *et al.* (1989) developed a method of enhancing snow and ice features in TM imagery using a ratio of TM bands 4 and 5. The enhancement of these features aids the delimitation of the accumulation and ablation

zones and the extent of supraglacial debris cover. Linking the field studies of Benson (1962) to optical image interpretation of glaciers, Williams *et al.* (1991) summarized the applications of optical imagery with the glacier facies concept.

Mapping ice margin position in optical imagery is particularly complex due to difficulties in determining debris laden glacier termini from the surrounding outwash plain (Hall and Ormsby, 1983). Hall *et al,* (1989) used a ratio of TM bands 4 and 5 to enhance the contrast between ice and debris covered surfaces and separate them from the deglaciated terrain. The ratioing technique was applied to the Vatnajökull glacier in Iceland and the Pasterze glacier in Austria to map decadal patterns of margin retreat (Hall *et al.,* 1992). Hall *et al.* (1992) state that *"a line may be drawn on the image around the glacier terminus".* It is inferred from their diagram that this line separates the ice mass from the outwash plain and incorporates all the ice covered with supraglacial debris. Hall *et al.* recognise that the supraglacial debris cover is thicker over recessional areas than advancing areas but give no quantification of the breadth of debris cover and no estimate of the quantity of stagnant ice included in the ice mass.

The TM band ratio method has also been successfully applied to the Barnes Ice Cap by Jacobs *et al.* (1997). Here the limit of clean ice was taken to represent the margin. A 100 m buffer was applied to this limit in order that all the debris covered ice and ice cored moraines be included in the glacier ice extent calculations. It was believed that the

exclusion of these features would result in a considerable overestimation of the amount of retreat.

Passive optical imaging systems are constrained by the conditions of solar illumination. Manipulation of the timing and direction of the sensor may be used to enhance certain features through shadowing (Thomas, 1993). This offers possibilities for the enhancement of ice surface topography and ridge-shaped, proglacial features such as eskers and moraines. However, for high latitude regions this solar illumination requirement prohibits data acquisition for up to two and half months a year due to polar night. In addition to the image acquisition time restrictions there are weather restrictions imposed on optical imagery. Optical wavelengths cannot penetrate cloud and rain, so on cloudy days or in stormy weather the land surface cannot be imaged; this is arguably the biggest disadvantage of optical sensors.

Microwave wavelengths, because they are longer than the optical wavelengths, have the advantage that, except for very severe rainstorms, they are able to penetrate cloud and atmospheric moisture. Microwave sensors can therefore image in most weather conditions. Microwave sensing may be passive or active. Passive remote sensing measures the amount of radiation emitted by the earth's surface which is related to the surface temperature. These surface temperature data have proved useful for the monitoring of accumulation zones but the extremely coarse, kilometre scale spatial

resolution severely constrains the range of applications (Rott, 1984; Rees and Squire, 1989).

Active microwave sensing provides its own energy source by means of an electrical pulse with a wavelength in the order of centimeters to meters. This independent energy source means that it is possible to image during conditions of no solar illumination. SAR technology facilitates a finer spatial resolution than for optical sensors. The finest spatial resolution currently available by spaceborne SAR is the fine mode of RADARSAT (8 m). Interpretation of the first radar imagery of glacial environments, for example, Bindschadler *et al.* (1987), Bindschadler and Vornberger (1992) and Hall *et al.* (1995), was undertaken using combinations of both optical and radar imagery. Hall and Ormsby (1983) advocated that additional information was provided by SAR for debris covered termini and interlobate areas, but generally it was considered that SAR imagery contained no more information than was already contained in visual and infra-red imagery, (Rott and Mätzler, 1987; Rees and Squire, 1989). However, it is now becoming apparent that the information provided by SAR sensors has much to offer glaciological investigation as an independent data source.

In addition to guaranteed imaging SAR has four other advantages. Firstly, SAR is sensitive to surface moisture conditions which makes it particularly suitable for snow and ice applications (Vornberger and Bindschadler, 1992; Shi and Dozier, 1993). Secondly, SAR has a penetration capability that enables subsurface features such as medial

moraines (Bindschadler *et al.*, 1987), buried crevasses and relic drainage channels to be detected in cold arid environments. Aridity is common in high latitude glacial environments as the extremely low air temperatures prohibit the presence of moisture. The amount of penetration varies according to the radar wavelength, the surface materials and topography, consequently the sensor must be selected to enhance the subsurface features of interest. Thirdly, phase differences between radar images of the same area separated by short time intervals, may be used in the detection of surface displacement using interferometry. This is particularly valuable for monitoring ice velocity (Rignot *et al.*, 1996; Rignot *et al.*, 1997; Mohr, 1997; Gray *et al.*, 1998), and with more than one interferometric pair it is possible to extract surface elevation and produce a digital elevation model (DEM) (Mohr, 1997). Fourthly, SAR images of the same area with different look directions have stereoscopic properties and may be viewed for a perception of relative elevation and used in the creation of DEMs (Sabins, 1987).

2.3 Radar image interpretation

Radar image brightness is the recorded radar backscatter from an imaged surface. The strength of the radar backscatter is controlled by the relief, moisture content, dielectric constant and the surface roughness of the imaged surface.

2.3.1 Relief

Relief interacts with the surface properties in controlling the radar return. Slopes that face the sensor (foreslopes) reflect the pulse directly back, therefore producing a higher backscatter response. Conversely, slopes that face away from the sensor

(backslopes) direct the pulse away and therefore produce lower radar returns. In areas of very rugged terrain the effects of relief produce three phenomena which complicate radar image interpretation. They are layover, foreshortening and shadowing. Where the foreslopes are very steep the radar pulse is returned from the top of the slope before the bottom. This results in unusually bright pixel values at the location of the slope referred to as 'layover'. Foreshortening is where steep foreslopes are misrepresented as proportionally shorter than reality, due to the radar pulse reaching the top of the slope in almost the same amount of time it takes to reach the foot of the slope. Shadowing occurs where the backslope is steeper than the radar incidence angle, for these areas no radar backscatter is recorded. Consequently, in areas of high relief a proportion of the image may lack data. Image shadow is an important factor for visual interpretation of imagery and aids the identification of linear features.

2.3.2 Moisture content and dielectric constant

Moisture content and dielectric constant are directly related. The dielectric constant or conductivity of a material affects the radar return through 'dielectric losses'. A material with high conductivity absorbs some of the microwave energy through high dielectric losses and so lowers the intensity of the backscatter. The presence of water increases the conductivity of a medium and so increases the dielectric losses, thus lowering the backscatter from a wet surface. Materials with high moisture content and high dielectric constants therefore produce lower radar returns than their dry counterparts.

Due to moisture sensitivity, SAR has strong potential for mapping patterns of snow melt. Therefore, most microwave glaciological applications to date have focused on snowline mapping and delimiting the areal extent of the accumulation zone and the characteristics of the snow and ice cover (Rott, 1984; Rott and Mätzler, 1987; Donald *et al.*, 1993; Fahnestock *et al.*, 1993; Jezek *et al.*, 1993; Rott and Nagler, 1993; Shi and Dozier, 1993; Maxfield, 1994; Shi *et al.*, 1994; Rees *et al.*, 1995; Brugman *et al.*, 1996; Smith *et al.*, 1997). Forster *et al.* (1993) have proposed the concept of 'radar glacier zones'. In summary, dry snow of high latitude ice sheet accumulation zones of Greenland and Antarctica produces a bright uniform response. The percolation facies, where meltwater percolates into the snow layer and refreezes to form networks of ice lenses and ice pipes, also produces high backscatter. The percolation zone differs from the accumulation zone in that it usually contains image texture due to topographically controlled drainage patterns (Jezek *et al.*, 1993). The wet snow and slush facies produce very low radar backscatter during the melt season due to the presence of melt water and high dielectric losses. During the accumulation season however, these facies are both frozen and produce similar high backscatter responses. Radar backscatter from bare ice is complex. Ice surface roughness relative to radar wavelength determines the backscatter and so results differ significantly between study areas and sensors.

In the proglacial environment surface moisture varies with drainage capabilities and vegetation cover. Large grain sizes and elevated surfaces drain more easily and are

characteristically drier than fine sediment surfaces and topographic depressions. Subsequently, surfaces composed of large grain sizes such as boulders, produce higher radar backscatter than fine sediment surfaces. The presence of vegetation will affect the radar response of a surface due to retention of moisture in the plant leaves and stem, and increased moisture retention in the soil due to root structure (Loor, 1968). Vegetation is particularly sparse in the proglacial environment due to the inhospitable climate and the instability of the sediments. Lichen cover is abundant but unable to retain moisture and probably ineffectual for altering radar response. Vegetation is found only in the stable areas of the proglacial zone in the form of low growing herbs, woody plants, grasses and sedges. These plants alter the moisture retaining capacity of the surface materials and may affect the radar response. However, for active microwave sensors operating at lower frequencies and with higher incidence angles, such as is characterized by the RADARSAT SAR, soil moisture and dielectric constant are considered to be of lesser importance than surface roughness (Altese *et al.*, 1996).

2.3.3 Surface roughness and structure

Surface roughness is determined by the arrangement of small scale surface features similar in size to the radar wavelength, such as pebbles or gravel particles. Surface roughness is a combination of both the vertical and horizontal dimensions of the surface variation, although vertical relief is found to be an adequate estimation of surface roughness (Sabins, 1987). Surfaces are rough or smooth depending on the surface height variation relative to the radar wavelength and the local incidence angle.

The threshold between radar smooth or rough surfaces has been defined by the Rayleigh criterion (Sabins, 1987).

$$\text{Rough (diffuse)} = h > (\lambda/\, 8)/\cos\theta \qquad\qquad (2.1)$$

$$\text{and} \quad h = \sqrt{\frac{\Sigma \left(Y_i - \bar{Y} \right)^2}{n-2}} \qquad\qquad (2.2)$$

where:

λ : radar wavelength (cm)

θ : local incidence angle (°)

h : root mean square of surface height variation

n : number of observations

Y_i : observation i

$\bar{Y}$: mean Y

A set of two equations have modified the Rayleigh criterion to incorporate an intermediate category between rough and smooth surfaces (Peake and Oliver, 1971) as follows:

$$\text{Rough (diffuse)} = h > (\lambda/4.4)/\cos\theta \qquad\qquad (2.3)$$

$$\text{Smooth (specular)} = h < (\lambda/25)/\cos\theta \qquad\qquad (2.4)$$

Smooth surfaces behave as specular reflectors and scatter little of the transmitted radar pulse back to the sensor, therefore producing low returns and dark areas in an image, see Figure 2.4a. Examples of smooth surfaces would be standing water bodies, and fine glaciofluvial sediments. Rott (1984) found that there was confusion between relatively smooth proglacial alluvial deposits and the similarly low backscatter values

produced by the firn and the wet snow facies upon the glacier. Rough surfaces produce diffuse reflectance which backscatters some of the pulse to the sensor and so the area appears bright on the image, see Figure 2.4b. Examples of rough glacial surfaces would include crevassed areas, areas with numerous incised supraglacial streams, or uneven boulder covered surfaces.

Surface structures such as corner reflectors exert influence over the nature of the radar backscatter. Corner reflectors are formed when two smooth surfaces are arranged at right angles, this structure reflects the radar pulse directly back to the sensor producing high returns and very bright spots in the imagery, see Figure 2.4c. Objects which might simulate corner reflectance in the remote tundra and glacial landscape are a rock within a pond or an ice cliff bordering a water body or a smooth bedrock surface.

(a) Diffuse reflectance   (b) Specular reflectance   (c) Corner reflectance

(Modified from Lillesand and Kiefer, 1994)
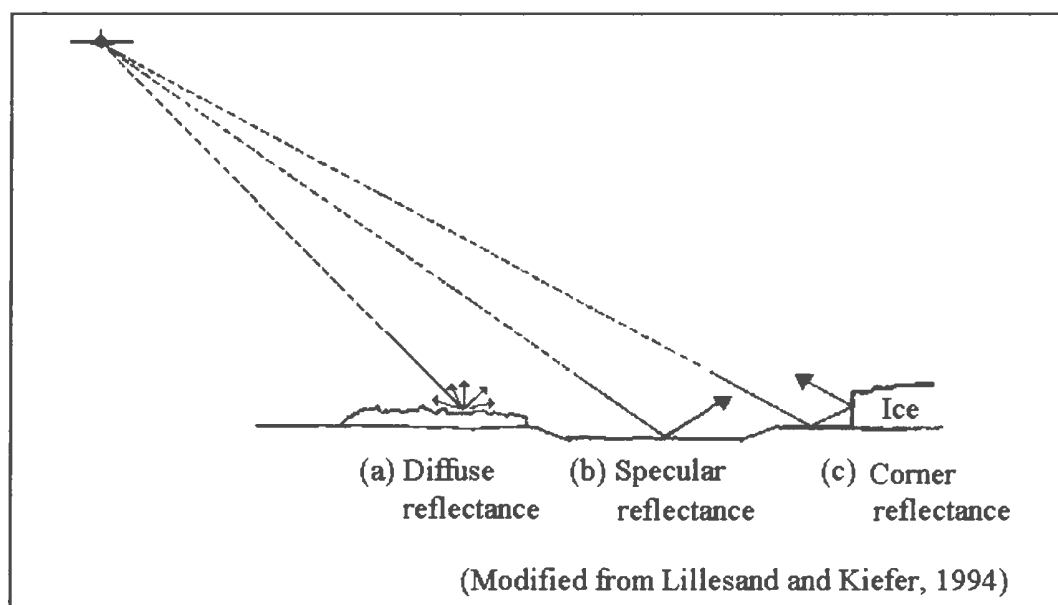
Figure 2.4 Specular and diffuse reflection of active microwave radiation from rough and smooth surfaces and a corner reflector

Measurements of the surface roughness are important for modeling radar backscatter and have been accomplished through the use of close up stereophotography (Weeks *et al.*, 1996), fine scale laser altimetry (Schaber *et al.*, 1976) and a tool termed a 'terrain templet' (Gaddis *et al.*, 1990; Benallegue *et al.*, 1995). The terrain templet consists of a linear array of closely spaced vertically movable rods. The vertical displacement of the rods to reflect the ground surface, quantifies the height variation at the surface. The profile data are used to calculate statistical parameters of surface roughness.

The grain size of the surficial sediments is a natural control on the range of vertical height variation and therefore plays an important role in surface roughness. Grain size analysis is thus a logical method of indirectly quantifying the surface height variation. Grain size composition, particularly the relative proportions of clay and sand particles, influence the ability of a soil to retain moisture, therefore exerting further control on the radar response. Consequently, soil texture has been quantitatively analysed for agricultural applications of radar (Dobson and Ulaby, 1981). At larger scales, grain size is important for geological and structural applications of radar imagery. Lithology influences surficial characteristics of rock surfaces and the size of particles produced by weathering, hence grain size is a key factor in the interpretation of radar imagery for geological mapping (Hanks and Guritz, 1997). Nevertheless, investigations of lithological grain size related to radar backscatter remain qualitative in nature and of secondary importance to measurements of vertical height variation. A detailed description of surface height variation and grain size composition for surface materials of

Death Valley, California, related to Seasat SAR data (L-band SAR with wavelength 23.5 cm), concluded that *"radar signatures alone cannot be used to identify the composition of materials"* (Sabins, 1987).

2.3.4 Radar penetration

Where the surface is smooth and dry there is no absorption of the radar pulse by dielectric losses and no immediate backscatter due to surface roughness. In this case the radar pulse will penetrate the surface materials and the subsurface properties will control the backscatter. Penetration depths vary with pulse wavelength and moisture content of the surface and subsurface materials. For smooth surfaces, example penetration depths for the C-band are, ~5 cm for wet snow (Rott, 1984), 20 cm for dry snow, and up to 9 m for bare ice (Rignot *et al.*, 1996).

2.4 Ice margin mapping applications of SAR

Much work using radar has focused on ice masses terminating in water bodies. The intense crevassing associated with ice cliffs and iceberg calving produces very rough surfaces and consequently a very high radar return. There is a marked contrast between this and the low return of still water surfaces which reflect specularly. The clear distinction between rough ice and smooth water permits accurate identification of ice margin positions. Glaciomarine margin mapping applications using ERS-1 SAR data (C-band with like vertical polarization, nominal spatial resolution of 30 m and a 23° look angle) have been successful in Greenland (Fahnestock and Bindschadler, 1993) and

Antarctica (Skvarca *et al.*, 1995). Hall *et al.* (1995) advocate late ablation season imaging of terrestrial ice margins in order to capitalise on the contrast between the open water of ice marginal lakes and the glacier surface.

Terrestrial glaciers were the focus of a study by Shi and Dozier (1993) which concluded that in areas of very high relief the complications of layover, foreshortening and shadow rendered SAR no more effective for glacier monitoring than optical sensors. Shi *et al.* (1994) insisted that SAR was useful for the delimitation of snow cover but, as it could not distinguish between rock and glacier ice, optical imagery was preferable for ice margin mapping. In contrast, Adam *et al.* (1997) used ERS-1 SAR imagery to automatically map the divide between rock and ice surfaces at the margin of the Place Glacier Basin, British Columbia, a region of rugged terrain. Adam *et al.* obtained a locational accuracy of 75 m for the margin and which is in accordance with the accuracy required for hydrological purposes and mass balance calculations (Adam *et al.*, 1997).

In an area of low relief, Rott (1984) found that the debris covered termini were clearly distinguishable from surrounding terrain in SAR imagery, on account of the elevated, rough surface of the terminus producing a much higher backscatter value than the lowlying surrounding terrain. This makes SAR particularly useful for ice margin mapping.

Sohn and Jezek (1996) developed an automated method of ice margin extraction for a length of the Greenland Ice Sheet margin using ERS-1 SAR imagery. The method identified the limit of clean ice to within 300 m of the limit as seen on the visually interpreted image. When SPOT HRV and air photo data were included in the method the accuracy improved to 150 m (Sohn, 1996).

Two points are immediately apparent from the examination of previous studies. Firstly, conclusions on the usefulness of SAR in the study of the ice marginal environment are conflicting. Despite the initial negative conclusions of Shi and Dozier (1993) and Shi *et al.* (1994), SAR imagery has been used successfully in other ice margin mapping studies and demonstrates potential for further exploitation. Secondly, in both optical and microwave imagery there is a lack of consistency in the definition of the term 'ice margin'. Typically the term 'rock and ice divide' is used, which suggests that the authors do not acknowledge the presence or absence of supraglacial debris. Alternatively the extent of clean ice is specified, but apart from Jacobs *et al.* (1997), no estimation of the breadth of the marginal debris cover is provided. With no consideration of the nature of the margin and its dynamics it is impossible to judge whether the extracted margin truely represents the limit of active ice or how accurately the margin is placed considering the spatial resolution of the data.

2.5 Speckle and image filtering

Radar image data contains high frequency noise referred to as 'speckle'. Speckle causes random variation in grey levels that result in a grainy or salt and pepper appearance of the radar image (Rees, 1990). Image speckle must be removed, or at least reduced to make image values consistant for a surface cover type (Frost et al., 1982). It has been established that speckle filtering is essential to improve the accuracy of pixel by pixel image classification (Durand et al., 1987; Pultz and Brown, 1987). Various filter procedures have been developed for the reduction of image speckle, some operating in the frequency domain and others in the spatial domain. Durand et al. (1987) rejected frequency domain noise filtering because they found that it introduced low frequency interference, or artificial texture, on the SAR image as well as smoothing edges and removing legitimate textural areas. Spatial domain filtering is therefore examined here as a method of image speckle removal.

2.5.1 Spatial domain filtering

Spatial domain filters operate directly upon the image values. Original averaging box filters, which simply smooth image values, have now been superseded by adaptive filters. Adaptive filters modify the filtering process according to local image statistics, in order that information contained within the image values is preserved (Shi and Fung, 1994). These adaptive filters reduce smoothing over edges, preserve areas of heterogeneity and isolated scatterers, while smoothing areas of homogeneity (Lee, 1980; Frost et al., 1982; Kuan et al., 1987; Lopes et al., 1990; Lopes et al., 1993). In this

manner image texture is detected and preserved. A comparison of 10 different speckle filtering methods by Durand *et al.* (1987) concluded that the adaptive filters were superior because they distinguished between useful information and speckle during the filtering process. Mastin (1985) concluded that adaptive smoothing filters were the best compromise between the competing goals of variance reduction and edge preservation.

2.5.2 Multilook image processing

Speckle may also be reduced by multilook image processing. This process reduces image speckle by combining images of the same scene and averaging the backscatter values (Rees, 1990). Thus each pixel value for the resultant image is an average value and has already experienced some smoothing. The RADARSAT fine mode image is a single look image, but the standard mode images are four look images. The disadvantage of this averaging method is the degradation in spatial resolution. The four look images have 25 m spatial resolution compared to 8 m spatial resolution of the single look.

2.6 Image texture

Image texture is the spatial variability of the tonal values within an image. The large scale, uneven nature of a surface causes variation in pixel backscatter values that is expressed as image texture. Heterogeneous surfaces have a large range of backscatter values over a small area. This high variability is expressed as coarse texture. Homogeneous surfaces have low variability and hence, fine image texture. Image texture assists the visual interpretation of radar imagery and when modeled mathematically, it

may be used as an input to radar image classification (Ulaby *et al.*, 1986). Image textural information has been shown to increase image classification accuracy (Ulaby *et al.*, 1986; Gong and Howarth, 1990; Shi and Dozier, 1993; Kushwaha *et al.*, 1994; Nezry *et al.*, 1996; Rotunno *et al.*, 1996)

There are a large number of quantitative approaches to texture analysis. Of the most common are the analysis of the Fourier power spectrum resulting from the discrete Fourier transform (Stromberg and Farr, 1986; Ehrhard *et al.*, 1993), first order statistics of grey levels (Hsu, 1978), second order texture statistics (Haralick *et al.*, 1973; Haralick, 1979), grey run length statistics (Galloway, 1975), texture units and spectra (Wang and He, 1990) and most recently, developments in fractal modeling of image texture (Dodd, 1987; Stewart *et al.*, 1993; Liu and Chang, 1997). The fractal methods produce good results (Liu and Chang, 1997) but are new and relatively inaccessible. Comparative investigations of the other texture analysis techniques have found that first and second order texture measures have been consistently most successful (Barber *et al.*, 1993; Weska *et al.*, 1976, Hsu, 1978; Conners and Harlow, 1980; Ulaby *et al.*, 1986; Alparone *et al.*, 1990).

First and second order measures use texture algorithms to quantify the relationship that a pixel has to its neighbouring pixels within a texture window. The window is an uneven number of pixels square so that the centre pixel may be assigned the value computed by the texture measure algorithm. The size of the texture window is

an important consideration when extracting image texture (Woodcock and Strahler, 1987; Dillworth, 1991; Dillworth et al., 1994) and the window must be smaller than the expected area of the features to be identified (Baraldi and Parmiggiani, 1995; Rotunno et al., 1996) in order that a pure texture statistic be extracted.

2.6.1 First order texture measures

First order texture measures quantify the amount of tonal variation within a texture window in terms of mean, standard deviation and variance. A low variance characterizes a homogeneous area while a high variance implies a heterogeneous area. First order texture measures have been used in glacial environment classification (Shi and Dozier, 1993; Shi et al., 1994; Sohn and Jezek, 1996). Shi and Dozier (1993) improved the classification accuracy of rock and ice surfaces from 66% to 74% through the inclusion of a variance texture measure. Sohn and Jezek (1996) used the coefficient of variance as a discriminator for measuring the coarseness of ice sheet and deglaciated rock area texture.

2.6.2 Second order texture measures

Second order texture measures use statistics calculated from grey level cooccurrence matrices (GLCMs). By quantifying the distribution patterns of the elements within the matrix they are able to provide information about the nature of the tonal variation, rather than just the amount of variation as calculated by the first order texture measures. They have been used with success in sea ice discrimination (Holmes et al., 1984; Barber and LeDrew, 1991; Shokr, 1991; Barber et al., 1993), terrain discrimination

(Weska *et al.*, 1976; Franklin and Peddle, 1987) and glacial environment image classification (Baraldi and Parmiggiani, 1995; Adam *et al.*, 1997). The GLCM approach assumes that the texture information in an image is contained in the overall spatial relationship between grey values of an image (Shanmugan *et al.*, 1981) and this information is captured in the GLCM. The GLCM is a square matrix with n^2 elements where n is the number of possible image values or digital numbers (DN) a pixel may assume. A matrix element (i, j) denotes the frequency with which a DN i occurs adjacent to a DN of j. Adjacent is defined as a specified pixel distance from one pixel to another in a particular direction. This directional factor is known as the spatial function and is expressed as displacement or $\delta = (\Delta x, \Delta y)$, for example $\delta = (1, 0)$ would be the adjacent pixel to the right. Figure 2.5 shows the pixel values for a small image segment of 5 x 5 pixels with gray tone values 0-3 and the resultant GLCM.

0	1	1	2	3
0	0	2	3	3
0	1	2	2	3
1	2	3	2	2
2	2	3	3	2

Original Image values

	0	1	2	3
0	1	2	1	0
1	0	1	3	0
2	0	0	3	5
3	0	0	2	2

Resulting GLCM matrix for image values with displacement 1, 0
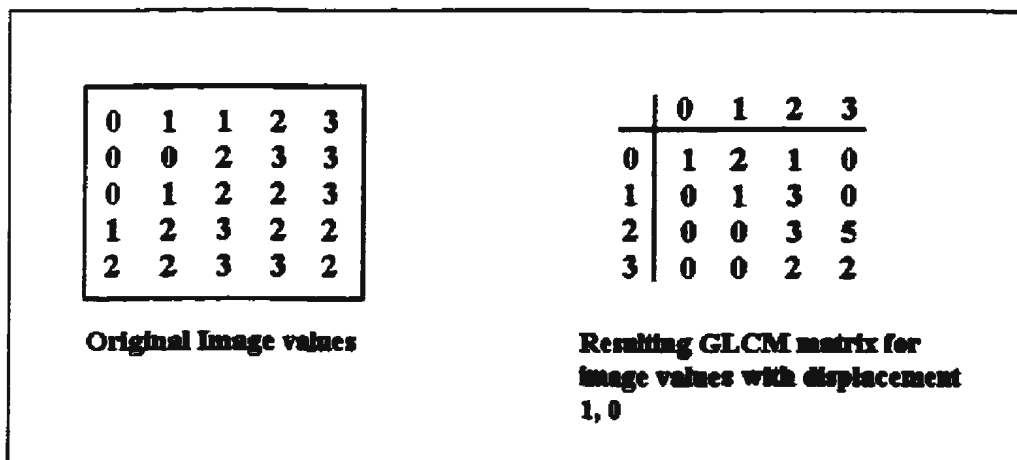
Figure 2.5 GLCM example

Features in radar imagery are dependent on the look direction, consequently the choice of spatial function produces preferential detection of features with a particular orientation. To eliminate the angular dependency of the final texture image it is advantageous to calculate texture values for four opposing directions and average the results (Sun and Wee, 1982).

The diagonal elements of the GLCM matrix represent the numbers of directly adjacent identical pixels. The amount of dispersion that the matrix elements have about the diagonal may be measured statistically through different texture algorithms. Fourteen texture algorithms were originally proposed by Haralick *et al.* (1973), yet there exists no general consensus on which measures are the best, as results vary considerably with the application. However, six measures occur most frequently in the literature and have been used successfully in a variety of geomorphological applications such as terrain class discrimination (Weska *et al.*, 1976; Franklin and Peddle, 1987), glacial environment classification (Baraldi and Parmiggiani, 1995) and the mapping of lava flows (Gaddis *et al.*, 1990). These six measures are contrast, angular second moment, correlation, homogeneity, entropy and standard deviation.

2.7 Image classification

Image classification is the delimitation of the areal extent of categories of interest in remotely sensed imagery in order to produce thematic maps. Automated image classification methods may be divided into hard or fuzzy logic (Jensen, 1996). Hard

classification logic is where each pixel is assigned to one class only. Fuzzy logic recognises the existence of mixed pixels and each pixel is assigned to every class with varying probabilities of membership. The fuzzy method is valuable for examining the makeup of mixed pixels (Fisher and Pathirana, 1990; Foody and Trodd, 1993) but hard classification logic is necessary for the production of thematic maps.

Automated methods of image classification are based on computed statistics and may be divided into unsupervised and supervised approaches. The unsupervised approach uses computer algorithms to identify spectral clusters in the data, the most common methods are the K-means and the isodata approach (Jensen, 1996). The spectral clusters are then identified and labeled by the analyst as information classes using ancillary data sources. The supervised approach extracts sample spectral signatures from pixels of known land cover type referred to as training areas. These example signatures train the classifier in the recognition of areas of similar response in the image, and a classification algorithm is used to classify the entire image and produce a thematic map. For the supervised approach the three most common classification algorithms are the parallelpiped, minimum distance to means and the maximum likelihood. These per-pixel classifiers consider individual pixel values and use statistical rules to assign pixels to a land cover class. Supervised classification may be considered as the more direct method as the classes of interest are specified from the outset.

The parallelpiped method uses the range of values of a training area to assign

image pixels to a class. Pixels which fall within the range of the training pixels are classified, those which fall outside are left unclassified. This method is computationally simple but cannot distinguish between overlapping class ranges and takes no account of the distribution of pixel values. The minimum distance to means classification algorithm assigns a pixel to the class with the closest mean value. The overlap problem of the parallelpiped is therefore avoided, but again no account of the variability or pattern of dispersion of values is made.

The maximum likelihood method is the most robust of the classification algorithms. It takes account of the variability and distribution of category values by modeling a probability density surface using equiprobability contours for each class. The structure of the classification feature space and the equiprobability contours is illustrated in Figure 2.6. Each pixel is assigned to the class for which it has the highest probability of membership. In the construction of the equiprobability contours the method assumes a Gaussian distribution for all training area input data. Care must therefore be taken to ensure that the Gaussian approximations are valid (Schott, 1997).

Where there is great overlap of class equiprobability contours, the inclusion of *a priori* probabilities has been shown to significantly improve classification accuracies (Mather, 1985). *A priori* probabilities or weights are used in the calculations of pixel class membership probabilities. The weights should represent the relative proportion of each image class determined from independent knowledge of the area (Strahler, 1980).

B=Boulderfield

D=Dump Moraine

I=Ice

A=Alluvial Sediments

W=Water

Image Tone

Equiprobability Contours

Image Texture (Correlation)
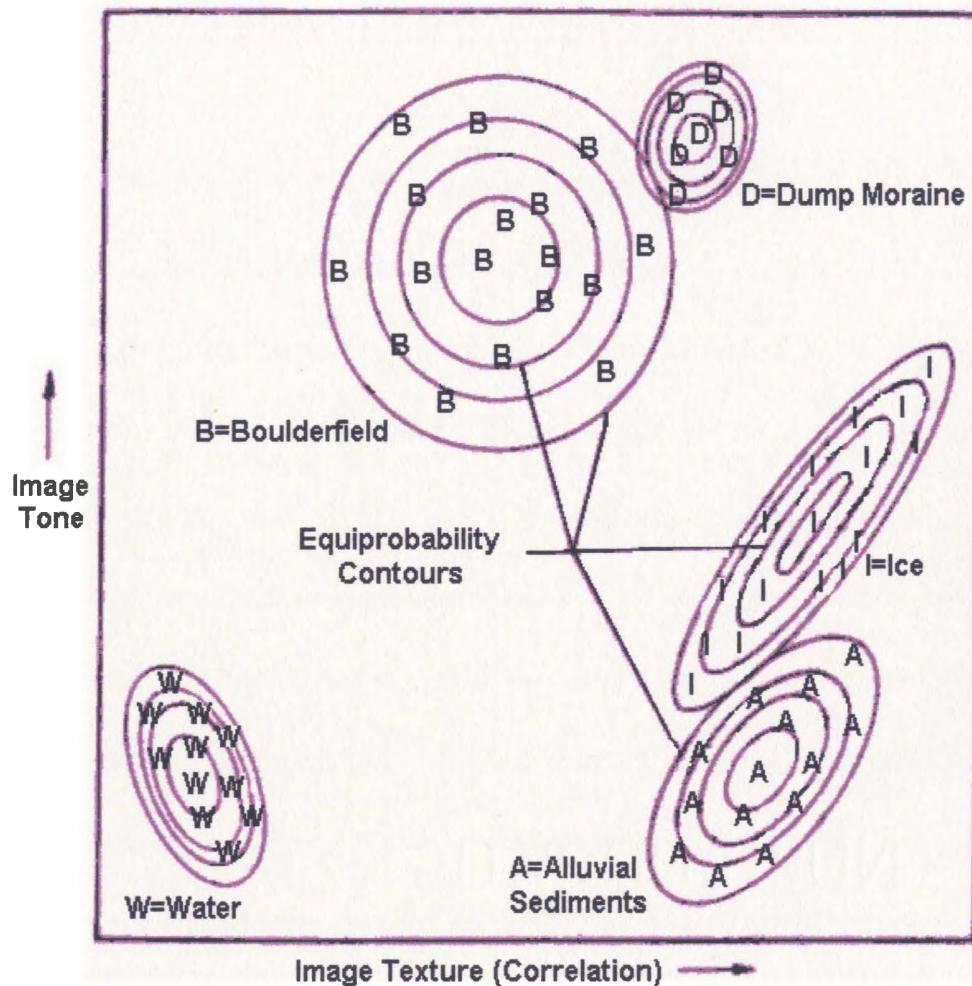
(Source:Modified from Lillesand and Kiefer, 1994)

Figure 2.6 An example of a maximum likelihood feature space and equiprobability contours defined for an ice marginal environment

When the Gaussian data distribution conditions for the maximum likelihood method are not satisfied alternative methods of image classification such as neural networks and discriminant function analysis may be used. Neural networks work by an iterative process which trains the classifier to balance class weightings until the classifier can correctly identify the training areas, or at least to a desirable degree of accuracy. The

developed method is then applied to the entire image.

Neural networks are an example of artificial intelligence and represent the leading edge in classification methodology. Tentative results suggest improved classification accuracies using neural networks over conventional classification algorithms (Hepner *et al.*, 1990; Foody *et al.*, 1994), but the still developing software and high demands on computational time and memory, currently restrict their widespread application. Discriminant function analysis is similar to layered classification or decision tree classification. In this method decision rules are used to assign pixels to classes in a series of stages (Schowengerdt, 1983; Jensen, 1996; Lillesand and Kiefer, 1994). These classifiers are computationally simple and are most effective when pixel values are clearly separated into groups, for example when including ancillary nominal data into the classification method. Remote sensing data are continuous, and significant overlap of class values implies that statistical methods are more appropriate.

The maximum likelihood algorithm has emerged as the one of the most commonly used algorithms (Kushwaha *et al.*, 1994) and has been used in several ice margin classification case studies to date, for example, Shi and Dozier (1993), Shi *et al.* (1994), Adam *et al.* (1997). Other ice margin classification studies have used thresholding algorithms similar to discriminant functions, for example Jacobs *et al.* (1997), Sohn and Jezek (1996) and Sohn (1996). These decision methods have been successful where the number of image classes is very small. There is some skepticism

expressed over the suitability of the maximum likelihood method for radar data, particularly that the presence of speckle in radar imagery makes the Gaussian assumption of training data invalid (Frost and Yurovsky, 1985; Wong and Posner, 1993). Speckle filtering reduces the relevance of this argument. Classification of SAR imagery has been performed using a variety of algorithms and methods, all with apparent success for their chosen application. No one classification method emerges to be consistently more successful than any another. Simple statistical methods such as minimum distance to means have been successful (Carr, 1996; Alparone et al., 1990), thresholding algorithms or decision methods are frequently used, new clustering algorithms (Wong and Posner, 1993) and neural networks are being developed, and despite the Guassian data distribution point of discussion, the maximum likelihood method continues to be widely utilized.

2.8 Edge detection

Edge detection or edge enhancement is particularly useful for detecting linear features and image components which cannot be considered as independent image classes. An ice margin is a perfect example as it represents the divide between a glaciated and nonglaciated surface. Edge detection identifies abrupt changes in image values such as are characterised by class boundaries. The method involves running a special edge detection filter kernel through the entire image (Gonzalez and Woods, 1992). The pixel values of the resultant edge image are the product of the filter kernel weightings and the original image values, they are referred to as 'edge amplitudes'. The size and weighting

distribution of the filter kernel determines the type of edges that are detected. Weightings may be balanced in all directions so that all abrupt changes in image values are identified, such as the Laplacian filter shown in Figure 2.7(a), or in direct opposition to detect linear features of a particular orientation, such as the Sobel 2.7(b) and Prewitt 2.7(c) kernels. Edge images with specific orientation may be combined later to produce omnidirectional edge images.

The resultant edge image values are indicative of the edge amplitude at that point. Different features or types of edge are represented by different edge amplitudes. Where the image class values are known, the possible edge values produced by filter kernel weightings may be calculated, and so the different types of boundaries may be identified and classified.

0	1	0
1	-4	1
0	1	0

1	2	1
0	0	0
-1	-2	-1

-1	0	1
-1	0	1
-1	0	1

(a) Laplacian Filter
Kernel

(b) Sobel Filter
Kernel

(c) Prewitt Filter
Kernel
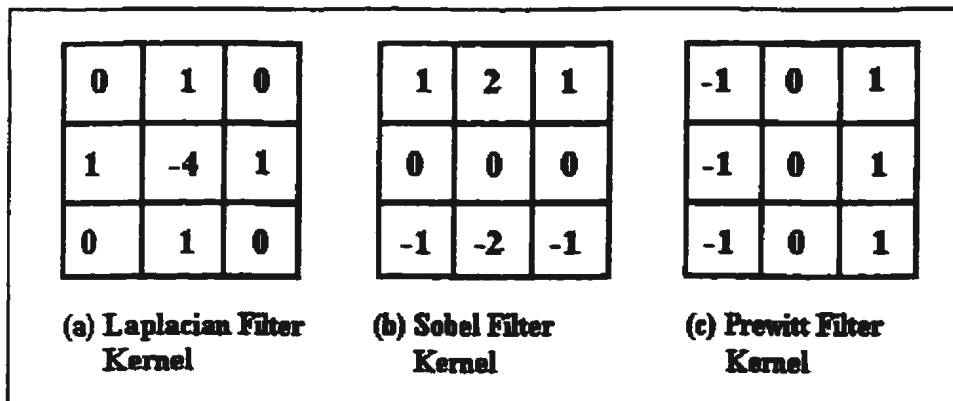
Figure 2.7 Example edge filter kernels

Edge amplitude is calculated from the image values within the edge filter kernel. If different boundary features have similar backscatter values or similar degrees of

contrast, the resulting edge amplitudes will be similar and boundary type will be indistinct. If the image is first classified and image classes assigned specific values, then the calculated edge amplitudes will be clearly representative of the boundary type, and so it becomes possible to distinguish the edges of interest from all the edges of the image.

Sohn (1996) and Sohn and Jezek (1996) used the Roberts method of edge detection in their automated technique of ice margin extraction. Using a SAR image classified into three classes, a Roberts filter was applied to detect all the boundaries of the rock surfaces. A recursive line following algorithm then extracted all the rock boundaries as line vectors. A threshold length criterion was used to determine which vectors represented the rock and ice boundary and which short vectors were spurious lake edges or artifacts and therefore removed.

In summary, the method of edge detection is vital for the detection of boundary features for which classification is inappropriate. A combination of image classification and edge detection, as developed by Sohn (1996) and Sohn and Jezek (1996), is necessary to identify only the edges of interest. This method provides the most promising results for the automatic extraction of ice margins from radar imagery.

3. Problems and research objectives

The literature review highlights the glaciological and geomorphological difficulties encountered in mapping a glacial environment and reveals the limitations of remote sensing studies of land based ice margins to date. This chapter isolates the two major problems of remote ice margin mapping and outlines a strategy of study to find solutions.

3.1 Problems

Terrestrial ice margins present particular problems for the measurement of terminus position. Delimiting the exact extent of an ice mass is complicated on account of dirty ice, supraglacial debris and the presence of both ice cored and end moraines. The similar geological properties of bedrock outcrops, supraglacial debris, moraine and outwash plain material produce similar spectral responses, and so ice marginal features are difficult to distinguish using optical remote sensing techniques (Hall *et al.,* 1989). These features must be identified in order to accurately map the extent of the active ice.

Radar data are controlled by relief, surface roughness and surface moisture content rather than spectral properties therefore, this alternative source of data may prove to be suitable for ice margin mapping. Methods of automated image classification and ice margin extraction for radar imagery are being developed, but they currently lack consistency in the definition of the ice margin.

3.2 Research objectives

The global objective of this research is to assess the potential of radar imagery for the classification of an ice marginal environment, and for the delineation of the limit of active ice. The classification method is to be based on image parameters which can be extracted by computation, thereby allowing automated classification and ice margin extraction from subsequent radar imagery of the same location. The classification method is to be based on the characteristics of ice marginal landforms in terms of image texture.

The secondary objectives examine the characteristics of different RADARSAT images with regard to look directions and spatial resolution:

1. To quantify the surface roughness variations characteristic of different landforms, understand how they are related to radar brightness values and conclude whether the differences between features are sufficient to be used in their identification in radar imagery.

2. To examine image texture in standard mode imagery and establish whether different image texture measures can be used to distinguish between ice marginal features.

3. To compare the classification accuracies obtained for 8 m fine and the 25 m standard spatial resolution and determine which is most successful for resolving ice marginal features.

4. To identify the optimal radar look direction for identifying the limit of active ice.

4. Study site and data

The Barnes Ice Cap provides a suitable site for the development of a classification method for radar imagery of an ice marginal environment. The area contains a variety of typical glacial landforms, has an associated body of literature and is accessible for the collection of ground truth data. This section describes the Barnes Ice Cap study area in detail, justifies the choice of study area and lists the data sources employed in this research.

4.1 Location and characteristics of the Barnes Ice Cap

The Barnes Ice Cap is located on the central plateau of Baffin Island, Nunavut, Canada, between 69.5° and 70.5° N. latitude. Figure 4.1 shows the ice cap with the coverage of the RADARSAT imagery and the location of the study area. The limited topographic variation of the interior lowlands of Baffin Island causes the ice cap to be almost elliptical in shape with no major protruding outlet glaciers. It is approximately 150 km long, has a maximum width of 62 km and covers an area of 5900 km^2. A slight constriction near the southern end separates the topographic high of the south dome from the main body, or north dome, of the ice cap (Løken and Andrews, 1966). The summits of the north and south domes are 1128 and 975 m a.s.l. respectively (Sagar, 1966).
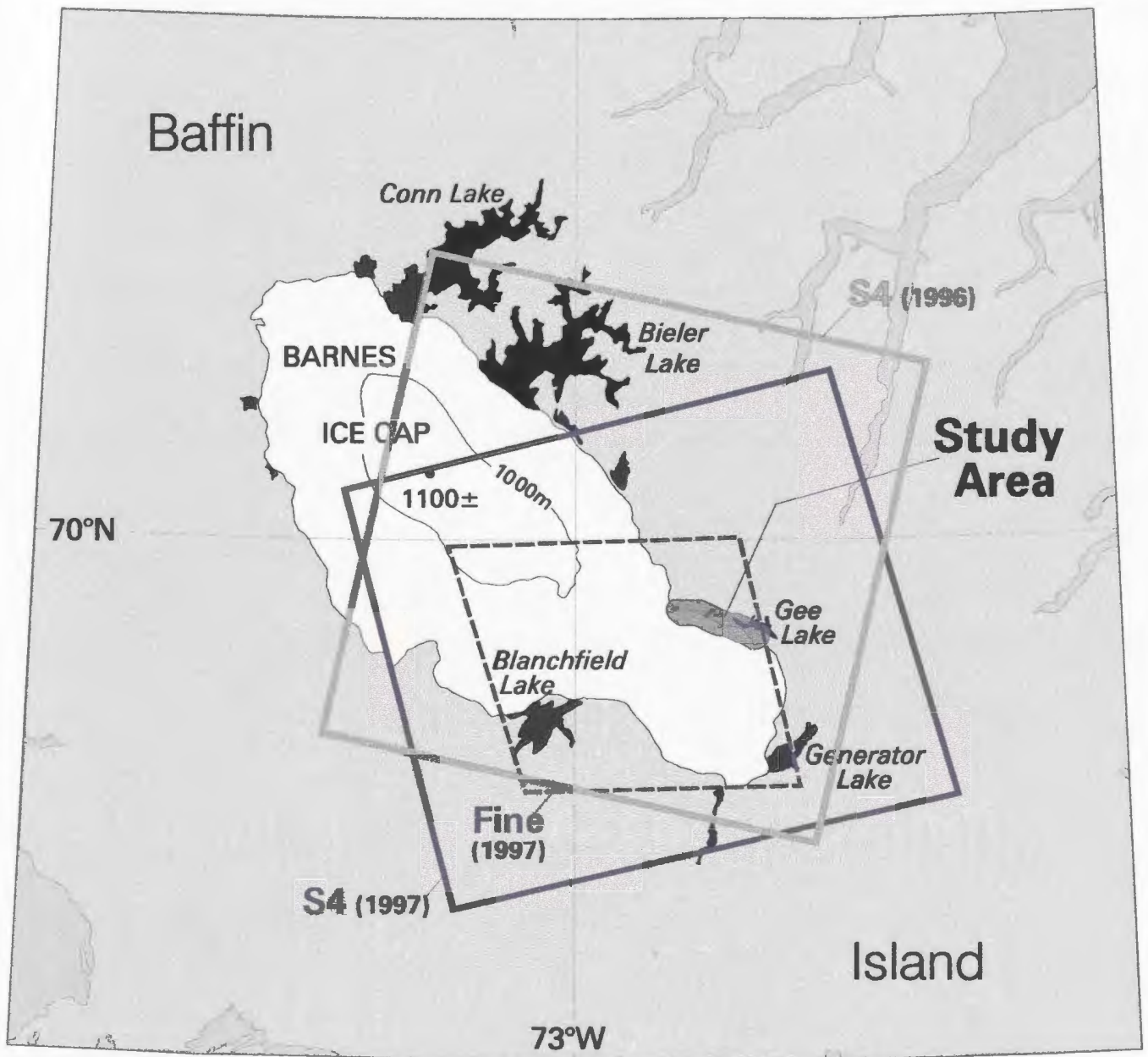
Figure 4.1 Location map of the Barnes Ice Cap study area with RADARSAT image coverage

4.2 Previous studies of the Barnes Ice Cap

Studies of the region by Ives and Andrews (1963) have determined that the ice cap is a remnant of the last ice age and that it attained its present configuration approximately 3000 years ago. Investigations of the ice surface have concluded that the ice cap is currently maintained by the formation of superimposed ice and firn accumulation, with the ice surface being characterised by puddles and slush and the absence of a dry snow accumulation zone (Baird et al., 1952; Sagar, 1966; Hooke et al., 1987). Most authors concur that the Barnes Ice Cap is a cold based ice mass (Goldthwait, 1951; Baird et al., 1952; Hooke, 1973; Holdsworth, 1973 and Hooke et al., 1987); although Holdsworth (1973) suggests that the interior basal ice is at pressure melting point.

It has been concluded that the ice cap is experiencing thinning (Hooke et al., 1987) and asymmetric retreat due to precipitation and solar radiation distribution patterns (Sagar, 1966; Løken and Andrews, 1966; Holdsworth, 1977). Mapping of end moraines by Løken and Andrews (1966) found greater rates of retreat for the northern margins of the ice cap than for the south over the last 250 years, 18 and 2.5 m yr^{-1} respectively. Recent work has confirmed these asymmetric retreat rates for the past three decades Rates of 10 to 30 m yr^{-1} were recorded for the Lewis Glacier of the north dome (Jacobs et al., 1993) compared to only 4 m yr^{-1} for the south dome (Jacobs et al., 1997). An examination of the results of Jacobs et al. (1997) reveals slightly increased amounts of retreat for the south-west facing margins of the south dome than for those facing north-

east. The overall trend is a slight north-eastward migration of the ice cap.

4.3 Radar study area

This study focuses on a 23 km long section of the north-east margin of the southern dome. The study area extends three kilometres either side of the margin, thus incorporating all ice marginal and proglacial landforms. The total area studied is 140 km^2. The area has been chosen for study primarily because of the limited local topographic variation. The surrounding terrain ranges from 425 to 625 m a.s.l., this relatively low relief makes the area an ideal location to develop the radar classification as it reduces the complications of radar layover, foreshortening and image shadowing. A body of literature specific to the ice margin morphology and glacial geomorphology and chronology of the area, provides the necessary background information for comprehension of the ice marginal dynamics. In addition to the already mentioned studies of Hooke (1973) and Goldthwait (1951), a detailed map of the glacial geomorphology of the study area was prepared by Løken and Andrews (1966). The glacial chronology of the area was reconstructed using lichenometry and radiocarbon dates from shorelines, lacustrine deltas and spillways by Barnett (1967) and Andrews and Barnett (1979).

The local geology is dominated by the granites, gneisses and shists of the Canadian Shield formed by volcanic activity 2.5 billion years ago (Thorsteinsson and Tozer, 1976). The absence of soft sedimentary strata precludes the presence of silt and

clay in the study area. Grain sizes therefore range from sand to large boulders and bedrock outcrops are common.

4.4 Data sources

A combination of data sources facilitates objective scientific investigation and allows verification of results and conclusions. The following sections describe the radar imagery, the aerial photographs, the topographic map sheets and the field data sources used in this research.

4.4.1 RADARSAT imagery

RADARSAT is an active microwave satellite imaging system that was launched by the Canadian Space Agency and the United States National Aeronautics and Space Administration on November 4th 1995. It transmits horizontal like polarized C-band (5.6 cm) pulses. In addition to the general advantages offered by radar remote sensors, RADARSAT has a variety of beam modes and look angles which enable imagery to be obtained over a specified area at a particular resolution and with a look angle chosen to enhance features of interest.

Three RADARSAT images of the Barnes Ice Cap were acquired during the summers of 1996 and 1997. The characteristics of each image are listed in Table 4.1, together with the weather conditions for the day of acquisition and the preceding three days. The weather data were obtained from the Dewar Lakes automatic weather recording station and synoptic surface weather maps (Atmospheric Environment

Service). From these the surface moisture conditions, waterbody surface roughness and wind distribution of lake ice at the time of image acquisition were inferred.

Table 4.1 RADARSAT image characteristics and acquisition time weather conditions

Image mode and spatial resolution	Standard 4 descending, 25 m	Standard 4 ascending, 25 m	Fine 1 ascending, 8 m
Pixel spacing (m)	12.5	12.5	6.25
Incidence angle (°)	34-40	34-40	37-40
Look direction	NNE-WSW	NNW-ESE	NNW-ESE
Scene coverage (km)	100 x 100	100 x 100	50 x 50
Multilook speckle reduction	yes	yes	no
Date	96/8/5	97/7/26	97/8/12
Time	11:31	22:11	22:15
Wind conditions	light WSW	moderate SE	light SWS
Max. Temp. Min. Temp. (°C)	4.4 -0.5	15.3 5.9	3.4 0.5
4 Day overview	cool with little or no precipitation	warm and dry	cool with light snowfall

4.4.2 Ancillary data

Aerial stereo-photographs taken in 1958 and 1961 provide detailed coverage of the study area at a scale of 1:57000. Four of these photographs were scanned and georegistered in a database to enable overlay with the radar imagery. Map sheets from field surveys in 1961 provide topographical information at a scale of 1:50000. The national topographic series (NTS) map sheets have locational accuracy of 25 m. These maps have a Universal Transverse Mercator (UTM) projection registered to North American Datum 1927, and the study area spans western zones 18 and 19. Figure 4.2 shows the NTS map sheet sections with the flight lines of the aerial photographs.

A geomorphological map of the southern dome of the ice cap was produced by Løken and Andrews (1966), which covers the study area at a scale of 1:80,000.

4.4.3 Field data

Field surveys were undertaken from July 7th to August 7th 1997 and were divided into three parts: glaciological observations, the collection of nominal training and ground truth data, and the quantitative measurement of surface roughness characteristics.

The glaciological observations included field sketching and geomorphic mapping of the ice margin. Conclusions about the ice margin dynamics and paths of sediment transport were drawn from these observations. The final sketches were combined to produce a field map that was georegistered and incorporated into the database. This allowed investigations of radar response and observed supraglacial debris conditions. The map was created using GPS field control points with an accuracy of $\pm$ 100 m.

Over the four week field season 181 ground truth sites were visited and the location of each site recorded using a GPS. The data were recorded as landcover classes. At each point a qualitative estimate of the parameters which affect the backscatter response of the land surface, i.e., relief, surface roughness, moisture content and percentage vegetation cover, was made. Surface roughness was assessed at all ground truthing points in terms of percentage sediment grainsize present within a 12.5 x 12.5 m pixel representative area.

At 29 representative sites the surface height variation was measured using a terrain templet. These measurements were 30 cm transects with a horizontal resolution of 0.5 cm and a vertical resolution of 0.1 cm.
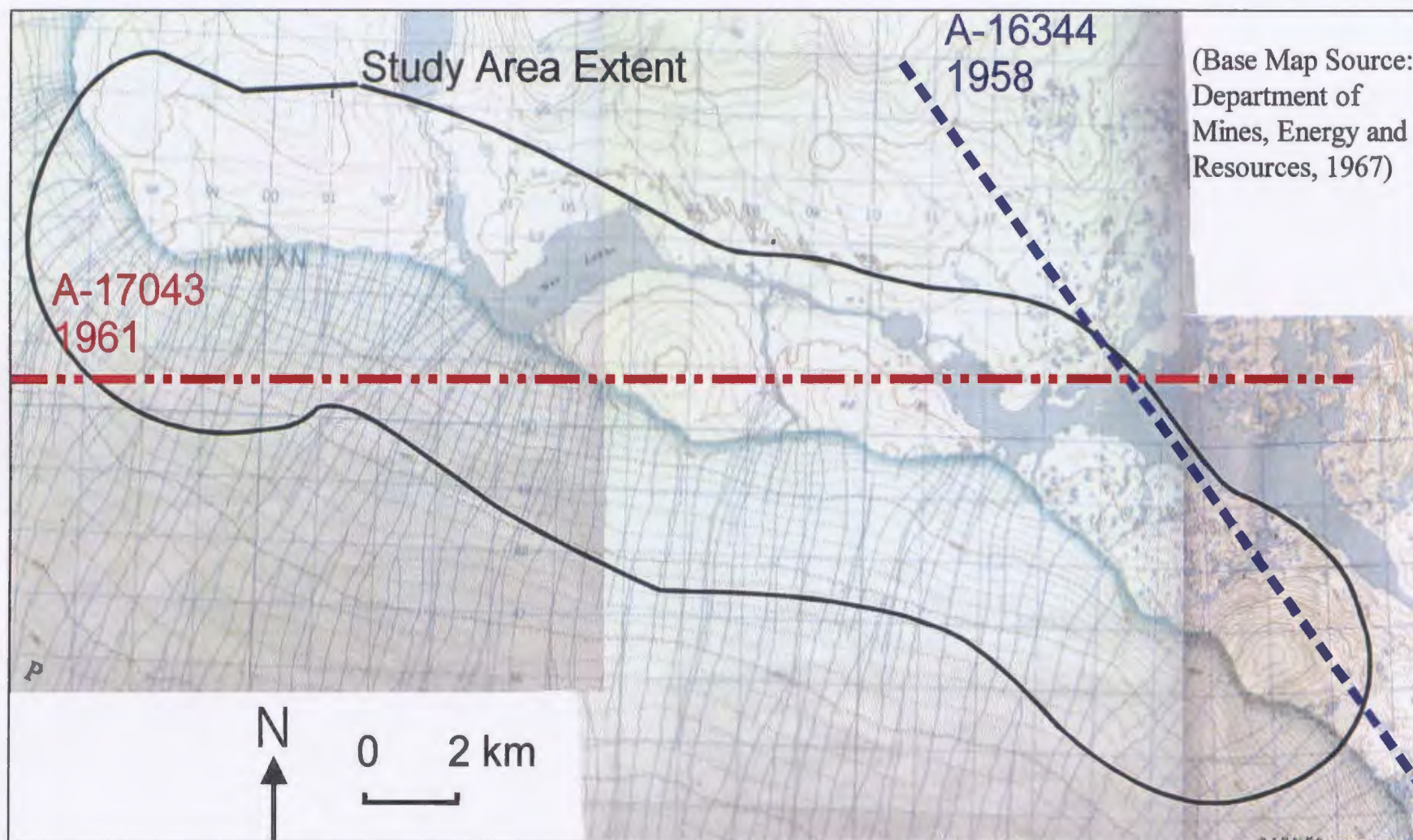
Figure 4.2 NTS map sheet sections with aerial photograph flight lines and study area extent

5. Methodology

This chapter is divided into two sections. The first section provides the details of the field methods and the second presents the sequence of image processing and the strategy of image analysis.

5.1 Field methods

A four week field season during the summer of 1997 was used to collect information about the local ice dynamics and proglacial landforms in terms of the radar parameters, training data for image classification and ground truth data for classification accuracy assessment. Observations of the length of the margin were needed to draw conclusions about the ice marginal processes of sediment transport, and to address the issue of a definition of the 'ice margin'. Measurements of surface roughness, grain size composition, vegetative cover and moisture content of proglacial surfaces were made simultaneously with the collection of training and ground truth data. Surface properties were assessed over a 12.5 x 12.5 m area marked out on the ground representative of one image pixel.

5.1.1 Field observations of the ice margin and the proglacial zone

The ice margin was observed and the landforms recorded in field sketches. Using field trigonometry and GPS coordinates as tie points for the field sketches, a scaled geomorphological map of the margin was produced with a locational accuracy of ± 100 m. This map was incorporated into the database, in order that ground truth points could be extracted for the accuracy testing of the final classification method. Observations of

ice front morphology, distribution patterns of supraglacial debris and cross sections through ice cored moraines enabled the author to objectively assess the ice marginal dynamics of the Barnes Ice Cap.

5.1.2 Collection of training and ground truth data

The coordinates of the sample points were randomly generated for the study area and the sites located in the field using a GPS and 1:50,000 topographic maps. In some cases it was physically impossible to access the randomly generated ground truth location and so additional points were surveyed at suitable substitute locations. A total of 181 points over the 140 km^2 study area were collected. This data set was then divided into two parts. One half to be used as training data and the second as ground truth data for testing the accuracy of the final classification method. General feature descriptions were collated from all the points visited by noting the gradient, feature dimensions (width, height and length).

5.1.3 Surface roughness

The terrain templet suggested by Gaddis *et al.* (1990) and Benallegue *et al.* (1995) was used to measure surface roughness. The dimensions of surface roughness required to produce specular and diffuse reflectance varies as a function of the radar wavelength and the local incidence angle, as was shown in equations 2.1, 2.3 and 2.4. Table 5.1 summarizes the surface height variations required to produce smooth and rough responses in a 5.6 cm wavelength C-band radar image with look angles of 34-40°, over

the range of possible local incidence angles.

Table 5.1 Surface height variations determining rough and smooth surfaces in a 5.6 cm radar wavelength image with look angles of 34 -40°, for possible local incidence angles

Terrain slope	Incidence angle (θ_0)	Rayleigh Criterion Threshold between smooth and rough surfaces (cm)	Modified Rayleigh Criterion Lower limit of rough (cm)	Modified Rayliegh Criterion Upper limit of smooth (cm)
0°	34-40°	0.82 - 0.87	1.48 - 1.57	0.26 - 0.28
5°	29-35°	0.78 - 0.82	1.41 - 1.49	0.25 - 0.26
10°	24-30°	0.76 - 0.78	1.37 - 1.43	0.24 - 0.25
15°	19-25°	0.74 - 0.76	1.33 - 1.38	0.23 - 0.24
20°	14-20°	0.71 - 0.74	1.30 - 1.34	0.23
30°	4-10°	0.70 - 0.71	1.27 - 1.29	0.22 - 0.23
40°	0-6°	0.69 - 0.70	1.27 - 1.28	0.22
50°	10-16°	0.70- 0.71	1.29 - 1.31	0.23
60°	20-26°	0.74 - 0.76	1.34 - 1.40	0.23 - 0.24
70°	30-36°	0.78 - 0.83	1.37 - 1.51	0.25 - 0.26

The surface roughness measurements for C-band are small, sub-centimetre scale and a 30 cm roughness profile should be sufficient to capture the features which will be affecting the radar response.

The design of the templet is shown in Figure 5.1. The templet pins are spaced at 0.5 cm intervals and pass through two guidance rods, the horizontal resolution is therefore 0.5 cm. The wooden backing board is graduated in millimetre intervals to facilitate reading of pin displacement values in the field, thus the vertical resolution is 0.1 cm. The maximum variation measurable in both the horizontal and vertical dimensions is 30 cm is, thus the templet is useful only for grain sizes smaller than 30 cm. The templet

has legs to enable it to stand unsupported on the ground surface whilst the pins find their own level.
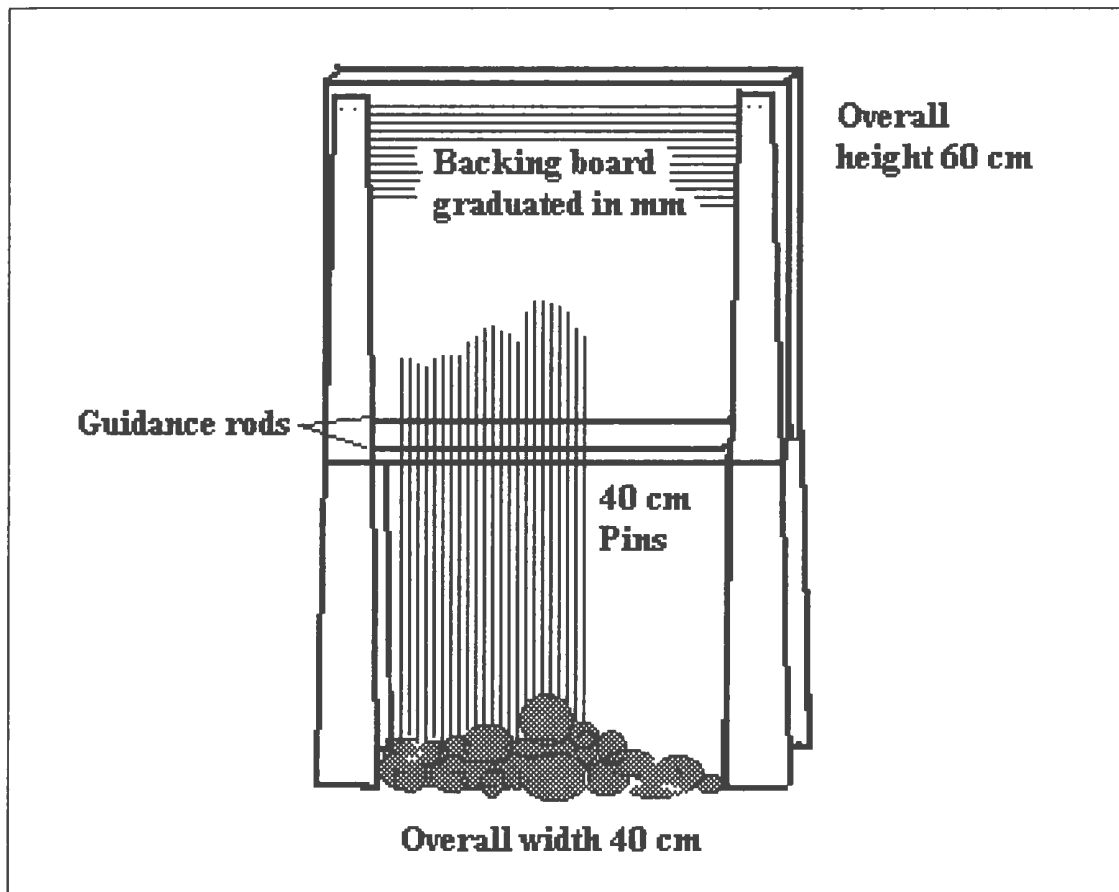
Figure 5.1 Terrain templet

Gaddis *et al.* (1990) corrected for slope angles by 'deprofiling' or normalizing the values in order to obtain true surface roughness figures. The slope of the top of the terrain templet was measured in the field with a compass-clinometer. Where slope correction is necessary the relative vertical displacement of rods across the profile as a function of the slope angle is calculated and graphed, the affected pin values are then adjusted to compensate for the slope. The final surface roughness is expressed using three parameters:

1. Standard deviation of the surface height, Sh (cm). This is the standard deviation of profile point heights after deprofiling.

2. Correlation of length, L (cm). This is the distance from the start of the profile at which the autocorrelation function first falls to ~0.37.

3. Standard deviation of surface height slope, Sp (cm/cm). This is calculated by Sh/L and has been demonstrated to be the most informative statistic when characterizing the roughness of different surfaces for identification using radar (Campbell and Garvin, 1993; Benallegue *et al.*, 1995).

A total 29 example surface roughness profiles were recorded for alluvium, residuum, bedrock, kame, supraglacial debris, ice and moraine surfaces. The selected site for the profile was as closely representative of the homogeneous pixel area as possible. According to Table 5.1 surface height variation exceeding ~1.27 cm should produce a radar response termed broadly as rough. The terrain templet is used only for surfaces with sediments of small grain size and therefore limited surface height variation. In order to capture this larger scale information surface types were also characterised in terms of grain size.

5.1.4 Grain size

Particle size and sediment composition plays an important role in controlling surface configuration and the moisture retention properties of a landform, it is therefore

an indirect control on the radar response. At each field site percentage surface cover by grain size was visually estimated within the 12.5 x 12.5 m marked pixel area. The grain size classes are the Udden-Wentworth size classes (Lindholm, 1987) and the class divisions are given in Table 5.2.

Table 5.2 Grain size categories, modified from Udden-Wentworth sediment grain sizes

Category	Long axis (cm)
Boulder	>25
Cobble	6 - 24.9
Pebble	0.4 - 5.9
Granule	0.2 - 0.39
Sand	0.06 - 0.19
Silt	0.0039 - 0.059
Clay	<0.0038

Analysis of the grain size measurements was performed in two stages. The first stage examines weighted mean radar brightness ($\beta°$) for different grain size surfaces, using the % of each grain size as the weight. The second stage examines the relationship of predominant grain size to $\beta°$. This analysis excluded any surfaces with surface slopes greater than 15° in order to reduce the effects of relief on the $\beta°$. $\beta°$ values for water and ice are included in the grain size analysis for the sake of comparison.

5.1.5 Vegetation cover

The presence of vegetation alters surface roughness and moisture characteristics and will therefore affect radar response. Percentage vegetation cover by plant type,

lichen, moss, grass, sedge, vascular plant or shrub, within the pixel area was noted at each survey point. These data are used in the general feature descriptions and densely vegetated surfaces are analysed as a separate category in the dominant grain size analysis.

5.1.6 Moisture content

Surface moisture was qualitatively assessed at all survey sites using the criteria defined in Table 5.3. These data were used in the general description of features.

Table 5.3 Soil moisture criteria

Category	Characterisation
Flooded	With pools and standing surface water
Saturated	Moisture visibly migrates when the surface is depressed
Wet	Sediment is visibly darker due to water content, boulders covered by a water film
Moist	Sediment appears dry but is damp to touch
Dry	Fine sediments crumble, larger grain sizes are dry

5.2 Image processing methodology

This section describes all stages of the image processing. Radiometric and geometric correction methods are detailed, followed by the training area selection procedure and a method of training area signature analysis. Speckle filter and texture measure algorithms are given and explained. The maximum likelihood classification algorithm is provided and the strategy of accuracy testing of the classification method is outlined. The final section explains the edge detection filtering used to extract the limit of active ice. The image processing sequence is shown schematically in Figure 5.2.
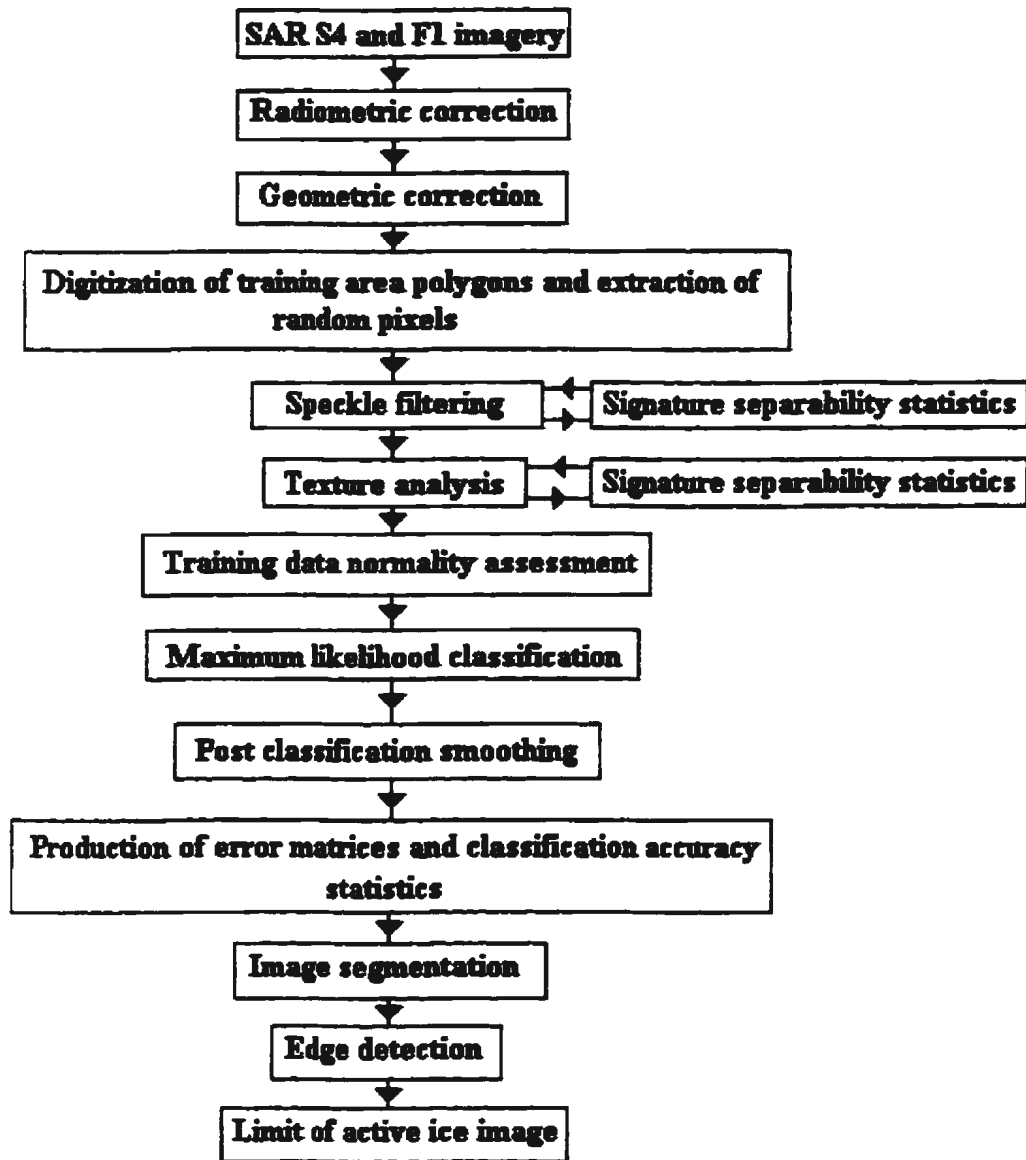
Figure 5.2 Image processing sequence

5.2.1 Radiometric correction

Radar brightness ($\beta°$) is the radar signal backscattered from the land surface and

recorded by the sensor. Radar data must be calibrated to radar brightness values in order to undertake quantitative analysis and to compare radar data from different scenes and platforms. The raw image data is supplied in a scaled format that maximises the visual interpretation potential of the image, the necessary radiometric correction is performed using equation 5.1 and the values provided in the image radiometric data record.

$$\beta^{\circ}_{k} = 10*\log_{10}[(DN_{k}^{2} + A3)/A2_{k}] \qquad (5.1)$$

where:

β°_{k} : radar brightness for pixel (dB)

DN_{k} : magnitude of the $_{k}$ th pixel from the start of the range line in the image data

$A2_{k}$: scaling gain value for the $_{k}$ th pixel from the start of the range line in the image data

$A3$: offset

5.2.2 Geometric correction

Geometric correction is the registering of the image to a known georeferencing coordinate system, in order that any point on the image may be accurately located on the surface of the earth. The procedure involves tying the image to a reference grid at a series of ground control points (GCPs). GCPs are features that can be recognised on both the image and on a map with a known reference coordinate system. The image is then transformed around the GCPs to fit the reference grid. The nature of the glacial environment means that distinctively shaped ponds, islands and stream confluences are suitable features for GCPs, although care must be taken in selecting features directly adjacent to the ice margin as they are subject to change more frequently.

As with any map, remote sensing imagery requires an attached estimate of the locational accuracy. This is derived from the accuracy of the map from which the GCPs were taken, and from the goodness of fit of the image achieved in the image registration process. This is termed the 'overall root mean square' or 'overall RMS' and is calculated using equation 5.2. It provides an estimate of the possible error associated with the location of any point on the radar image.

$$\text{Overall RMS} = \sqrt{\left(\text{locational error of GCPs (m)}\right)^2 + \left(\text{image registration error (m)}\right)^2}$$

(5.2)

The GCPs were taken from NTS map sheet with locational accuracy of 25 m, thus all GCPs are accurate to within 25 m with respect to the map sheet. The standard mode radar image has a spatial resolution of 25 m, thus no feature with dimensions less than 25 m will be identifiable in the image. Consequently, the accuracy of the final image cannot exceed 25 m. Although the fine mode image has 8 m spatial resolution the accuracy is still constrained by the 25 m accuracy of the map sheet. Overall RMS values were in the order of 25 to 35 m.

A second order polynomial was used to fit the radar image to the UTM tie points. The second order transform corrects for distortion in the range and azimuth directions, but not for vertical distortion. As the study area has relatively low relief it is satisfactory to correct in these two dimensions only. The nominal pixel sizes of 12.5 and 6.5 m for

standard and fine mode imagery respectively, are preserved in the resampling of the corrected image. The fitting of the image to the UTM grid involves nearest neighbour resampling of pixel values. In this method there is no pixel averaging and so the original data is preserved.

5.2.3 Training areas

Training areas are areas identified on the image for which the landcover characteristics have been established using ancillary data sources. Sample image statistics derived from these areas are used in the investigation of speckle filter performance, texture measure performance and in the final classification. Field surveys provide UTM coordinates of points of known landcover types and training area polygons are digitized on screen around these points. Random pixels are extracted from training area polygons to reduce the effects of spatial autocorrelation on training image statistics, as recommended by Campbell (1981), Genderen and Uiterwijk (1987) and Wilson (1992). Each landcover class has approximately 300 training pixels.

5.2.4 Image statistics and signature separability

The analysis of image statistics refers to an examination of the mean, standard deviation and coefficient of variation of texture image pixel values for landcover training areas. If the coefficient of variation is high the area is not homogenous and therefore not a good representation of that land cover class. It is best to minimize the coefficient of variation for training areas so that there is minimal overlap between class statistics and classes are distinguishable (Rand, 1985). In order that image class statistics are valid and

to truly separate classes, they must have unimodal and normal distributions.

Once image statistics for training areas have been extracted a comparative method known as signature separability is used to determine whether landcover classes are statistically separable or not. Signature separability values are used to identify which speckle filtered and texture images are best able to distinguish between features, and will therefore make the best classification input variables. The measure used is Jeffries-Matusita or Bhattacharrya distance (Swain, 1978) and is computed using the formula in equation 5.3.

$$J(i, j) = 2*[1-\exp(-a(i, j))] \tag{5.3}$$

and

$$a(i, j)=0.124*[Mi-Mj]^T*[A(i, j)]^{-1}*[Mi-Mj]+0.5*\ln\{(A(i, j))^{det} / \sqrt{[(Si)^{det} * (Sj)^{det}]}\} \tag{5.4}$$

where:
$J(i, j)$: Jeffries-Matusita distance between class i and j
$A(i, j)$: $0.5*[(Si) + (Sj)]$
(Si) : covariance matrix for class i, which has n channel by n channel elements
$()^{det}$: determinant of matrix
$[]^{-1}$: inverse of matrix
$\ln \{\}$: natural logarithm of scalar value
Mi : mean vector of class i, where the vector has n channel elements
(n : number of channels used)
$[]^T$: transpose of matrix

Where more than two classes are compared the average J value is calculated to quantify the separability of classes. In summary, J values of 0 - 0.1 indicate complete signature overlap. J values of 0.1 - 1.0 indicate very poor separability, J values of 1.0 -

1.9 indicate medium separability. J values of 1.9 - 2.0 indicate very good separability. The separability algorithm assumes normality in the data, therefore training area image statistics are examined to ensure this criterion is met.

5.2.5 Speckle and image filtering

The Enhanced Lee, the Enhanced Frost and the Kuan adaptive filters were found by Shi and Fung (1994) to be the most successful in a comparative study and they are investigated here for application to an ice marginal environment. All investigations of speckle filters are performed on the S4 ascending mode image. As the main feature of interest is image texture, the absolute minimum level of image filtering is desirable and so a filter window size of 3 x 3 pixels is used. This correlates with a ground area of 37.5 x 37.5 m. Image statistics and signature separabilities are used to evaluate filter performance. The choice of the 3 x 3 filter window is small compared to recommendations of 5 x 5 and 7 x 7 made by the developers of the speckle filters, however, the landforms of the ice marginal environment are small, typically with dimensions of tens of metres, and the small filter window is essential to prevent the removal of texture within small landforms.

5.2.5.1 Enhanced Lee Filter

The original Lee filter is based on the additive noise model. The filter uses a linear relationship to model image speckle as a function of the central pixel value and local variance within the filter window (Lee, 1980), pixels are smoothed by the replacement of the central pixel with the mean pixel value within the filter window,

equation 5.5. The Lee filter was modified by Lopes *et al.* (1990) to incorporate the use of thresholds, these thresholds determine which pixels are to be filtered and which pixels should retain their original values. The thresholds separate pixel values into three classes, these are: 1) homogeneous areas with low variance in the filter window, these pixels are smoothed, equation 5.5, 2) heterogeneous areas which represent image texture, these pixels are minimally smoothed, equation 5.6, and 3) isolated scatterers, in this case the original values are preserved, equation 5.7. These thresholds are defined by values of variance within in the filter window.

$$R = \mu_g \text{ when } C <= Cu \qquad (5.5)$$

$$R = \mu_g *W + CP*(1-W) \quad \text{when } Cu < C < Cmax \qquad (5.6)$$

$$R = CP \text{ when } C >= Cmax \qquad (5.7)$$

$$\text{and} \quad W = \exp(-Damp (C - Cu)/(Cmax - C) \qquad (5.8)$$

where:

$C : \sigma_g / \mu_g$

$Cmax : \sqrt{(1+2/NLOOK)}$

CP : central pixel grey level

$Cu : 1/\sqrt{(NLOOK)}$

μ_g : mean grey level in the filter window

NLOOK : number of looks

σ_g : variance in the filter window

Damp : dampening factor

The dampening factor is a constant that specifies the extent of the filtering. Small damp values produce greater smoothing, large damp values reduce smoothing and preserve edges. A dampening factor of 1 has been found to be an effective compromise

between point and edge preservation and homogeneous area smoothing by Shi and Fung (1994) and is the damp value used in these investigations.

5.2.5.2 Enhanced Frost Filter

The original Frost filter was developed by Frost *et al.* (1982) and uses the model of multiplicative noise. Multiplicative noise assumes that the brighter the image the greater the amount of speckle and so the amount of image filtering increases as the radar backscatter increases. This filter models the radar backscatter using only the local variance and excludes the central pixel of the filter window from the calculations, in this manner it can be said to be a model of scene reflectivity. Like the Lee filter it has been modified by Lopes *et al.* (1990) to perform image smoothing within three thresholds, as defined in equations 5.9, 5.10 and 5.11.

$$R = \mu_g \quad \text{where Ci} < \text{Cu} \tag{5.9}$$

$$R = Rf \quad \text{where Cu} <= C <= \text{Cmax} \tag{5.10}$$

$$R = CP \quad \text{where } C > \text{Cmax} \tag{5.11}$$

$$\text{and} \quad Rf = (G1*W1 + G2*W2 + \ldots Gn*Wn)/(W1 + W2 + \ldots + Wn) \tag{5.12}$$

$$\text{and} \quad W = exp(Damp*(C - Cu) / Cmax - C) + T) \tag{5.13}$$

where:

$C : \sqrt{(\sigma_g / \mu_g)}$

$Cmax : \sqrt{(1 + 2/NLOOK)}$

CP : central pixel grey level

$Cu : 1 / \sqrt{(NLOOK)}$

Damp : the exponential dampening factor

μ_g : mean grey level in the filter window

NLOOK : number of looks of radar image

G1. ..Gn : grey levels of each pixel in filter window

T : the absolute value of the pixel distance from the centre pixel to its neighbours in the filter window

σ_g : the variance of the grey levels in the filter window

W1 ...Wn : weights for each pixel

5.2.5.3 Kuan Filter

The Kuan filter was developed by Kuan *et al.* (1987) and is based on a linear model of signal dependent additive noise. It has the same form as the original Lee filter in that it models image noise using a linear relationship of image values and the variance within the filter window, but it has a different weighting function and, unlike the enhanced enhanced Frost and Lee filters, it has no thresholds to separate classes for filtering and preservation. All image pixels are filtered using algorithm given in equation 5.14.

$$R = CP*W + \mu_g *(1 - W) \qquad (5.14)$$

$$\text{and} \quad W = (1 - Cu / C) / (1 + Cu) \qquad (5.15)$$

where:

C : σ_g / 1

CP : central pixel in window

Cu : 1 / NLOOK

μ_g: mean grey level in the filter window

NLOOK : number of looks of image

σ_g : variance in the filter window

5.2.6 Texture Measures

Texture measure success varies with application, both first and second order texture measures have proved to be useful in different situations. Texture measures that have been found to be useful in other studies are tested for suitability in an ice marginal

environment. Six second order texture measures, angular second moment (ASM), contrast, correlation, homogeneity, mean and variance, are investigated here. Although they are all based on the GLCM approach, mean and variance may be considered very similar to first order texture measures. These six measures provide a thorough analysis of the image texture as they examine average tonal values, the amount of tonal variation as well as the nature of the tonal variation. To avoid angular dependency of the texture images, texture values are calculated for four opposing directions and averaged, as recommended by Sun and Wee (1982). All texture measure investigations are performed on the S4 ascending mode image. The texture algorithms are based on Haralick *et al.* (1973) and Haralick (1979) and are as follows:

$$ASM = \Sigma\ [p(\ g,\ h)^2] \tag{5.16}$$

ASM measures uniformity by quantifying pixel pair repetitions. High values are obtained when the grey level distribution within the texture window is constant and the area is homogeneous.

$$Contrast = \Sigma\ [(g-\ h)^2\ p(g,\ h)] \tag{5.17}$$

GLCM contrast is a measure of the difference between the highest and lowest values of a contiguous set of pixels, and therefore quantifies the amount of local variation within the image. Homogeneous regions are characterized by low contrast texture values.

$$\text{Correlation} = \Sigma \left[p(g, h) (g - \mu_g)(h - \mu_h)\right] / (\sigma_g \cdot \sigma_h)^{0.5}] \qquad (5.18)$$

Correlation measures the linear grey tone dependencies by quantifying the degree to which the rows and columns resemble each other. High correlation values imply linearity within the image window.

$$\text{Homogeneity} = \Sigma \left[p(g, h) / 1 + (g - h)^2 \right] \qquad (5.19)$$

Homogeneity measures tonal differences in pair elements. Homogeneous areas with small differences in tone therefore produce high homogeneity values.

$$\text{Mean} = \Sigma \left[g * p(g, h) \right] \qquad (5.20)$$

Mean is the average grey level value within the texture window, as determined from the normalised GLCM.

$$\text{Variance} = \Sigma \left[p(g, h) * (g - \mu_g)^2 \right] \qquad (5.21)$$

This measure is the variance of grey levels within the texture window determined from the GLCM.

where:

g : grey level row of the cooccurence matrix

h : grey level column of the cooccurence matrix

(g, h) : matrix element, i.e number of times that the same grey level of the pixel at the center of the texture window occurs at δ

p(g, h) : normalised co-occurrence matrix, ((g, h) element divided by the sum of all the GLCM matrix elements)

μ_g : mean of the row sums of the matrix

μ_h : mean of the column sums of the matrix

σ_g : variance of the row sums

σ_h : variance of the column sums

δ : spatial function

Various texture window sizes are tested to identify the optimum window size for distinguishing ice marginal textural features. Ice marginal feature dimensions are typically in the order of tens of metres, therefore texture windows of 3 x 3, 5 x 5 and 7 x 7 pixels, corresponding to ground dimensions of 37.5 x 37.5 m, 62.5 x 62.5 m and 87.5 x 87.5 m are investigated. Linear features may be hundreds of metres in length, therefore the correlation measure is examined using larger texture windows of 7 x 7, 13 x 13 and 15 x 15 pixels. Texture window performance is evaluated using texture image statistics from the training areas.

Speckle filtering has the effect of removing some image texture, the selection of the texture window size must therefore consider the effects of the speckle filter. A speckle filter window of 3 x 3 will remove texture over this area, consequently the texture measure will detect no texture over this same area. A texture window that is

larger than the speckle filter window will be best able to detect different blocks of texture within features. A texture window that is the same size as the speckle filter will be restricted to the detection of blocks of texture preserved by the speckle filter.

5.2.7 Classification method

The maximum likelihood classification (MLC) algorithm has proved to be one of the most robust classification algorithms available and it is used in this classification method. The MLC algorithm calculates a probability density surface for each image class using the mean and the standard deviation. Unimodality and normality of the training data are assumed for the calculation of class probabilities. In actuality the classifier has been found to be robust to small deviations from the normal as long as the primary requirement of unimodality is satisfied (Swain and Davies, 1978). Prior to classification all input image training data is examined for normality. If bi- or trimodality is observed then training areas are separated for the classification algorithm and merged for the production of the final thematic map.

The algorithm used is the Mahalanobis minimum distance classifier provided by Schowengerdt (1983). This algorithm allows the user to decide on the threshold values in terms of standard deviations, from which the equiprobability contours of the feature space are constructed, and the inclusion of *a priori* probabilities. One standard deviation is used as the threshold value in order to reduce the problems of substantial overlap in class image statistics and the percentage class cover, as observed in the field, is used for the *a priori* weightings.

The MLC algorithm is applied in two stages. First it is determined for each class (i=1,...,n) whether pixel X lies within the hyperellipsoid for that class, based on the following:

$$[X-Ui]^T [Si]^{-1}(X-Ui) <= Ti^2 \text{ must be true} \qquad (5.22)$$

If X lies outside all hyperellipsoids then the pixel is assigned to the null class. Where pixel X lies within two or more class hyperellipsoids the probability of membership to each class (MPi(X)) is calculated and the pixel is assigned to class with the highest probability. The calculation of membership probabilities is performed using equation (5.23).

$$MPi(X) = 1/2 (X-Ui)^T (Si)^{-1}(X-Ui) - (n/2)\log(2\pi) - (1/2)\log(Si)^{det} + \log(Pi) \quad (5.23)$$

where:

Si : the (n by n) covariance matrix for class i
$(Si)^{det}$: the determinant of the covariance matrix
n : Number of channels in the classification
MPi(X) : Probability of membership to class i for pixel X
Pi : *a priori* probability for the class
Ti : threshold value for class i
Ui : the (n by 1) mean vector for class i
X : (x1,.......xn) the (n by 1) pixel vector of grey levels
π : 3.1415
^{T} : transpose of matrix
$^{-1}$: inverse of matrix

Per pixel classifiers examine pixel values independently with no consideration of position of adjacent elements. The classification output is often disjointed with numerous erroneous pixels and can be difficult to interpret. Post classification smoothing is a form of contextual filtering and is found to improve both the visual appearance, and the final accuracy of a classified image. The use of a majority filter with dimensions equivalent to

the size of the smallest feature of interest, is recommended by Davis and Peet (1977). Classified image smoothing is performed here using a 7 x 7 pixel majority filter. The 7 x 7 pixel filter represents the maximum ground area of the smallest feature it is hoped to detect.

5.2.8 Ground truth data and performance evaluation

The three RADARSAT images are classified independently and the accuracy of each image is assessed using ground truth data collected during the 1997 field season. Additional test data sets are taken from the aerial photographs and from the geomorphological sketch map. Each classified image therefore has three associated error matrices and classification accuracies. It is important to bear in mind the structure of the test data sets when analysing overall accuracies. The composition of the test data sets is given in Table 5.4. The sketch map has entirely ice and ice marginal features. In contrast, the air photos and field data sets have large proportions of terrestrial landforms in addition to the ice and ice marginal features. The test data sets for the fine and standard mode images differ slightly due to the reduced coverage of the study area of the fine mode image.

Table 5.4 Test data set composition

	Field data		Geomorphological sketch map data		Airphoto data	
Landcover class	Standard	Fine	Standard	Fine	Standard	Fine
Water	6	6	6	6	20	20
Bedrock	2	2	--	--	8	8
Residuum	16	15	--	--	22	22
Till	1	1	--	--	--	--
Alluvium	17	17	--	--	24	25
Kame	3	3	--	--	12	12
Dump moraine	2	2	5	4	11	11
Snowbed	2	2	20	19	10	10
ICDR	7	7	19	17	18	18
SDC	4	4	56	56	54	17
Ice	10	13	61	58	36	36
Total test points	70	72	167	160	215	179

Classification performance is evaluated using the visual result and accuracy statistics calculated from the error matrix. Accuracy statistics are examined for individual classes and for each image overall. Class commission and omission errors are investigated, together with the standard producers, users, and overall accuracy statistics. Table 5.5 provides an example of an error matrix. Commission errors are the errors of inclusion of wrong classes in the classified data and omission errors are the errors of exclusion of pixels from a class. The error matrix is used to calculate the producer's accuracy (5.24), the user's accuracy (5.25) and the overall accuracy (5.26) of the classification method.

Table 5.5 Error matrix example

Ground truth data → Classified data ↓	a	b	c	d	Row marginal
a	a=a	b≠a	c≠a	d≠a	X_{a+}
b	a≠b	b=b	c≠b	d≠b	X_{b+}
c	a≠c	b≠c	c=c	d≠c	X_{c+}
d	a≠d	b≠d	c≠d	d=d	X_{d+}
Column marginal	X_{+a}	X_{+b}	X_{+c}	X_{+d}	N

where:
      = : correctly classified
      ≠ : misclassified

The producer's accuracy is the percentage probability that a pixel from the ground truth data set has been classified correctly, it is calculated by:

$$\text{Producer's Accuracy} = \left(\frac{x_{ii}}{\sum_{i=1}^{r} x_{+i}} \right) \times 100 \tag{5.24}$$

The user's accuracy is the percentage probability a classified image pixel is actually that class on the ground. It is calculated by:

$$\text{User's Accuracy} = \left(\frac{x_{ii}}{\sum_{i=1}^{r} x_{i+}} \right) \times 100 \tag{5.25}$$

The overall accuracy is the standard reporting format for image classification

accuracy and is calculated by:

$$\text{Overall Accuracy} = \left(\frac{\displaystyle\sum_{i=1}^{r} x_{ii}}{N}\right) \times 100 \tag{5.26}$$

where:

    N : total number of observations

    r : number of rows in the matrix

    X_{ii} : number of observations in row i and column i (entry on the major diagonal)

    X_{+i} : total of observations in column i

    X_{i+} : total of observations in row i

The overall accuracy provides an overall estimate of image accuracy, however, it may conceal significant variability in accuracy of classification between classes. For this reason individual class accuracies are also given. It has been suggested that the kappa statistic is a better overall estimate quantification of classification accuracy (Rosenfield and Fitzpatrick-Lins, 1986). The KHAT or Kappa statistic is a measure of the extent to which the percentage correct values of an error matrix are due to true agreement versus chance agreement (Fitzgerald and Lees, 1994). It is calculated using values from the error matrix and equation (5.27)

$$\text{KHAT} = \frac{N\displaystyle\sum_{i=1}^{r} x_{ii} - \displaystyle\sum_{i=1}^{r}\left(x_{i+} \cdot x_{+i}\right)}{N^{2} - \displaystyle\sum_{i=1}^{r}\left(x_{i+} \cdot x_{+i}\right)} \tag{5.27}$$

KHAT ranges between zero and one. The ideal case is KHAT equals one, here true agreement equals one and chance agreement equals zero. A value of 0.67 % indicates that the classifier is 67 % better than the chance classifier or random assignment of pixels. KHAT agreement values of <0.4 are poor, 0.4-0.75 are good and >0.75 are excellent (Landis and Koch, 1977). The accuracy of the final classification method is assessed using the KHAT statistic.

5.2.9 Edge detection

The limit of active ice is represented by the boundaries between ice, snowbed and debris covered ice surfaces. The boundaries are identified using image edge detection. The edge detection filter kernel has pixel weightings in opposition in order to detect changes in blocks of image values, and thus image boundary features. Image classes are assigned pixel values which, when reflected in edge amplitudes, make it possible to detect the nature of the boundary. For example, ice pixels are assigned a value of 1000, therefore all ice edges have amplitudes greater than 1000, the supraglacial debris is assigned a value of 100, therefore all ice and supraglacial debris boundaries are multiples of 100. Image classes of the deglaciated surface are assigned values of 0 to prevent spurious edges away from the ice margin. Figure 5.3 shows two example image boundaries, the edge detection kernel weightings, the kernel calculations and the resulting edge image values.

The example kernels shown in Figure 5.3 detect only boundaries with specific

orientation. In order that all possible boundaries are detected the image is filtered for edges in all directions, and the results combined to extract the edge of maximum amplitude, maximum amplitude corresponding to the most pronounced boundary between classes. The four directional filter kernels are shown in Figure 5.4.

Image Values	Edge Filter Kernel	Kernel Calculations	Resulting Edge Image Values		

Snow (value = 80)

-1	-1	-1
0	0	0
1	1	1

-3 x 80 = -240
3 x 1000 = 3000
= 2760

0	0	0
2760	2760	2760
2760	2760	2760
0	0	0

Supraglacial debris (value =100)

0	-1	-1
1	0	-1
1	1	0

-3 x 100 = -300
3 x 1000 = 3000
= 2700

-1 x 100 = -100
-2 x 1000 = -2000
3 x 1000 = 3000
= 900

-3 x 100 = -300
2 x 100 = 200
1 x 1000 = 1000
= 900

2700	900	0
2700	2700	900
900	2700	2700
0	900	2700
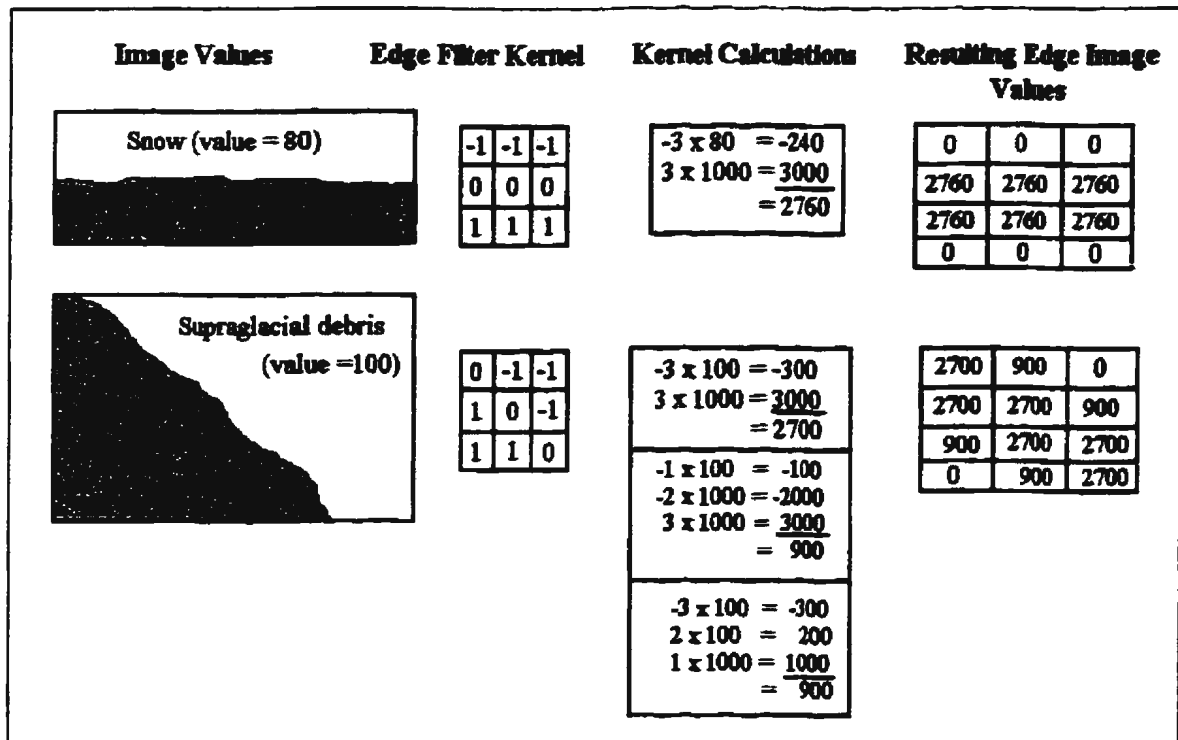
Figure 5.3 Edge detection filter examples

1	0	-1
1	0	-1
1	0	-1

Vertical

-1	-1	-1
0	0	0
1	1	1

Horizontal

-1	-1	0
-1	0	1
0	1	1

+45 degrees

0	-1	-1
1	0	-1
1	1	0

-45 degrees
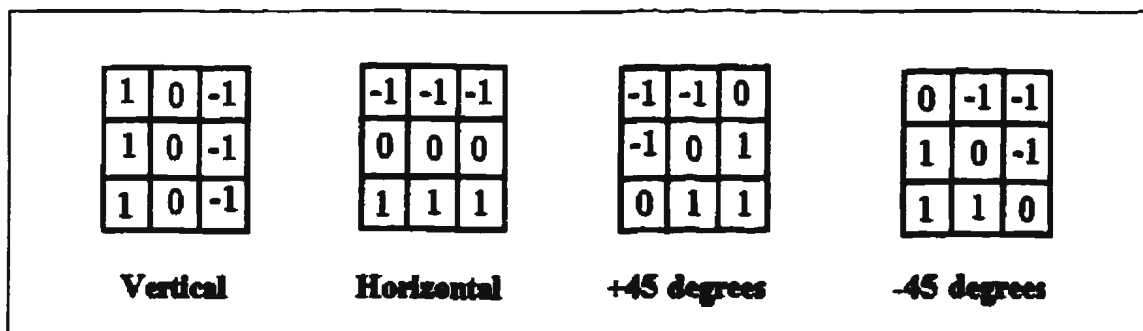
Figure 5.4 Edge detection filter kernels

In Figure 5.3 it was shown that the edge image is characterised by a double line of pixels, this double line is thinned to a single line by removing the pixels which overlap with the ice classified area. The pixel values along the line indicate the nature of the limit of active ice. An overall accuracy of the limit of active ice is calculated using equation 5.2 and the image registration error and the error associated with the line. The error of the line is assessed using field observations of feature size. A linear feature extraction programme is used to follow the line of pixels and remove short spurious edges, resulting in a line vector of the limit of active ice.

6. Field results

This chapter presents the results of the field surveys. The first section describes the observations of the Barnes Ice Cap margin and conclusions are drawn about the active ice marginal processes. The second section summarises the landforms of the proglacial zone. The final sections quantitatively analyse the surface roughness and grain size composition characteristics of the proglacial landforms and relate the roughness to radar brightness.

6.1. Observations of ice margin dynamics

Observations and sketches of the ice margin morphology were combined to produce a sketch map of the margin and to draw conclusions about the active ice marginal processes. An example segment of the sketch map is given in Figure 6.1 Observations of the ice cap itself reveal two ice surface types, wet ice where the surface has slush flows and pools, and dry ice where the meltwater is confined to incised stream channels and narrow but deep pockets. The dry ice surface is more common toward the margin as the surface assumes a gradient and the surface drainage improves. The margin of the ice cap is characterised by the following five margin forms.

1. A thin layer of supraglacial debris with a clean ice surface and a steep ice face or snowbed on the distal side, see Figure 6.2 (1).
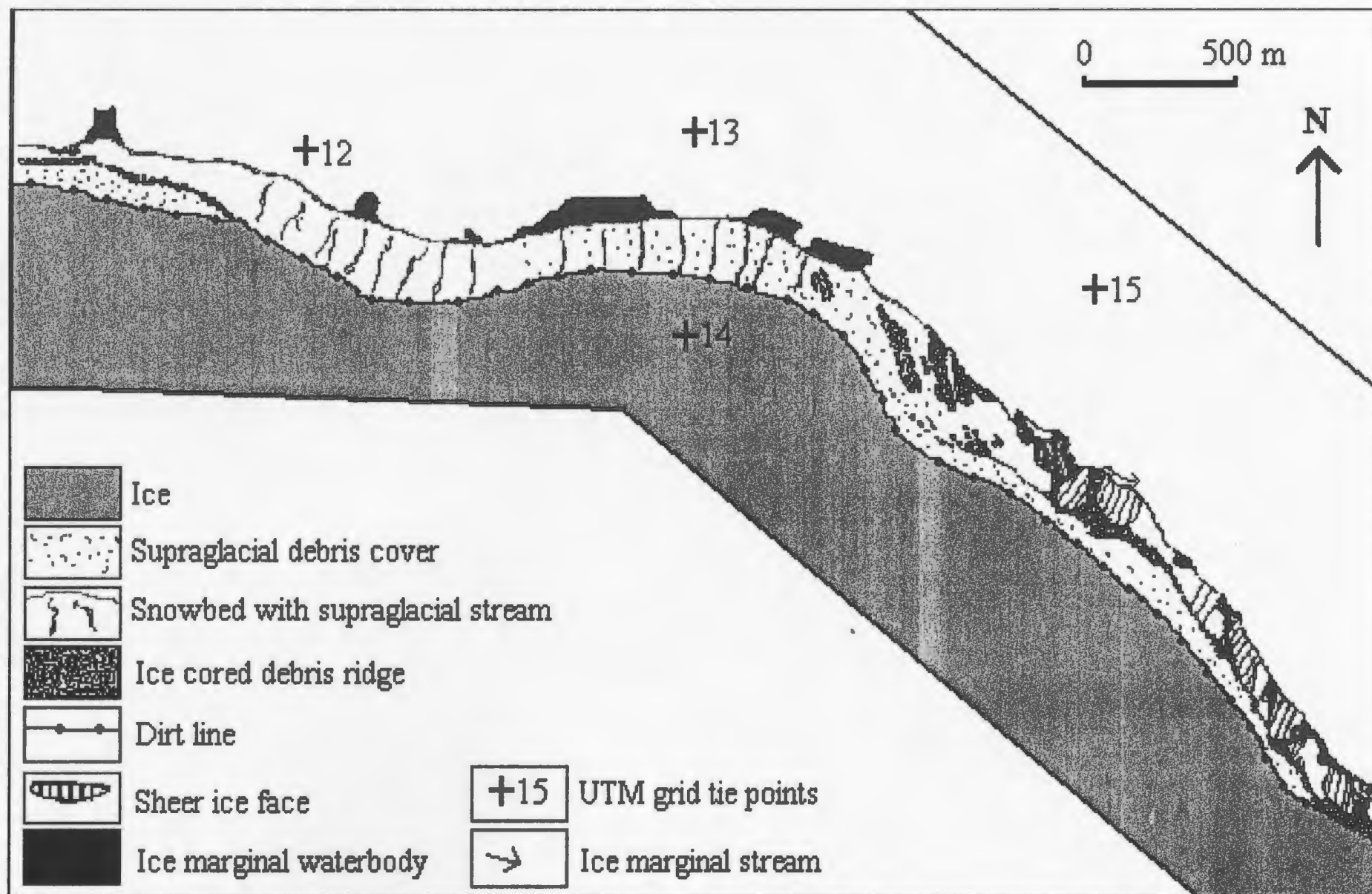
Figure 6.1 Ice margin sketch map segment

2. A low ridge of ice cored debris, up to 3 m above the relatively clean ice surface with a steep ice face or snowbed on the distal side, see Figure 6.2 (2).

3. A prominent ridge of ice cored debris more than 3 m above the debris strewn ice surface with a snowbed on the distal face, see Figure 6.2 (3).

4. A convex snowbed that is capped by a narrow band of supraglacial debris or "dirt line", see Figure 6.2 (4).

5. Clean ice cliffs that calve or melt directly into ice marginal water bodies, see Figure 6.2 (5).
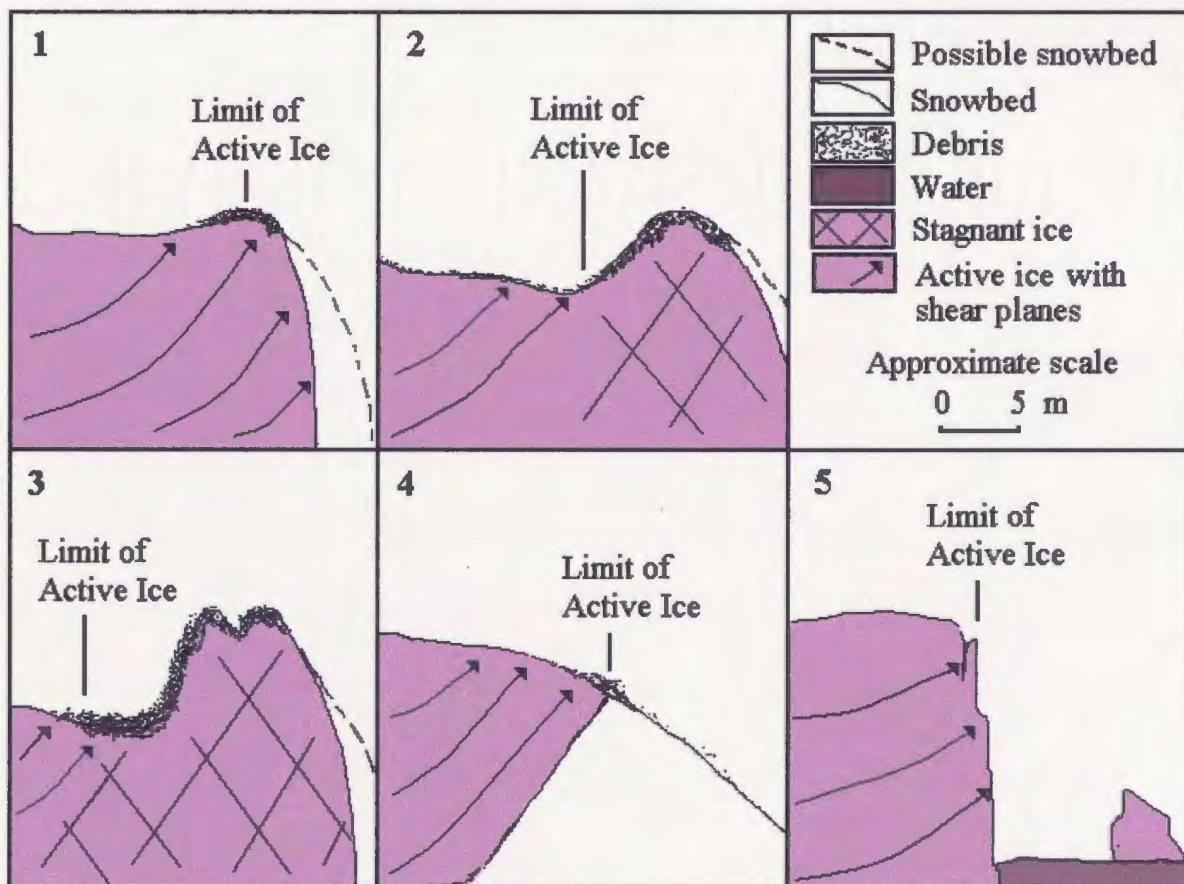
Figure 6.2 The five active ice limit scenarios of the Barnes Ice Cap margin

For the purpose of mass balance studies it is important to identify the limit of active ice. In the case of ice cliffs the limit of active ice is clear. However, where snowbeds or supraglacial debris characterise the surface the active ice limit becomes indistinct. The relative height of the ice and the amount of supraglacial debris behind the ice cored ridge is the key factor in determining whether or not the ridge is active. Where the ridge is less than three metres above the clean ice surface, it can be concluded that the ridge is underlain by active ice. Englacial debris is carried into the ridge and released therefrom, either to rest on the surface of the ridge if it is banked by a snowbed, or to fall down the distal side if the ridge has a sheer ice face. In summary, an absence of supraglacial debris behind the ridge means that the active ice limit is taken to be the ridge itself, as shown in Figure 6.2 (1)

Where the ridge is elevated many metres above the general ice cap surface, supraglacial debris is present behind the ridge and active shear planes bring material to the surface many metres back from the ridge. Here recession has caused downwasting of the ice but the insulating properties of the debris cover protect the ice core of the ridge and so it retains its elevation. In this case the ice cored ridge itself is now stagnant and the active ice limit lies to the ice proximal side of the ice cored ridge. Where there is a double ridge or large flat area of thick supraglacial debris cover, the active ice limit is suggested to lie at the ice proximal limit of this cover, as shown in scenarios (2) and (3) of Figure 6.2.

In light of the fact that some sections of the debris covered ridge may be currently active and cannot be considered as stagnant ice cored moraine, the term "ice cored debris ridge" (ICDR) is considered more accurate than ice cored moraine.

Plate 6.1 shows a cross section through an active ICDR. The debris capped ice is only a metre above the general ice surface. The vertical foliations indicate complex ice flow patterns and the crest of this ridge would be taken as the limit of active ice.

Plate 6.1 Small active ice cored debris ridge

Plate 6.2 shows a larger and more developed ice cored ridge. The ridge is more than 3 m above the ice surface and the supraglacial debris cover (SDC) behind the crest is extensive. The active ice limit for this feature would be the proximal edge of the ridge feature.

The fourth type of margin is characterized by snowbeds tens of metres high and similar dimensions thick. They are distinct from the glacier ice on account of lighter colour and density. The point at which they join the ice cap is typically marked by a 'dirt line'; this thin line of debris marking where the glacier ice begins to over-ride the superimposed ice of the snowbed, bringing debris to the subaerial surface. Plate 6.3 shows a section of ice margin with snowbeds and the characteristic 'dirt line'. In this scenario the 'dirt line' represents the limit of active ice.

It is concluded that where the ice cored debris ridge is the first surfical expression of supraglacial debris, this is taken to be the limit of the active ice and therefore the item of particular interest when mapping the ice margin. In cases where the ridge is preceded by an expanse of supraglacial debris, or it possesses a particularly wide or double form, it is concluded to be stagnant and the limit of active ice is the ice proximal limit of the debris cover.

Plate 6.2 Advanced stagnant ice cored ridge, elevated from the surrounding ice surface

Plate 6.3 Ice marginal snowbeds with dirtline

Where the convex snowbeds characterise the margin the limit of active ice is taken to be the surficial expression of the dominant active shear plane, referred to here as the dirt line.

On the basis of the described previous work and the author's field observations it is assumed that the limit of active ice is surficially expressed through the ICDR, the presence of supraglacial debris and the dirt line. These three features are therefore used to define the limit of active ice in this study. Beyond this limit is a mix of perennial snowbeds and superimposed ice which is not fed by flow from the accumulation zone. This inner placement of the limit of active ice is in agreement with Hooke (1973) and Holdsworth (1973), who state that flow at the edge of the Barnes Ice Cap is negligible within 50 m of the (visible) margin because there the glacier is thin and frozen to its bed.

6.2 Observations of the proglacial zone

The following subsections describe the observed landforms of the proglacial zones and consequently, the image classes to be used in the image classification.

6.2.1 Bedrock

Exposures of bedrock are found as small outcrops and as large expanses of washed bedrock with scattered boulders or 'boulder lag'. Streams and ponds are common on the bedrock surface and density of lichen cover is related to exposure since ice retreat. Generally the bedrock surface is dry and bare. Plate 6.4 shows a washed bedrock surface with boulder lag.

6.2.2 Residuum

Residuum characterises approximately half of the entire proglacial area. The boulders range in size from 25 cm to 2 m along the A-axis and are lichen covered to different extents depending on the length of exposure following ice retreat. Residuum occurs as large scale undulating hills, criss-crossed and modified by redundant meltwater channels. Periglacial weathering of bedrock outcrops contributes to boulder production. Plate 6.5 shows a residuum surface with a tape marking a 12.5 x 12.5 m area for scale. The large grain sizes cause residuum surfaces to be well drained and dry. Interspersed with the residuum are small pockets of colluvium. These fine sediments have been washed into slight depressions and have collected to form isolated pockets several metres in diameter. As they are smaller than a pixel area colluvium cannot be considered as a separate landcover class but is taken as a component of the residuum surface.

6.2.3 Till

Till is generally found on low gradient surfaces and forms unusually wet areas with extensive moss and grass growth. It is a diamict composed of sand, granules, pebbles and occasional cobbles, and demonstrates tundra patterned ground characteristics. Mud boils are common on flat areas and vegetation stripes are present where there is a slight gradient. Plate 6.6 shows an example of till.

Plate 6.4 Washed bedrock surface with boulder lag

Plate 6.5 Residuum

Plate 6.6 Till with evidence of sediment sorting

Plate 6.7 Kame deposit

6.2.4 Kames

Kames are sand and gravel mounds and ridges that mark the positions of former proglacial meltwater channels. In the field they are clearly distinguished by their abrupt relief and light colour due to their high sand content. Kames are dry and barren landforms, their elevation and consequent exposure to the ice cap winds, in addition to good drainage characteristics, make them unable to retain moisture and nutrients. They are consequently inhospitable to plant life. Plate 6.7 provides an example of a kame surface.

6.2.5 Alluvium

The category of alluvium incorporates all non-glacial water-lain sediments. They are varied in composition depending on the length of time since deposition, water velocities at time of deposition and current environment stability. The absence of silt and clay from the local area means that the lowest energy fluvial environments are characterised by sand and granule deposits. This is evident along lake margins, which form narrow sandy beaches devoid of vegetation, and over areas of low lying flood plain. The active floodplain is characterised by low gradient surfaces with high moisture content and extensive moss and grass growth. Areas with low risk of inundation have dense grass coverage and sedge and herb growth.

The narrow river reaches that link the lake sections and the ice marginal meltwater channels are higher energy fluvial environments. These are characterised by larger, cobble and boulder grain sizes with frequent pockets of standing water between

boulders in the riparian zone. Plate 6.8 shows the large grain sizes that form the bank of the river in the foreground and the low energy deltaic sediments on the far side of the river. Included in the alluvium class are river terraces. These stable and elevated surfaces are composed of sand and gravel between small boulders. They have good drainage and support moss, grass, herbs and woody plants. The alluvium category is generally level surfaces, fine grain sized material, high moisture content and vegetation.

6.2.6 End moraines

There are two types of end moraines within the study area, active and inactive end moraines. To the north west there is a series of nested moraines that delineate previous positions of the ice front. These moraines were first identified and mapped by Løken and Andrews (1966) and are referred to as the L&A moraines from here on. They are typically several metres wide across the ridge and between 15 and 25 m across the base, 5 to 15 m high and 100 - 1000 m long. Their predominantly sand and granule composition with intermittent larger clasts permits good drainage and so the dry surfaces support only minimal lichen and some moss colonization. An example of the L&A moraines is shown in Plate 6.9.

The second type of moraine is the actively forming terminal moraine. Frequently the morainic material is still supported by ice, but in a few rare cases the material forms an independent ridge shaped mound. Instability prohibits any vegetation cover of these features. Such ridges are approximately 5-10 m high with narrow peaks, basal widths of

less than 10 m and lengths rarely exceeding 25 m. Plate 6.10 shows an example of an actively forming terminal moraine by the process of falling supraglacial debris or 'dump'.

6.2.7 Waterbodies

Waterbodies form the final proglacial landcover category. Although usually clearly distinguishable in radar imagery some confusion is encountered in the proglacial environment due to the presence of lake ice. Lake ice pans, candling of the ice surface and the presence of icebergs complicate the radar waterbody response. This is a highly variable temporal and spatial phenomenon with daily wind patterns significantly altering the distribution of ice pans and bergs, and air temperatures altering the surface conditions of the ice.
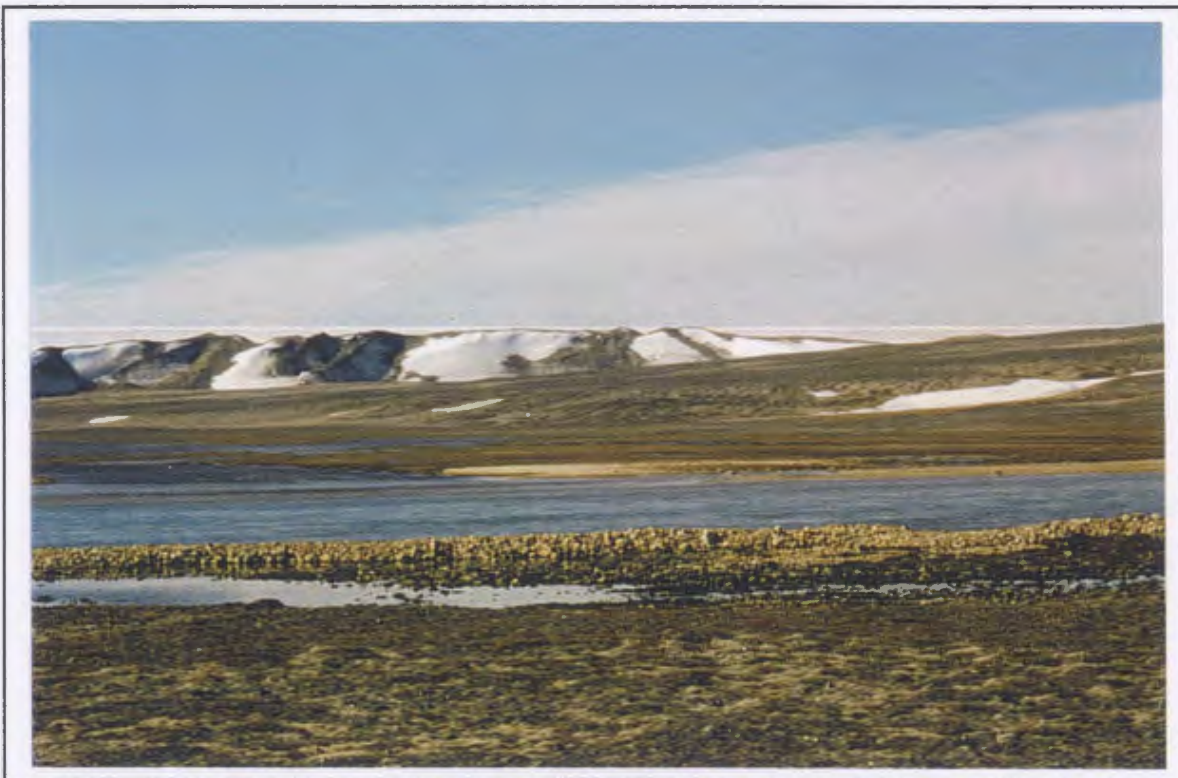
6.8 River bank and deltaic alluvium surfaces

Plate 6.9 Løken and Andrews moraine

Plate 6.10 Actively forming dump moraine at the base of a sheer ice face

6.3 Terrain templet results

Figure 6.3 presents the terrain templet measurements and the calculated standard deviation of surface height slope (Sp) for the different landcover classes. The bedrock has the lowest Sp value (0.152 cm/cm) as would be expected from a smooth rock surface. Alluvium is characterised by generally low Sp values, 0.34 to 0.43 cm/cm between the two hinges, which are characteristic of the sand and granule low energy lake margin environments and vegetated deltaic surfaces. However, the relatively large (0.23 to 1.93 cm/cm) range of alluvium Sp values is indicative of the wide variety of sediments categorised as alluvium. Kame deposits and the L&A moraines are predominantly composed of similar sand and granule grain sizes and have a similar range of Sp values (0.42 to 0.47 cm/cm).

...

6.4 Grain size results

The first stage of the grain size analysis looks at percentage grain size cover in relation to $\beta°$. The weighted mean $\beta°$ values calculated using the percentage cover as the weight are listed in Table 6.1. T-tests for the significance of difference of means were then possible between grain size classes and Table 6.2 shows a matrix of the results.

The $\beta°$ for water surfaces are significantly different from all other surfaces and should therefore be clearly identifiable in radar imagery. Ice surfaces are significantly different from surfaces composed of large grain sizes but are very similar to sand, granule and vegetated surfaces. Sand surfaces are generally well separated from the other land surfaces. Confusion is most common between bedrock, vegetation, boulder, pebble and cobble surfaces.

Table 6.1 Weighted mean radar brightness values by grain size class

Grain size category	Weighted mean $\beta°$ (dB)
Bedrock	-11.21
Boulder	-9.05
Cobble	-9.96
Pebble	-9.99
Granule	-14.27
Sand	-14.06
Vegetation	-11.49
Ice	-14.23
Water	-17.92

Table 6.2 T-test results for significant difference in mean radar brightness

Grain size class	Bould'	Cob'	Peb'	Gran'	Sand	Veg'	Water	Ice
Bedrock	2.03	2.10	2.03	2.11	3.52*	0.46	10.06*	5.68*
Boulder	—	0.86	0.88	4.59*	4.19*	2.28	14.88*	4.90*
Cobble		—	0.05	6.00*	5.07*	2.53	12.04*	8.04*
Pebble			—	5.93*	5.01*	2.47	11.92*	7.91*
Granule				—	0.23	4.43*	4.84*	0.06
Sand					—	3.15*	4.50*	0.22
Vegetation						—	4.50*	0.22
Water							—	6.10*

Bold = Significant at the 95% confidence level
Bold * = Significant at the 99% confidence level

In the second stage of grain size investigation the influence of the dominant grain size on $\beta°$ was examined. This produces a more interesting picture of class separability. Figure 6.4 is a box and whisker plot of dominant grain size class against $\beta°$.
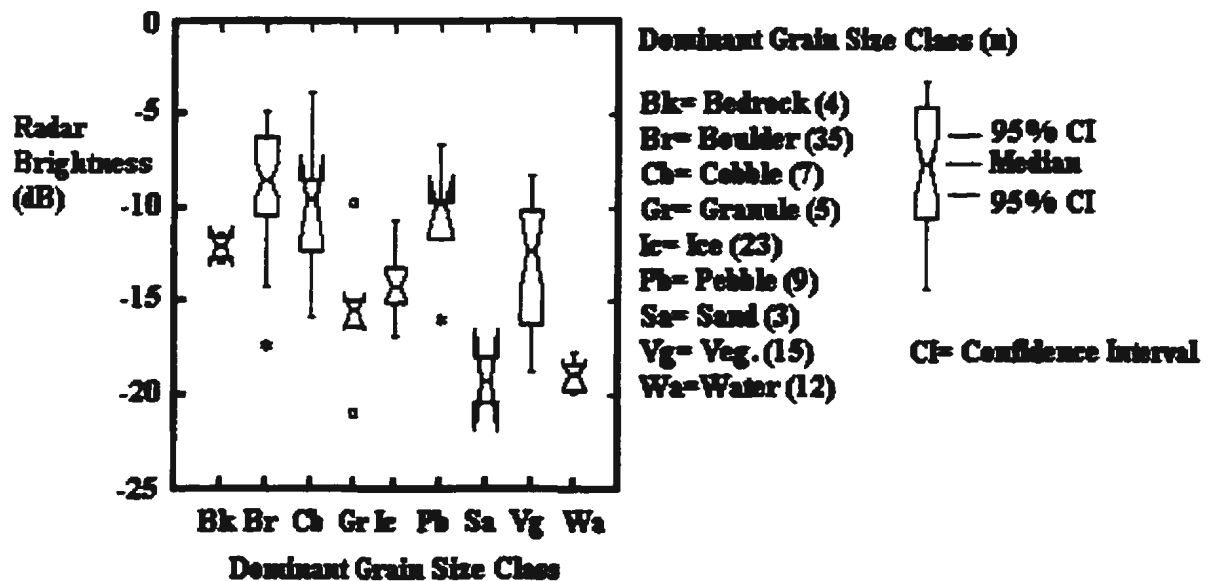
Figure 6.4 Box and whisker plot of dominant grain size class against radar brightness

Predominantly pebble, cobble and boulder surfaces are inseparable at the 5.6 cm radar wavelength. In contrast the sands, granules and bedrock surfaces are well separated with non overlapping 95% confidence intervals. There is still overlap with the bedrock and the vegetation class and with the granules, bedrock and ice. The overlap of sand and water is thought to be caused by saturation of sandy lake margins.

7. Image analysis results

This chapter presents the results of the image analysis. The accuracy of the geometric correction is given and the results of the speckle filter investigations are presented together with the final choice of filter to be applied. The texture measure investigations are summarized and the choice of classification variables is explained. Thematic map output and accuracy assessments for each of the classified images are provided. The final section presents the extracted limit of active ice.

7.1 Geometric correction

A total of 26 GCPs were used in the image registration process. The image characteristics and overall RMS for each image is given in Table 7.1.

Table 7.1 Image registration error

Image	S4, Descending, 1996	S4, Ascending, 1997	F1, Ascending, 1997
Spatial resolution (m)	25	25	8
Pixel spacing (m)	12.5	12.5	6.5
Registration error (pixels)	1.55	1.53	2.04
Registration error (m)	19.37	19.12	13.26
Map Locational error (m)	25	25	25
Overall RMS (m)	31.6	31.5	28.3

7.2 Speckle filter performance

Filtering increases tonal signature separability but removes fine texture detail. Judging the filter performance is complex as changes in texture measure performance must be judged as well as tonal averaging. Table 7.2 presents the average Jeffries-Matusita separabilities for the differently filtered images for tone alone and four texture measures.

Table 7.2 Average Jeffries-Matusita tonal and textural separabilities for three adaptive speckle filters

Image (Texture window)	Enhanced Lee	Enhanced Frost	Kuan
Tone	0.513	0.690	0.511
Mean (7 x 7)	0.658	0.957	0.654
Homogeneity (7 x 7)	0.542	0.416	0.541
Contrast (7 x 7)	0.568	0.525	0.575
Correlation (15 x 15)	0.774	0.696	0.778

The enhanced Frost filter clearly performs the most image smoothing as is shown by the increased separabilities of tone and the mean texture measure. The Kuan and enhanced Lee filtered imagery produce similar results but with slightly higher texture image separabilities. The averages provided in Table 7.2 indicate generally higher separabilities of texture images than image tone alone, and the superiority of the mean texture measure particularly when performed on the enhanced Frost filtered image.

Another method of evaluating the effect of image filtering on the performance of texture measures is to look at the number of class combinations successfully separated, by implying a Jeffries-Matusita separability of greater than 1.9. Table 7.3 shows the number of class combinations successfully separated, those poorly separated and those unsuccessfully separated for each filtered image and texture measure.

Table 7.3 Number of landcover class combinations having Jeffries-Matusita texture image separabilities of >1.9, 1.0-1.9, <1.0

Texture measure (window size)	Enhanced Lee	Enhanced Frost	Kuan
Mean (7 x 7)	1, 7, 28	7, 7, 22	1, 7, 28
Homogeneity (7 x 7)	0, 5, 31	0, 3, 33	0, 5, 31
Contrast (7 x 7)	0, 4, 32	0, 5, 31	0, 4, 32
Correlation (15 x 15)	0, 13, 23	0, 10, 26	0, 13, 23

The enhanced Lee, enhanced Frost and Kuan filters produced generally similar textural separabilities although the Kuan and Lee filters are slightly better in the cases of homogeneity and correlation. However, the Frost filter is found to far outperform the other two filters in the case of the mean texture measure, which is tentatively found to be the most effective texture measure. Due to this importance of the mean texture measure and the desired efficiency of having only one speckle filtering stage it was decided that all image processing would be performed on enhanced Frost filtered imagery.

7.3 Texture measure performance

The results of the texture image analysis and the conclusions from this section provide the basis for the decisions on the final classification input. The role of texture window size is investigated followed by a detailed examination of the six texture measures. The visual interpretation and statistical discrimination strengths and weaknesses are provided for each texture measure in order to justify the selection of classification variables.

7.3.1 Texture window size

Apart from the ASM texture measure, increasing the size of the texture window is found to increase the separability of landcover classes. This is shown by the trends in average Jeffries-Matusita separabilities given in Table 7.4. Therefore, it is decided to use as large a texture window as possible bearing in mind the size of the features. It is also considered necessary that the texture window be larger than the size of the speckle filter window to avoid detecting only the texture produced by the filtering process. Features of the ice marginal zone typically have dimensions of 10s of metres. A texture window of 7 x 7 pixels, corresponds to an area of 87.5 x 87.5 m, this is the absolute maximum ground area possible considering some of the smaller proglacial features, for the smaller dump and L & A moraines it is possibly too large. But a balance is sought for the effectiveness

of the measures and so a minor sacrifice on the part of the dump moraines and the L & A

moraines is made. A 7 x 7 window is used for all the texture measures apart from the

correlation measure. Linear features of the proglacial environment are hundreds of meters

long and so a larger texture window of 15 x 15 pixels (187.5 x 187.5 m) is used.

Table 7.4 Average Jeffries-Matusita class separabilities for six texture measures and three window sizes

Window size (pixels)	Mean	Variance	Homogeneity	ASM	Contrast	Correlation
3 x 3	0.777	0.203	0.145	0.090	0.327	--
5 x 5	0.912	0.358	0.279	0.339	0.400	--
7 x 7	0.957	0.484	0.416	0.326	0.525	0.163
13 x 13	--	--	--	--	--	0.535
15 x 15	--	--	--	--	--	0.696

7.3.2 ASM

The ASM average separability of 0.326 is the lowest of all the texture measures. No classes are well separated, six class combinations are poorly separated and 72 class combinations are inseparable. Visually the ASM texture image is difficult to interpret, The ice cap has generally lower ASM values than the non-ice categories, but landforms are not obvious and waterbodies are not clearly distinguished from the land. The only surfaces that are vaguely separable are waterbodies and dump moraines and even this class combination only has a Jeffries-Matusita separability of 1.5. ASM class separabilities are given in Table 7.5.

Table 7.5 Separability matrix for ASM texture image

	Bk	Rs	Al	Till	L&A	Km	Sw	DM	ICDR	SDC	DI	WI
Water	**1.5**	**1.2**	0.9	**1.1**	**1.2**	0.9	0.7	**1.5**	**1.1**	0.9	0.9	0.9
Bedrock		0.3	0.5	0.3	0.3	0.5	0.7	0.1	0.4	0.6	0.6	0.6
Residuum			0.1	0.0	0.0	0.1	0.2	0.4	0.0	0.1	0.1	0.1
Alluvium				0.0	0.1	0.0	0.0	0.7	0.1	0.0	0.0	0.0
Till					0.0	0.0	0.2	0.5	0.1	0.1	0.1	0.1
L &A						0.1	0.2	0.5	0.1	0.1	0.1	0.1
Kame							0.1	0.6	0.1	0.0	0.0	0.0
Snow								0.8	0.2	0.1	0.0	0.0
Dump									0.4	0.8	0.7	0.7
ICDR										0.1	0.1	0.1
SDC											0.0	0.0
Dry ice												0.0

Bold character   : J. 1.0 to 1.9
Regular character : J. <1.0

7.3.3 Contrast

Average separability for the contrast texture image is 0.525 with no classes well separated, eleven classes poorly separated and 67 class combinations being inseparable. Visually the ice surface is distinct from the land due to higher contrast values, and edge features such as lake margins, ICDR and ice marginal channels are well identified by very high contrast values. Snowbeds produce surprisingly high contrast values which make this texture measure good for separating snow from ice surfaces, but causes confusion between snow and ICDR and SDC. The contrast separabilities are given in Table 7.6.

Table 7.6 Separability matrix for contrast texture image

	Bk	Rs	Al	Till	L&A	Km	Sw	DM	ICDR	SDC	DI	WI
Water	0.3	0.1	0.2	0.0	0.3	0.5	**1.1**	0.3	**1.2**	0.5	0.1	0.2
Bedrock		0.7	0.0	0.1	0.0	0.1	0.8	0.9	0.9	0.2	0.0	0.0
Residuum			0.5	0.3	0.7	0.8	**1.3**	0.1	**1.4**	0.8	0.5	0.6
Alluvium				0.1	0.0	0.1	0.7	0.7	0.9	0.1	0.0	0.1
Till					0.1	0.3	0.9	0.4	**1.1**	0.3	0.0	0.1
L &A						0.1	0.7	0.9	0.9	0.1	0.0	0.1
Kame							0.4	**1.0**	0.6	0.0	0.2	0.3
Snow								**1.3**	0.0	0.4	0.9	**1.0**
Dump									**1.4**	0.9	0.7	0.8
ICDR										0.5	**1.0**	**1.1**
SDC											0.3	0.3
Dry ice												0.0

Bold character : J. 1.0 to 1.9
Regular character : J.<1.0

7.3.4 Correlation

The average correlation separability of 0.696 is the second highest of the six measures. No classes are well separated, sixteen class combinations are poorly separated and 62 are considered inseparable. The correlation texture image produces high values where there is linearity in the pixel values, therefore linear features are broadly separable from those features with anisotropic texture. Linear contrast features such as lake margins, rivers channels and ice marginal features such as the ICDR, the strips of SDC and the snowbeds that flank the margin of the ice cap produce high correlation values and are shown clearly on the resulting texture image. The ice surface and the land surface produce broadly similar low correlation values. Table 7.7 presents the statistical separabilities for the correlation texture image.

Table 7.7 Separability matrix for correlation texture image

	Bk	Rs	Al	Till	L&A	Km	Sw	DM	ICDR	SDC	DI	WI
Water	0.7	0.0	0.3	0.4	0.9	0.9	**1.3**	0.0	**1.6**	**1.3**	0.1	0.1
Bedrock		0.7	0.1	0.1	0.1	0.0	0.5	0.4	0.7	0.3	0.3	0.4
Residuum			0.4	0.4	**1.0**	**1.0**	**1.3**	0.1	**1.7**	**1.4**	0.1	0.2
Alluvium				0.1	0.2	0.2	0.5	0.1	0.8	0.5	0.1	0.2
Till					0.4	0.2	0.9	0.3	**1.3**	0.8	0.1	0.1
L&A						0.1	0.2	0.6	0.3	0.1	0.6	0.7
Kame							0.5	0.6	0.7	0.3	0.5	0.6
Snow								0.9	0.2	0.2	**1.0**	**1.2**
Dump									**1.2**	0.9	0.1	0.2
ICDR										0.1	**1.4**	**1.6**
SDC											**1.0**	**1.2**
Dry ice												0.0

Bold character : J. 1.0 to 1.9
Regular character : J.<1.0

7.3.5 Homogeneity

The average separability for the homogeneity texture measure is 0.418 with no classes well separated, nine classes poorly separated and 69 class combinations inseparable. Visually the image shows low homogeneity values for the ice surface and medium homogeneity values for the land surface, individual landforms are indistinguishable. High contrast edge features such as lake margins and ice marginal features are identified by their particularly low homogeneity values. The most successful separations are between surfaces of most extreme surface characteristics, the dump moraine and ICDR features produce the highest separabilities distinguishing them well from ice and other relatively smooth terrestrial surfaces. Table 7.8 shows the class separabilities for homogeneity.

Table 7.8 Separability matrix for homogeneity texture image

	Bk	Rs	Al	Till	L&A	Km	Sw	DM	ICDR	SDC	DI	WI
Water	0.3	0.1	0.1	0.1	0.3	0.4	0.8	0.4	**1.2**	0.4	0.2	0.2
Bedrock		0.6	0.0	0.1	0.2	0.0	0.3	0.9	0.6	0.2	0.0	0.0
Residuum			0.4	0.2	0.8	0.7	**1.0**	0.1	**1.5**	0.6	0.5	0.5
Alluvium				0.0	0.2	0.1	0.4	0.7	0.7	0.0	0.0	0.0
Till					0.4	0.2	0.5	0.4	0.9	0.1	0.1	0.1
L &A						0.3	0.7	**1.2**	**1.0**	0.3	0.1	0.1
Kame							0.2	**1.0**	0.4	0.0	0.1	0.1
Snow								**1.2**	0.1	0.2	0.5	0.4
Dump									**1.6**	**1.0**	0.9	0.9
ICDR										0.4	0.8	0.8
SDC											0.1	0.1
Dry ice												0.0

Bold character : J. 1.0 to 1.9
Regular character : J.<1.0

7.3.6 Mean

The mean texture measure was found to be the most effective texture measure, with an average class separability of 0.957, and eleven class pairs are well separated, 25 class pairs are poorly separable and 42 class combinations considered as inseparable. Ice, land surfaces and waterbodies are generally well separated. The mean texture image is particularly good for visual interpretation due to the preservation of the radar brightness values and real edges and linear features. The separabilities given in Table 7.9 show that the main problems are confusion between alluvium, kame, bedrock and supraglacial debris covered surfaces. Despite two distinctly different types of ice cap surface observed in the field the ice surfaces themselves were not well separated. The ice marginal features of snowbed, ICDR and SDC are not well separated.

Table 7.9 Separability matrix for mean texture image

	Bk	Rs	Al	Till	L&A	Km	Sw	DM	ICDR	SDC	DI	WI
Water	**2.0**	**2.0**	1.5	**2.0**	**2.0**	**2.0**	1.0	**2.0**	**1.9**	1.6	**2.0**	**2.0**
Bedrock		1.1	0.3	0.7	0.3	0.0	0.7	**1.8**	0.1	0.2	0.4	0.6
Residuum			1.3	0.1	**1.8**	1.1	1.5	0.9	0.8	1.0	**1.9**	**1.9**
Alluvium				1.1	0.7	0.2	0.2	1.7	0.1	0.0	0.4	0.4
Till					1.5	0.8	1.4	1.3	0.6	0.8	1.7	1.8
L &A						0.3	1.1	**2.0**	0.6	0.7	0.5	0.7
Kame							0.7	**1.8**	0.1	0.1	0.7	0.5
Snow								**1.8**	0.5	0.3	0.7	0.6
Dump									1.5	1.5	**2.0**	**2.0**
ICDR										0.1	0.5	0.6
SDC											0.4	0.5
Dry ice												0.0

Bold character : J. >1.9
Bold character : J. 1.0 to 1.9
Regular character : J.<1.0

7.3.7 Variance

The average class separability is 0.484, with no classes well separated, 15 pairs are poorly separated and 63 are inseparable. Visually the image is difficult to interpret, ice has generally a slightly higher variance than the non-ice categories but no distinctive landforms are obvious, waterbodies have similar variance values as the land surface. The only information contained in the image is in the linear contrast features such as lake margins and ice marginal channels which have extremely high variance values. Statistically the only separable features are waterbodies and dump moraines. Waterbodies are characterised by low variance and the dump moraines have abnormally high variance, all other surfaces are characterised by medium variance values with overlap and poor separability. The values shown in Table 7.10 show that very few separabilities are above 0.5 and these are confined to the dump moraines, waterbodies and ICDR.

Table 7.10 Separability matrix for variance texture image

	Bk	Rs	Al	Till	L&A	Km	Sw	DM	ICDR	SDC	DI	WI
Water	**1.7**	**1.5**	**1.3**	**1.3**	**1.6**	**1.2**	**1.2**	**1.8**	**1.5**	**1.4**	**1.2**	**1.3**
Bedrock		0.0	0.3	0.1	0.5	0.1	0.1	0.4	0.4	0.4	0.5	0.6
Residuum			0.1	0.0	0.3	0.0	0.1	0.5	0.4	0.2	0.2	0.3
Alluvium				0.1	0.0	0.1	0.2	0.9	0.7	0.0	0.0	0.1
Till					0.2	0.0	0.1	0.7	0.5	0.1	0.1	0.2
L &A						0.2	0.4	0.0	0.9	0.0	0.1	0.1
Kame							0.0	0.1	0.4	0.1	0.1	0.2
Snow								0.4	0.3	0.3	0.3	0.4
Dump									0.0	**1.0**	**1.1**	**1.2**
ICDR										0.8	0.8	0.9
SDC											0.0	0.0
Dry ice												0.0

Bold character : J. 1.0 to 1.9
Regular character : J. <1.0

7.3.8 Summary

The ASM and variance measures produced relatively poor class separabilities and are not used for classification. The mean texture measure performed exceptionally well and is selected for input to the classification process. The correlation measure is selected on account of its reasonable performance and the unique information about image structure that it contains. The contrast and homogeneity measures separate the same classes with a similar amount of success. Therefore either homogeneity or contrast will provide information to the classification method and only one need be chosen.

Training area statistics are examined for unimodality and normality as a prerequisite for the classification input and classes are subdivided where necessary. The contrast measure is found to have the greatest deviation of class values from normality. Significant negative skew is present in most of the contrast training data sets. Homogeneity value distributions are closer to normal and therefore, despite just slightly lower class separabilities, this measure is selected as the third classification variable. The three selected texture measures of mean, correlation and homogeneity provide complementary information to the classifier. The mean texture image provides information about original backscatter values, the correlation measure provides information about image structure, and the homogeneity image provides information about the surface variability. Of the six tested measures no other measure appeared to provide significant additional information and so other classification variables are

deemed unnecessary. The mean, correlation and homogeneity texture images as used in the final classification method are shown in Figures 7.1, 7.2 and 7.3 respectively.

No texture measure was able to distinguish between the two different observed ice surfaces, separabilities of consistently less than 0.1 suggest signature merging. Ice is therefore examined as one category in the classification. The Løken and Andrews moraines were also a poorly separable class. These moraines are important proglacial features and would have been useful for mapping former extents of the ice cap, however, they are not necessary for mapping the contemporary ice margin and, on account of their high level of confusion, they are omitted from the final classification method.
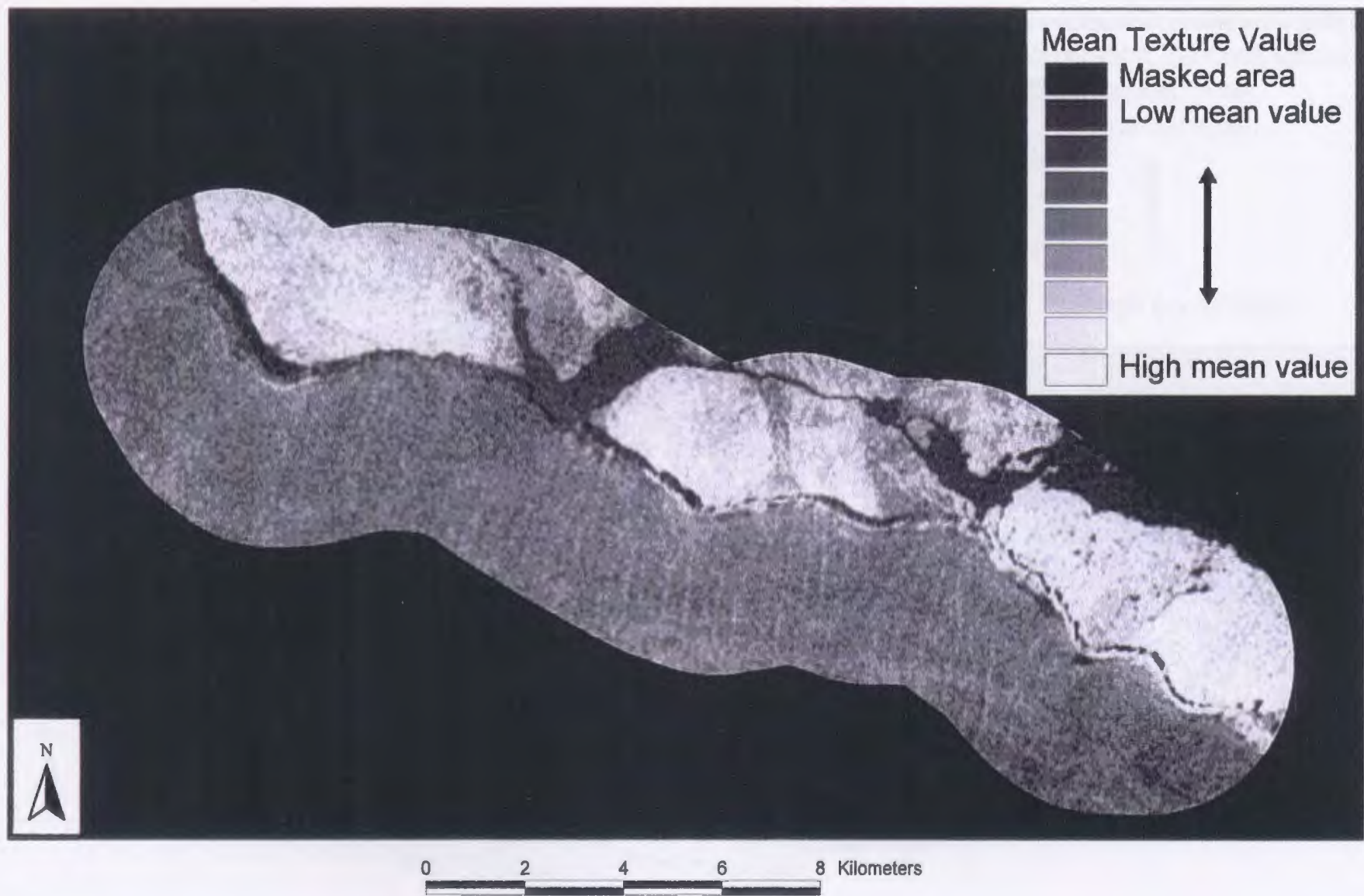
Figure 7.1 Mean texture image
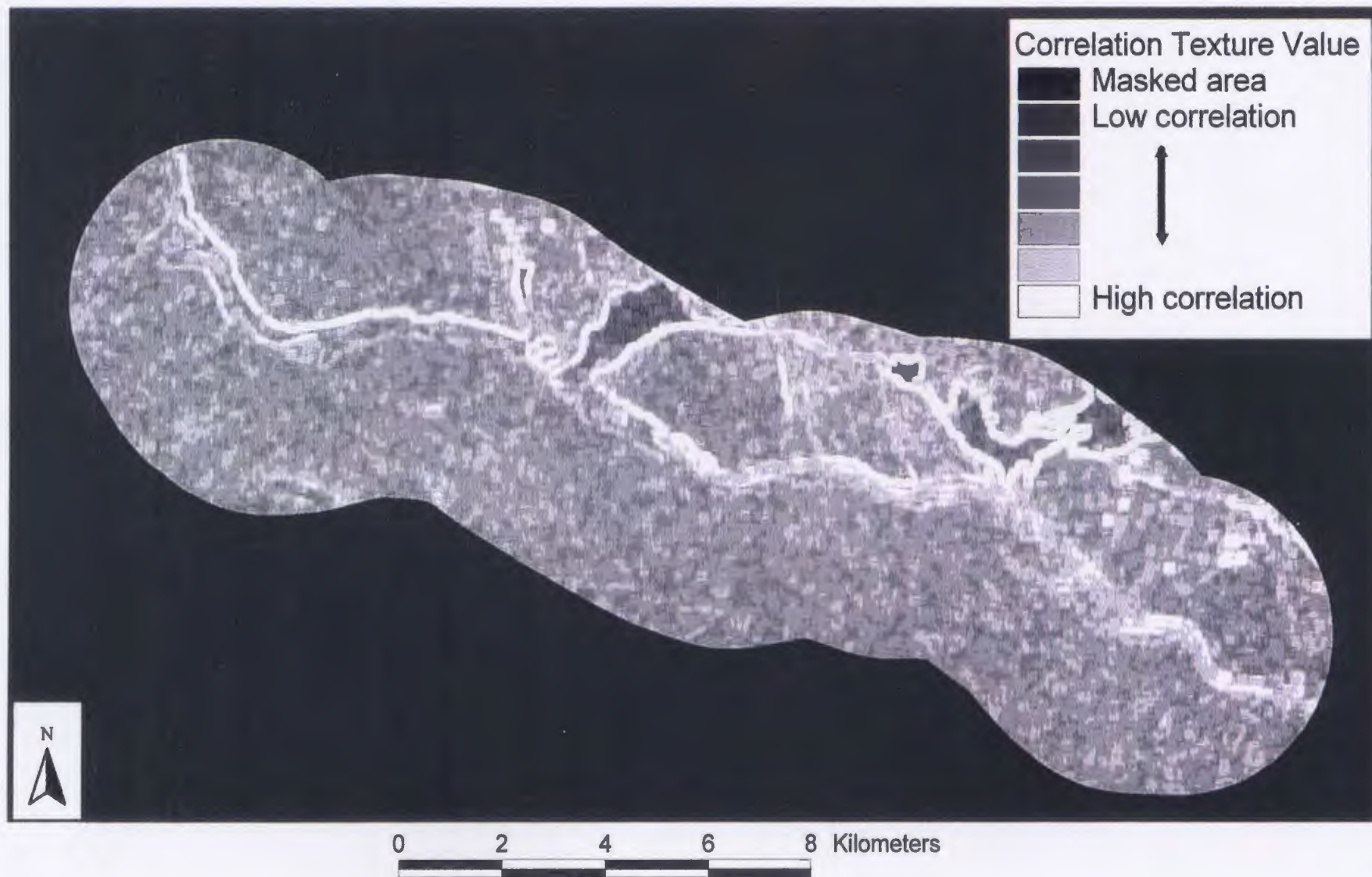
Figure 7.2 Correlation texture image
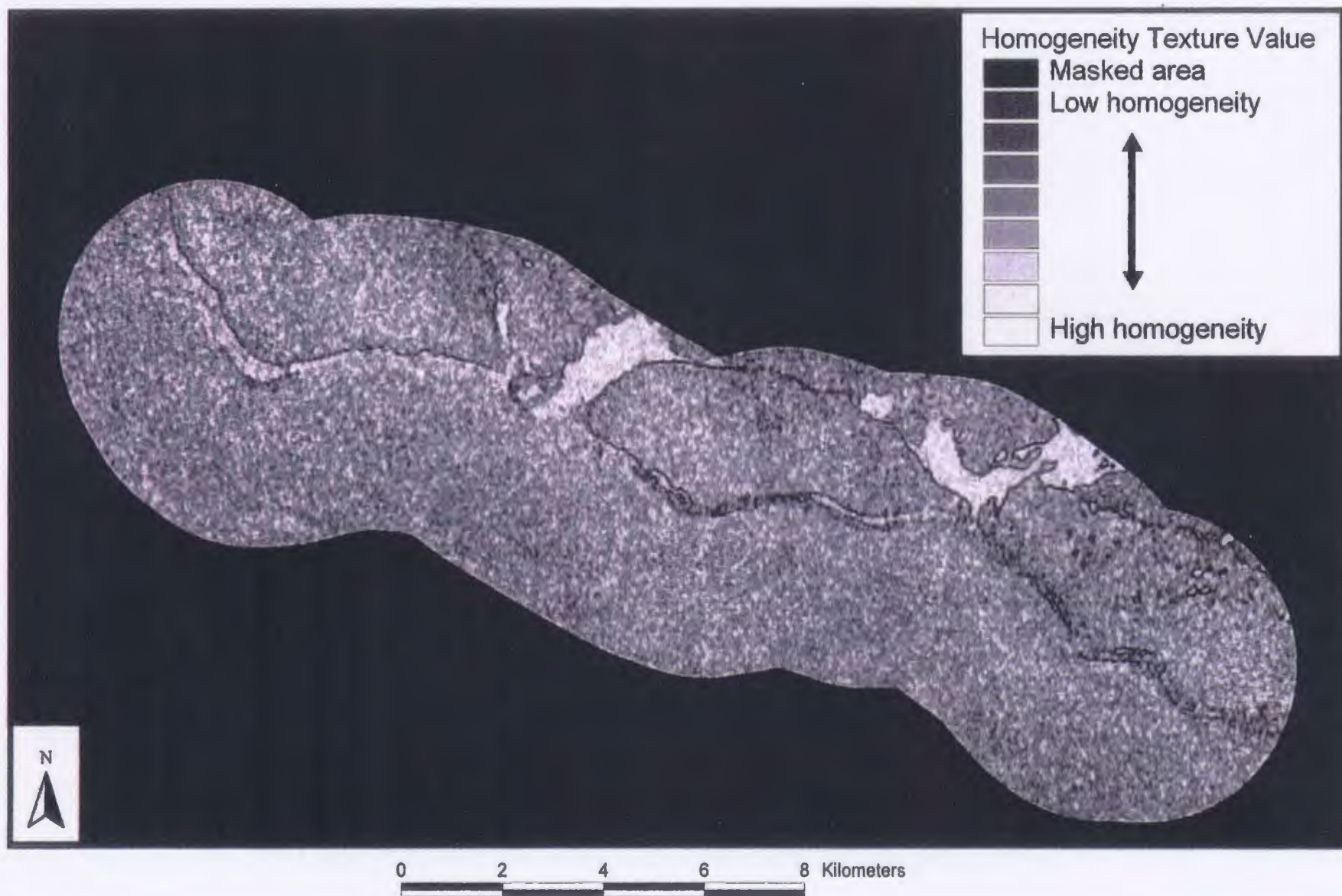
Figure 7.3 Homogeneity texture image

7.4 Image classification and accuracy assessment

The land cover classes as identified in the field and their possible subsets, are listed in Table 7.11. These classes are the basis of the supervised classification. The percentage cover of each class is included in the table for input as *a priori* weightings in the classification, as recommended by Strahler (1980).

Table 7.11 Ice marginal landcover classes

Landcover classes (% cover)	Possible subclasses
Open water (5)	Standing Flowing With ice cover
Bedrock (5)	With boulder lag Scoured with ponds
Residuum (25)	
Till (1)	Saturated Damp
Alluvium (5)	Saturated lake margins Low energy lacustrine deposits High energy fluvial Deltaic sediments River terraces
Kame (1)	Hummocky Ridge
Dump moraine (1)	
Snow (1)	Saturated Dry
Ice with supraglacial debris (SDC) (1)	Bare ice with intermittant debris Thick supraglacial debris cover
Ice cored debris ridge (ICDR) (1)	
Ice cap (50)	Wet ice with surface pools and slush Dry ice

The following subsections present the resultant thematic maps and the accuracy statistics for each of the classified images. Individual class accuracies are shown in order that the strengths and weaknesses of each image may be evaluated.

7.4.1 S4 descending image

The classified S4 descending image is shown in Figure 7.4, the associated error matrix is given as Table 7.12 and a summary of class accuracies is provided in Table 7.13. Visual inspection of the classified image shows that the margin is correctly characterised by snowbeds, with sections of ICDR and small areas of SDC. The ice cap surface has some areas misclassified as bedrock but is well separated from the terrestrial surface along the margin. Lake margins are frequently misclassified as snowbeds, and river channels are misclassified as ICDR. An area of lake ice is correctly classified as ice. Kames, alluvium and bedrock are confused and often misclassified as ice.

Table 7.12 Error matrix of S4 descending image

Classified data	Field Data											
	Wr	Bk	Rs	Al	Till	Km	Sw	DM	ICDR	SDC	Ice	Total
Water	4	0	0	0	0	0	0	0	0	0	0	4
Bedrock	0	1	1	1	0	0	0	0	0	0	0	3
Residuum	1	0	10	4	1	0	0	0	0	0	0	16
Alluvium	1	0	0	2	0	1	0	0	0	0	1	5
Till	0	0	2	1	0	0	0	1	0	0	0	4
Kame	0	0	1	0	0	0	0	0	0	0	0	1
Snow	0	0	0	4	0	0	2	0	0	1	1	8
Dump	0	0	1	0	0	0	0	1	0	0	0	2
ICDR	0	0	0	1	0	0	0	0	5	0	0	6
SDC	0	0	0	1	0	0	0	0	2	1	0	4
Ice	0	1	1	3	0	2	0	0	0	2	8	17
Total	6	2	16	17	1	3	2	2	7	4	10	70
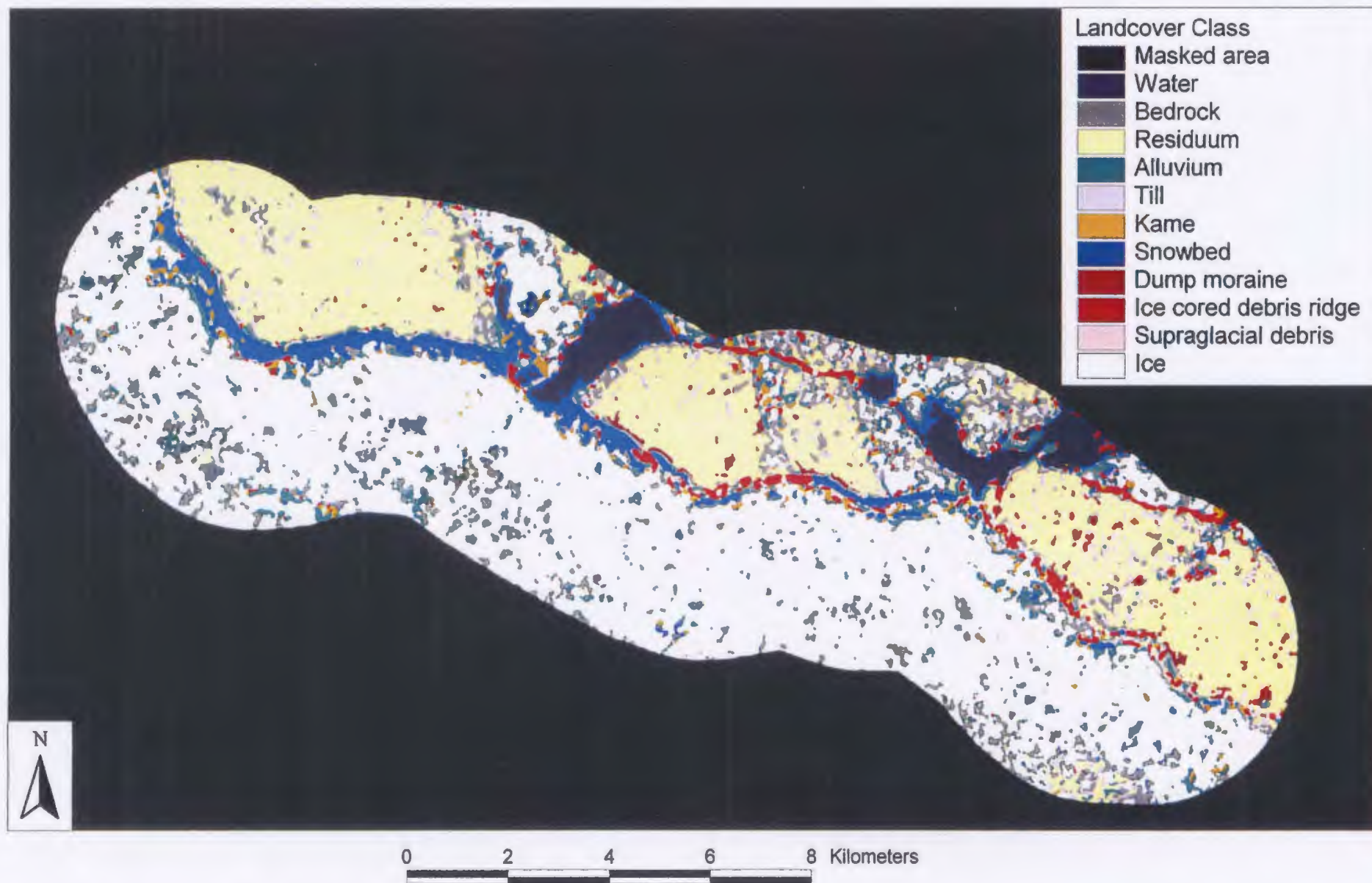
Figure 7.4 Classified S4 descending image

Table 7.13 Class accuracies and coverages of S4 descending image

Class	Producer's accuracy (%)	User's accuracy (%)	Relative area (%)	Area (km^2)
Water	66.7	100.0	3.2	4.8
Bedrock	50.0	33.3	8.2	12.3
Residuum	62.5	66.7	22.6	34.0
Alluvium	11.8	40.0	5.7	8.6
Till	0.0	0.0	1.9	2.8
Kame	0.0	0.0	1.4	2.1
Snow	100.0	25.0	4.4	6.7
Dump moraine	50.0	50.0	0.7	1.0
ICDR	71.4	83.3	2.8	4.2
SDC	25.0	25.0	1.9	2.8
Ice	80.0	47.1	47.1	70.8
Total	–	–	100.0	150.1

The descending image identifies the ice cored debris ridge and residuum surfaces well. Snow and ice surfaces have large commission errors. The method is unable to accurately classify till and kame deposits. Alluvium has a large omission error due to confusion with residuum, snow and ice surfaces. The percentages of area covered are in the anticipated order of magnitude as applied through the *a priori* probabilities. The overall accuracies and Kappa coefficients given in Table 7.14 demonstrate that the classification results are approximately 50% and may be considered to be in the 'poor' performance range of the Kappa statistic.

Table 7.14 Overall accuracies and Kappa coefficients for S4 descending image

	Field data	Sketch map data	Airphoto data
Overall accuracy (%)	50.0	52.7	43.7
Kappa coefficient	0.37	0.41	0.37

7.4.2 S4 ascending image

The classified S4 ascending image is shown in Figure 7.5 and the associated error matrices and accuracies given in Tables 7.15, 7.16 and 7.17. The classified image shows the presence of narrow snowbeds along some of the margin and many ice marginal channels. ICDR characterises much of the length with some areas of SDC. The ice is well represented but there is confusion of SDC and bedrock at the very edge of the ice cap. Lake margins and river channels are misclassified as snowbed and ICDR and kame and alluvium surfaces are frequently misplaced.

Table 7.15 Error matrix for S4 ascending image

	Field	Data									
Classified data	Wr	Bk	Rs	Al	Till	Km	Sw	DM	ICDR	SDC	Ice	Total
Water	5	0	0	1	0	0	0	0	0	0	0	6
Bedrock	0	2	1	5	0	0	0	0	0	1	1	10
Residuum	1	0	13	2	1	0	0	1	0	1	0	19
Alluvium	0	0	0	2	0	0	0	0	0	0	0	2
Till	0	0	0	1	0	0	0	0	0	0	0	1
Kame	0	0	1	0	0	0	0	0	0	0	0	1
Snow	0	0	0	1	0	0	2	0	1	1	0	5
Dump	0	0	0	1	0	0	0	0	0	0	0	1
ICDR	0	0	0	2	0	0	0	1	6	0	0	9
SDC	0	0	0	1	0	0	0	0	0	1	0	2
Ice	0	0	1	1	0	3	0	0	0	0	9	14
Total	6	2	16	17	1	3	2	2	7	4	10	70

Ice marginal features in the ascending image have slightly higher accuracies of classification than in the descending image. Ice, ICDR, water and residuum are well classified but the method is unable to identify till and kame surfaces. Bedrock and snow

have high errors of commission and the alluvium has 88% omission. Percentage area coverages are reasonably close to the expected areas although there is a considerable overestimation in the area classified as ice. The overall accuracies in Table 7.17 show a wide range of values, the field data Kappa coefficient is within the 'good' category, the overall accuracy is 57%, yet the airphotos and sketch map data sets produce KHAT values of 0.37and 0.3 and overall accuracies of 46 and 45% respectively.

Table 7.16 Class accuracies and coverages for S4 ascending image

Class	Producer's accuracy (%)	User's accuracy (%)	Relative area (%)	Area (km^2)
Water	83.3	83.3	5.1	7.7
Bedrock	100.0	20.0	7.0	10.5
Residuum	81.2	72.2	20.6	31.1
Alluvium	11.8	100	3.7	5.5
Till	0.0	0.0	1.0	1.5
Kame	0.0	0.0	0.7	1.0
Snow	100	40.0	3.2	4.8
Dump moraine	50.0	50.0	0.5	0.7
ICDR	85.7	66.7	2.9	4.3
SDC	25.0	50.0	3.5	5.2
Ice	90.0	64.3	51.8	77.8
Total	--	--	100.0	150.1

Table 7.17 Overall accuracies and Kappa coefficients for S4 ascending image

	Field data	Sketch map data	Airphoto data
Overall accuracy (%)	57.1	46.1	44.6
Kappa coefficient	0.51	0.30	0.37

Landcover Class
- Masked area
- Water
- Bedrock
- Residuum
- Alluvium
- Till
- Kame
- Snowbed
- Dump moraine
- Ice cored debris ridge
- Supraglacial debris
- Ice

0 2 4 6 8 Kilometers
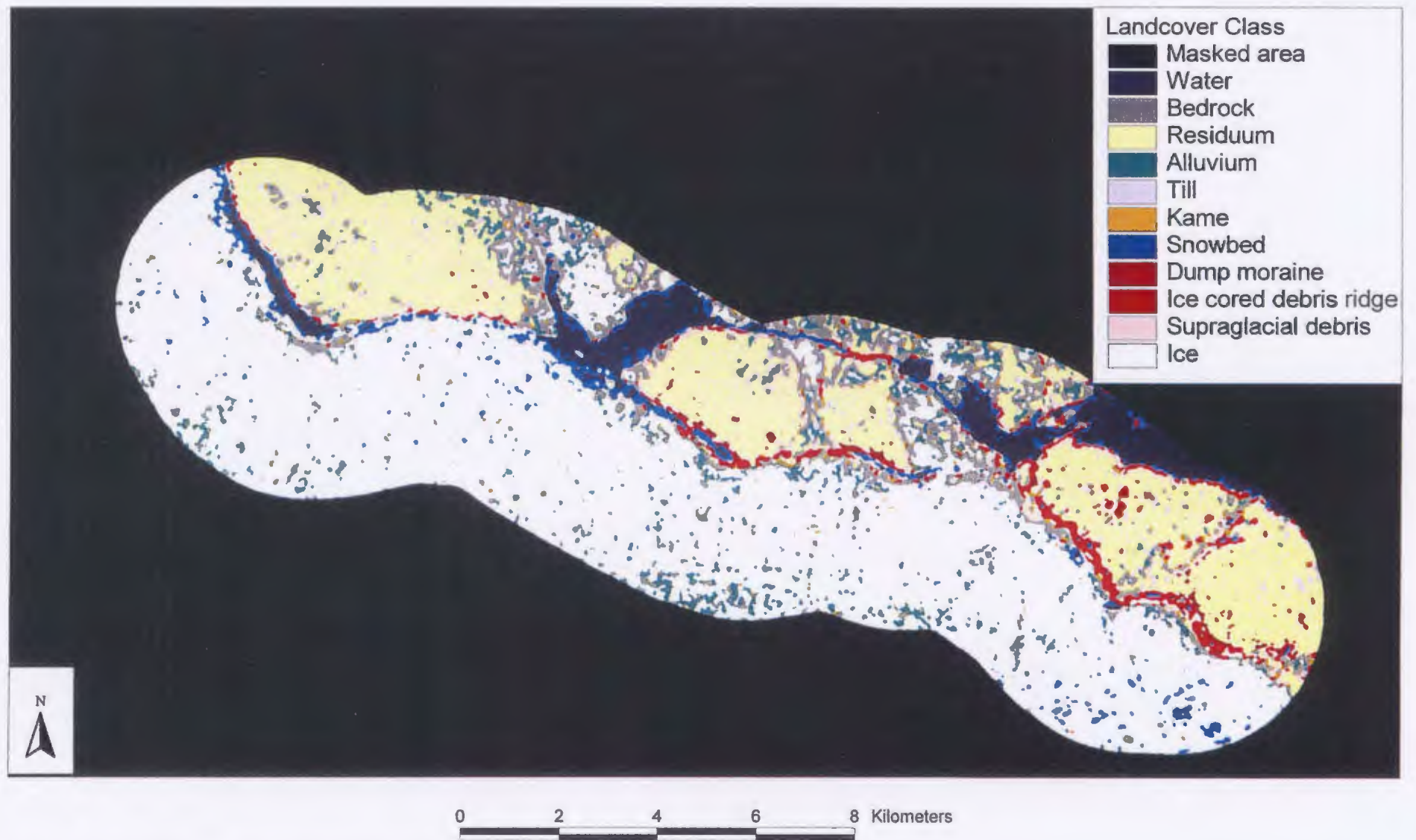
Figure 7.5 Classified S4 ascending image

7.4.3 Fine mode ascending image

The classified fine image is shown in Figure 7.6, the associated error matrix and accuracy statistics are provided in Tables 7.18, 7.19 and 7.20. Figure 7.6 shows the ice surface itself is well classified although there is confusion in a certain area with residuum. The margin is characterised by snowbed and ICDR, standing water and a minimal proportion of SDC. The same confusion of lake margins and river channels as snowbed and ICDR is apparent as in the other images. Similarly kame, alluvium and bedrock surfaces are confused with each other and with ice.

Table 7.18 Error matrix for the fine mode image

Classified Data	Wr	Bk	Rs	Al	Till	Km	Sw	DM	ICDR	SDC	Ice	Total
		Field	Data									
Water	4	0	0	0	0	0	0	0	0	0	0	4
Bedrock	0	0	2	4	0	1	0	0	0	2	0	9
Residuum	1	0	9	1	1	0	0	1	0	0	1	14
Alluvium	0	1	1	4	0	0	0	1	0	0	0	7
Till	0	0	0	0	0	0	0	0	0	0	0	0
Kame	0	0	0	0	0	0	0	0	0	0	0	0
Snow	1	0	0	2	0	0	0	0	0	0	0	5
Dump	0	0	0	1	0	0	2	0	0	0	0	1
ICDR	0	0	0	2	0	0	0	0	7	2	0	11
SDC	0	0	0	0	0	0	0	0	0	0	0	0
Ice	0	1	3	3	0	2	0	0	0	0	12	21
Total	6	2	15	17	1	3	2	2	7	4	13	72

The fine image identifies the ice surface particularly well and shows a clearly the large areas of residuum. However, the supraglacial debris, dump moraine, snowbed, till and kame surfaces have 100% omission errors. ICDR and ice have large errors of commission. The percentage coverage of classes is far from the expected with considerable over classification of ice and residuum areas.
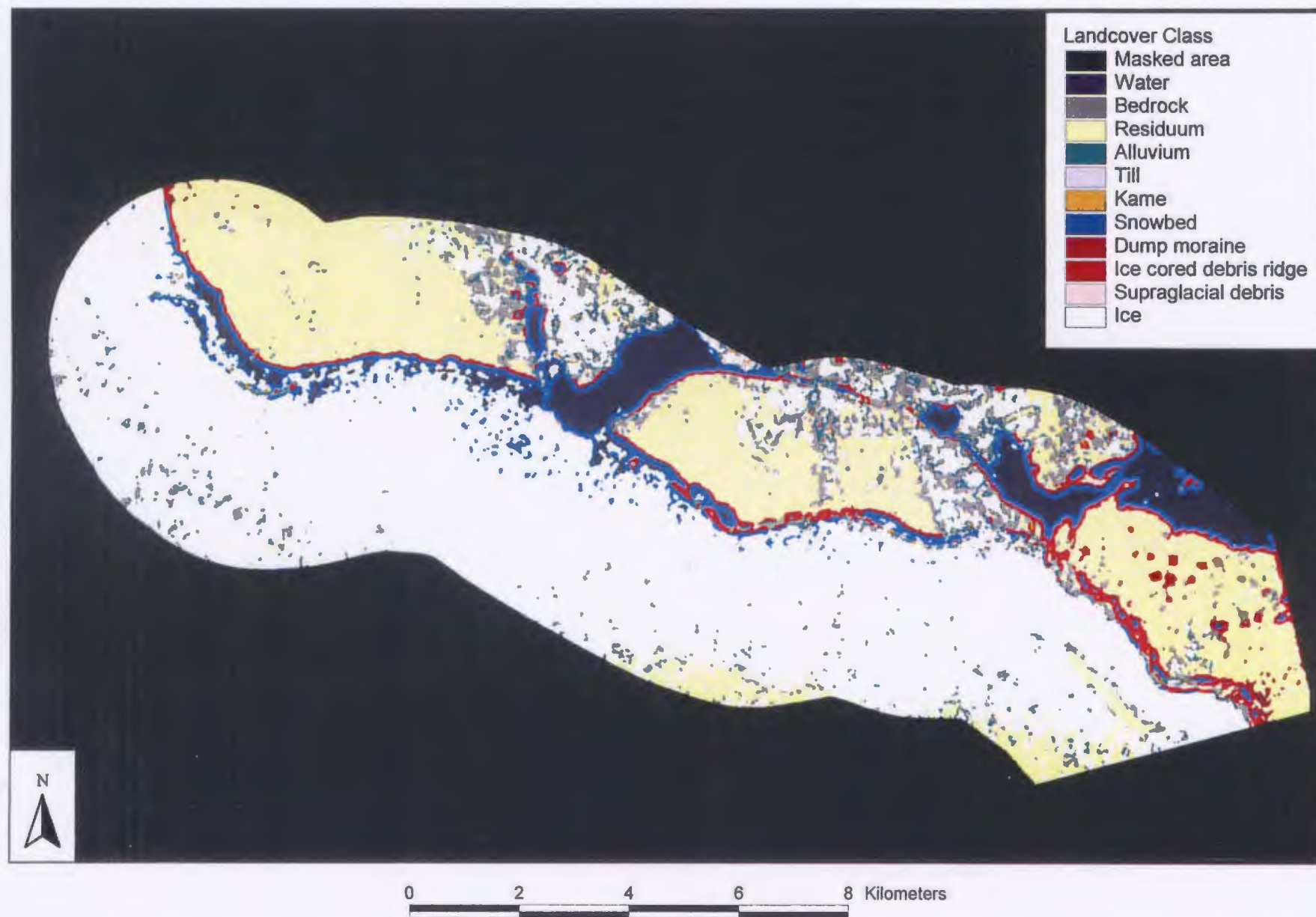
Figure 7.6 Classified fine mode image

The overall accuracies shown in Table 7.20 are relatively high with 52.8%, but this cannot be considered as truly representative of the success of the classification method. The range of the Kappa coefficients, 0.26 to 0.43, is a better indicator of the poor classification. The finer spatial resolution does not seem to enhance the accuracy of the classification method.

Table 7.19 Class accuracies and coverages of fine mode image

Class	Producer's accuracy (%)	User's accuracy (%)	Relative area (%)	Area (km^2)
Water	66.7	100	4.4	6.4
Bedrock	0.0	0.0	4.3	6.3
Residuum	60.0	69.2	29.2	42.5
Alluvium	23.5	57.1	2.7	4.0
Till	0.0	0.0	0.4	0.5
Kame	0.0	0.0	0.2	0.2
Snow	100.0	40.0	4.3	6.3
Dump moraine	0.0	0.0	0.4	0.6
ICDR	100.00	63.6	3.4	4.9
SDC	0.0	0.0	0.9	1.2
Ice	75.0	42.9	49.8	72.5
Total	--	--	100.0	145.4

Table 7.20 Overall accuracies and Kappa coefficients of the fine image

	Field data	Sketch map data	Airphoto data
Overall accuracy	52.8	42.5	52.8
Kappa coefficient	0.39	0.26	0.43

7.5 Edge Detection

The limit of active ice is represented by the boundaries between the snowbed, SDC, ICDR and ice image classes, as discussed in chapter six and shown in Figure 6.2.

Edge detection is used to identify these class boundaries in the image. The edge detection is performed on the S4 descending image. A standard image is used because of the higher classification accuracies than with the fine mode image. Despite the slightly higher overall classification accuracies of the ascending image, the descending image is superior for the edge detection procedure because the landforms around the ice margin are better identified. In the classified ascending image there is a break in the margin where a major supraglacial stream cuts through the ICDR. The immediate alluvium and bedrock surfaces are misclassified as ice and the result is that ice appears to spill out of the ice cap in a spurious lobate form. Such a misrepresentation of the ice margin is avoided by using the descending image.

The misclassification of the ice as alluvium, bedrock and kame surfaces is overcome by converting their image values to those of ice. The true ice cap is then extracted from the image using an ice polygon size criterion, spurious off ice polygons are small and therefore removed from the image. Misclassified pixels upon the ice cap are thus incorporated into the ice mass. The edge detection is performed upon an image containing only the classes of ice, snowbed, ICDR and SDC, specific image values are assigned to each class and all other pixels are assigned a value of zero.

The final edge image is shown in sections in Figures 7.7, 7.8 and 7.9, the limit of active ice is characterised by the four different types of ice margin. Figure 7.10 shows the extracted vector lain over the original radar image. The limit of active ice is characterised

by 45 % snowbed, 17 % ICDR, 13 % SDC and 24 % classified as 'other', essentially water or residuum.

Where the ice directly adjoins open water or the deglaciated terrain, the placement of the limit of active ice is within one pixel. The width of the ICDR is between 2 and 10 m, therefore where the ice adjoins the ICDR we can be confident that the limit of active ice is also within one pixel. Where the ice adjoins a snowbed the limit of active ice may be displaced ice proximally as some active ice shear planes are apparent ice proximal to the true 'dirtline'. Such shear planes are observed to occur within a maximum of 20 m of the true 'dirtline' and so any displacement of the active ice limit is unlikely to exceed two pixels. Accuracy of the ice and snowbed limit is thus within two pixels or 25 m. Where the active ice limit is characterised by SDC it is possible that active ice shear planes may extend beyond the beginning of the SDC for up to 30 m, the accuracy of this type of limit is within three pixels or 37.5 m. Using the maximum error of placement of the line (37.5 m) and the error associated with the image registration (31.6 m) the overall RMS error of the limit of active ice is calculated to be 49 m.
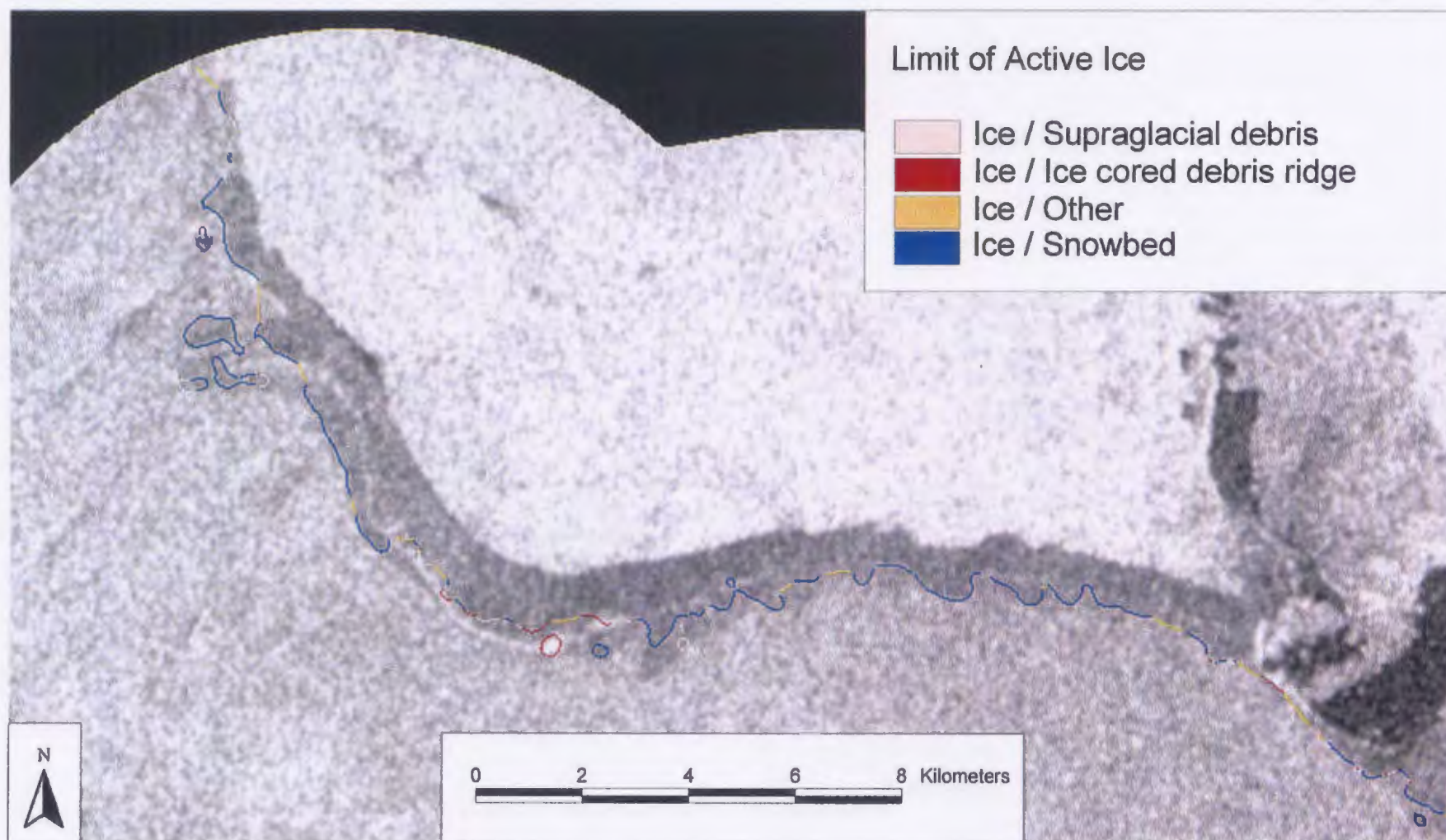
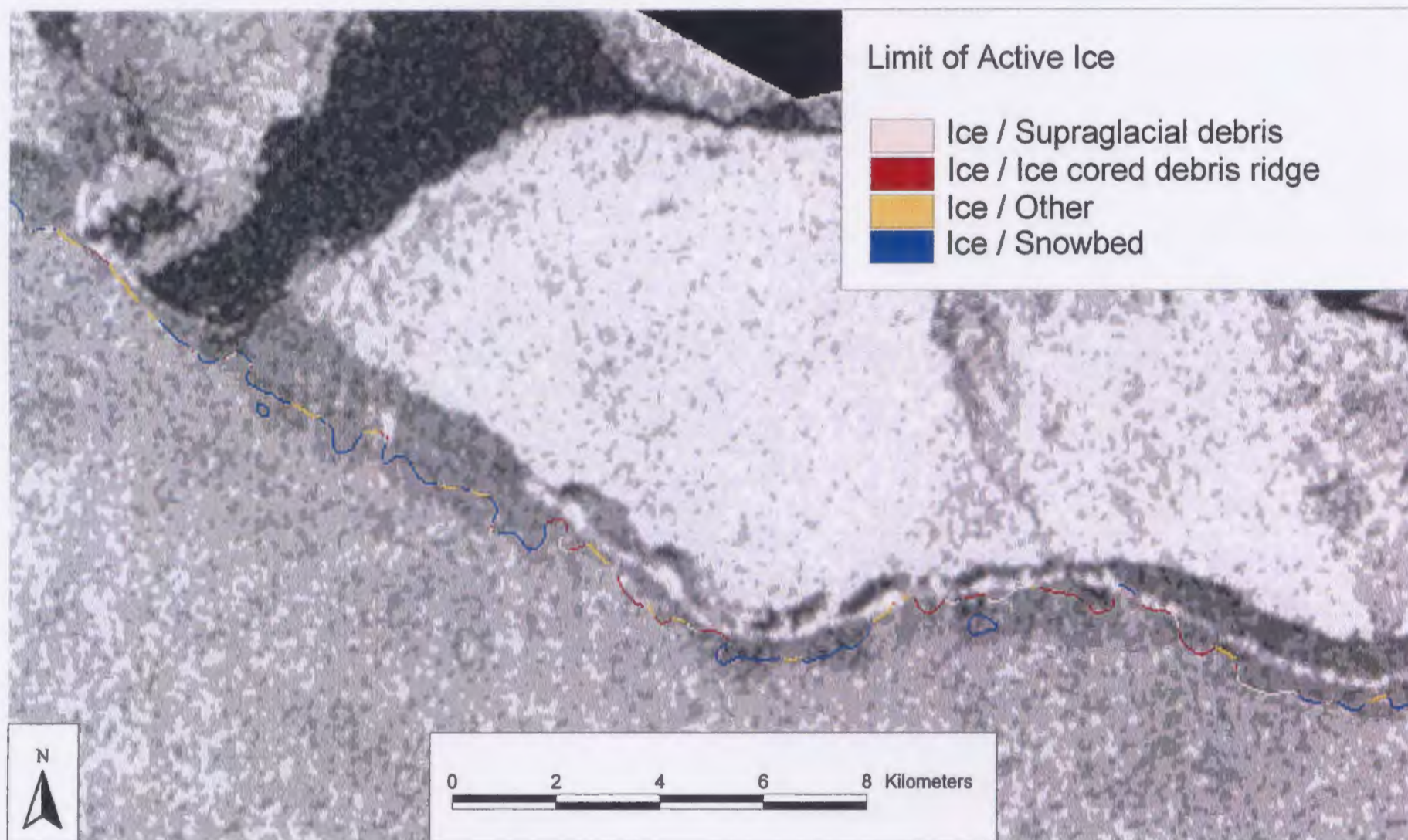Figure 7.7 Limit of active ice for the west section of the study area

Figure 7.8 Limit of active ice for the middle section of the study area
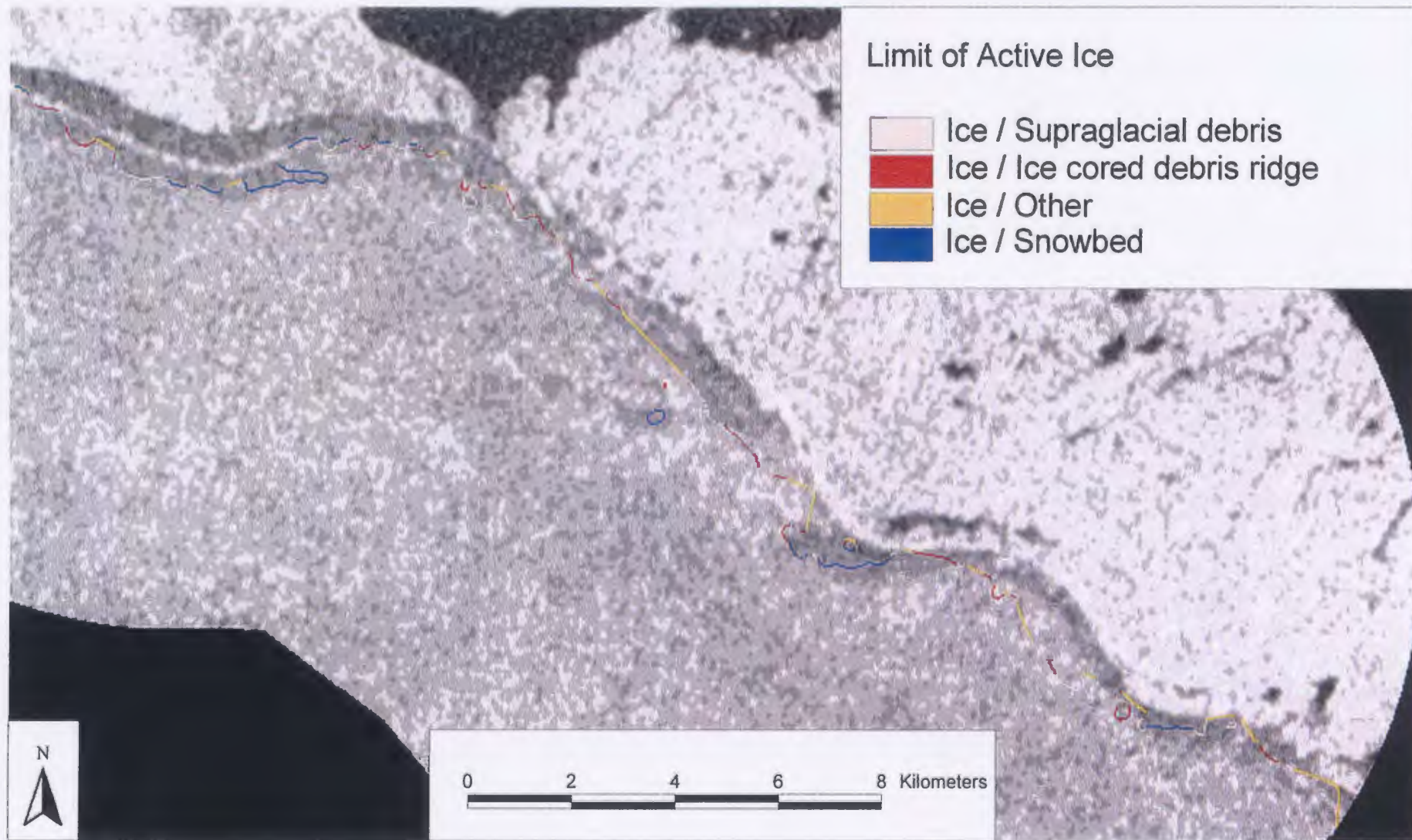
Figure 7.9 Limit of active ice for the east section of the study area

Figure 7.10 Limit of active ice as a line vector lain over the original radar image

8. Discussion

This chapter discusses the results of the field investigations and the image processing. The strengths and weaknesses of the method are explored and where possible, recommendations for further studies are made. Comparison with results from other studies provide an objective evaluation of this research.

8.1 Glaciology and remote mapping of ice margins

The importance of the nature of the ice margin, in ice margin mapping applications of remote sensing, is emphasised by the research completed here. As ice marginal processes vary spatially, initiating a variety of ice front morphologies, the more specific 'limit of active ice' is introduced as an alternative to the general term 'ice margin'. The limit of active ice is considered to be more accurate as it excludes stagnant ice at the margin and therefore gives a better estimate of contemporary ice extent. It is suggested that future ice margin mapping studies should describe the nature of the margin and clearly state the feature that is mapped as the 'ice margin'.

8.2 Image classification and orbital characteristics

This research set out to assess the potential of SAR imagery for classification of an ice marginal environment and for the delineation of the extent of active ice. Image classification was accomplished but was considerably more successful for the features of the ice margin than for the proglacial environment. Consequently, whilst it is possible to

delineate the limit of active ice from a classified image, it is not possible to classify all landforms of the proglacial zone using SAR imagery alone.

The differences in the classification results of the three RADARSAT images highlight the role of the image look direction and the spatial resolution. The descending orbit illuminates the surface from an off ice perspective looking 'upglacier'. In this manner the ice distal slopes of the ICDR, with or without snowbed cover, and ice marginal features such as dump moraines and meltwater channels form the foreslope features and are well detected. Waterbodies and bedrock surfaces are clearly identified in the descending image. Ice proximal ICDR slopes and SDC surfaces are sometimes in shadow and less reliably identified. This is reflected in the low overall accuracy (46%) of the sketch map test data set. On the other hand, the terrestrial surfaces are well identified and the overall accuracy of the field data test set is 57%.

The ascending orbit illuminates the surface from a 'downglacier' perspective, hence, the ice, SDC and ice proximal slopes of ICDR are well detected. Distal slopes of steep ICDR and snowbeds are backslope features and subject to shadowing, the land surface immediately adjacent to the ice cap is less reliably classified. However, since the proximal slopes of ICDR and the SDC cover are the primary features of interest when mapping the Barnes Ice Cap limit of active ice, these illumination conditions are optimal. The S4 ascending image produced the highest classification accuracies. The sketch map

accuracy is 53% and the field and airphoto test sets produce slightly lower accuracies of 50% and 44% respectively.

The accuracies show that the look direction has a significant impact on the features that are successfully identified. Illumination from a 'downglacier' perspective produces higher classification accuracies for the features of importance in the mapping of the limit of active ice. It should be noted however, that these are the characteristics of the Barnes margin and are not necessarily valid for all other ice masses. In addressing the secondary objective of identifying the optimal look direction for ice margin mapping, it is concluded that the selection of the orbital path must be made using knowledge of local ice dynamics and the features of importance in the placement of the limit of active ice.

The fine mode image has massive overclassification of residuum and ice, the percentage coverages are far higher than the anticipated coverages assigned through the *a priori* weightings. The field and airphoto test data sets have large proportions of these two categories and so produce the highest accuracies, both with 53% overall accuracy. Despite the optimal 'downglacier' illumination, the accuracy of the ice features as reflected in the sketch map accuracy is low, only 42% compared to 53% for the standard mode image.

This reduction in accuracy is predominantly due to the misclassification of dump moraines and SDC. Dump moraines are misclassified as residuum or alluvium and the

SDC surfaces are misclassified as bedrock or ICDR. It is suggested that the misclassification of SDC occurs at the finer spatial resolution because SDC responses separate more distinctly into smooth ice and thick debris cover, rather than being an average of the two surfaces. These responses are then more likely to be confused with smooth bedrock and rough ICDR. The SDC has a vital role in the delineation of the limit of active ice and so it is concluded that the fine image is the least useful for ice margin mapping. The fine image does not prove any more useful for other landcover types and as with the standard mode, kames and till are misclassified. There is no significant improvement in the accuracies of alluvium and residuum, and the bedrock surfaces are more frequently misclassified in the fine mode image. With regard to the study objective to identify optimal spatial resolution it is concluded that 25 m spatial resolution is superior to 8 m spatial resolution.

The decrease in classification accuracy of the fine mode image may be related to the increased amount of image speckle. The standard mode images have multilook speckle reduction, in contrast the fine image is a single look image. Although all the images were filtered for speckle using the enhanced Frost filter, fine mode images may require an increased amount of adaptive speckle filtering compared to standard mode images.

8.3 Edge detection

The limit of active ice is characterised by four edge types: ice adjoining snowbed, ice adjoining ICDR, ice with beginning of SDC and ice adjoining any other surface, such as open water or immediate terrestrial surface. It is acknowledged that the accuracy of this line is entirely dependent on the accuracy of the classification method used in the derivation of the edge detection image. The overall accuracy of the segmented image upon which the edge detection is performed, which contains only the classes of ice marginal features, is 70%.

The classification problems which affect the accuracy of this line may be summarised as follows. A minor problem is observed with ICDR being misclassified as SDC. This error attaches a lower accuracy of placement (three pixels) to a limit that is actually accurate to within one pixel. The main problems are the misclassification of SDC as ice and sometimes as snow. Where SDC is misclassified as ice this would place the limit of active ice slightly distal to the beginning of the SDC, therefore slightly distal to the first active shear plane, but still within the three pixel accuracy limit assigned to this particular type of limit. Where ice is misclassified as snow, the limit would be placed ice proximal to the true limit of active ice, thus underestimating the true extent of active ice. As 45% of the resulting edge image is classified as ice adjoining snowbed, this latter problem is considered to be the most serious. The detected limit of active ice is therefore taken to be an absolute minimum estimate of the position of the limit of active ice for the Barnes Ice Cap.

The placement of the limit of active ice is considered to be accurate to within 49 m. This is comparable to the accuracies achieved by Adam *et al.* (1997) using ERS-1 SAR data, and well within the 75 m accuracy they consider necessary for glacier hydrology studies. It is considerably more accurate than the 300 m obtained using ERS-1 SAR data for a section of the Greenland Ice Sheet (Sohn and Jezek, 1996) and the 150 m obtained using a combination of radar and multispectral data for the same area (Sohn, 1996). The results would therefore be useful for mass balance studies. The results may be considered more interesting from a glaciological perspective as they relate the ice dynamics to ice front morphology in radar imagery. With reference to the multispectral study of the Barnes Ice Cap by Jacobs *et al.* (1997) these results may be considered more accurate. The multispectral study identified the limit of clean glacier ice and then applied a 100 m buffer in order to include the ICDR and SDC. In light of this indepth field and radar study, the inclusion of the buffer zone considerably overestimated the extent of active ice of the Barnes Ice Cap.

8.4 Image processing for ice marginal spaceborne radar imagery

Of the three adaptive speckle filters it is apparent that the Kuan and enhanced Lee filters perform less image smoothing than the enhanced Frost filter and so preserve more image texture. Consequently, the Kuan and enhanced Lee filters produce slightly higher texture separabilites for most texture measures. That the Kuan and the enhanced Lee filters produce the same degree of filtering is no surprise, the Kuan filter is after all, an extension of the original Lee filter based on the additive noise model. The enhanced Frost

filter is based on the multiplicative model for speckle and is designed specifically for radar imagery. The multiplicative model states that the brighter the radar response the more developed the speckle, therefore the greater the amount of appropriate filtering. Subsequently, more filtering is performed and the Frost image is the smoothest. For the purposes of signature separability, particularly for the mean texture measure, this image smoothing has a positive effect on signature separability and so the enhanced Frost filter is deemed the most effective.

In image texture analysis increasing texture window size is found to increase signature separability. As the number of pixels used in the GLCM calculation increases, the signatures have greater capacity for variation and so become more distinct and individual. The constraining factor in choosing texture window dimensions is the size of the smallest feature it is desired to detect. For all texture image processing the texture window should be as large as possible, taking into account the size of the features of interest.

GLCM texture measures were examined to identify whether image texture could be used to distinguish between ice marginal features. No one measure could identify all landforms and different measures had success with different features. Of the six measures investigated the mean texture image is by far the most useful. Representing the average of original backscatter values it retains information about relief, surface moisture content and surface roughness. With this information it is best able to distinguish between

landcover types. Variance quantifies the amount of backscatter variation within the texture window, the resulting values are similar for many different landcover types and produce a highly confusing texture image. The ASM texture measure is the opposite of variance and quantifies uniformity within the texture window. Like the variance measure landcover class values are not distinctive and texture separabilities are low.

Contrast texture gives information about the range of image values. Features with a large range of backscatter values within their coverage, due to the effects of relief or abrupt image boundaries, are distinctive. Dump moraines and ICDR show well due to the highly contrasting values produced by steep foreslopes and shadowed backslopes. Snowbeds are narrow features often with small boulder patches of slumping debris, which produce high contrast values. These make snowbeds separable from the low contrast ice surface but cause confusion with the ICDR and SDC. Waterbody margins are very high contrast features and are well identified in the contrast texture image. The homogeneity measure quantifies the degree to which pixel values are similar and is the opposite of the contrast measure, accordingly the two measures identify the same landforms with a comparable success rate.

The correlation measure proves particularly useful as it detects linear structure and this is a key element in the ice marginal environment. The only problem is that all linear contrast features, such as stream channel and waterbody edges, in addition to the actual linear landforms such as ICDR, snowbeds and dump moraines, are detected. The

correlation image must be used in conjunction with other information in order that the linear features of interest are identified.

It appears that some ice marginal features are distinguishable in radar imagery using image texture but others are not. Waterbodies, ICDR, snowbed, residuum and dump moraines are well detected, ice and SDC are detected but with slightly lower accuracy. Proglacial features such as kames, alluvium, bedrock and till surfaces are not reliably distinguishable from each other, and are frequently confused with ice. These proglacial features have similar backscattering characteristics so they are not identifiable with the mean texture measure, they are medium contrast features, therefore they do not show up in the contrast and homogeneity texture measures, and they are anisotropic, thus they are not identified by the correlation measure.

Previous ice marginal radar studies have reported confusion of ice surfaces with proglacial alluvium (Rott, 1984) and also smooth bedrock surfaces (Shi and Dozier, 1993; Shi *et al.*, 1994) resulting in reduced classification accuracies. Despite more detailed image texture analysis, the same problems are identified in this study. It would appear that the separation of alluvium, kame, bedrock and ice surfaces will continue to be problematic for radar classification until a method of texture analysis that can recognise more complex patterns is developed. The eventual replacement of the rigid algorithms and texture windows of the second order GLCM texture measures with flexible measures more suited to natural surfaces, such as fractals, would seem desirable.

The mean, correlation, contrast and homogeneity texture measures were successful in this context but these results are not duplicated in any other study. It may be concluded that texture measure performance varies greatly with the nature of the environment being studied and the size of the texture window used. For example the correlation measure was found to be particularly useful in this study because of the natural linearity of features, whilst variance was found to be poor. In contrast, studies using larger texture windows for a more general impression of image texture over a glaciated region have found variance to produce good results (Sohn, 1996).

8.5 Surface roughness measures for radar

A secondary objective of this study set out to quantify the surface roughness characteristics of proglacial landforms and determine whether the variations in roughness would be sufficient to produce significantly different radar backscatter between features. The terrain templet derived Sp values give a good indication of the surface roughness associated with the different landcover types, despite the limited number of samples. The Sp values are low for smooth surfaces such as bedrock and high for rough surfaces such as ICDR and residuum. Ice has a surprisingly high Sp value indicative of a rough surface similar to residuum. This is due to the presence of small but deep holes on the ice surface producing large standard deviations of surface height. The Sp values for the L&A moraines, kames and alluvium overlap because they are composed of similar materials.

Consequently, similar radar brightness values and confusion in radar imagery is anticipated. In conclusion, it is not possible to distinguish between proglacial landforms on the basis of surface roughness alone.

A problem was observed in the field with the weight of the templet pins disturbing the surface materials. Where surface materials were loose, such as sandy lake margins and on wet ice surfaces, particles were dislodged and the pins found their level on the more stable subsurface. How this subsurface differed from the surface producing the radar response is difficult to assess, particularly if the surface was wet. This problem would need to be addressed in the design of any subsequent terrain templet. The length of the profile is also open to question. Theoretically, considering the radar wavelength, the 30 cm profile should have been satisfactory. However, the influence of the deep holes in the ice surface may have been reduced by using a longer profile, and the resulting ice Sp values would have been more representative of the generally smooth ice surface.

The weighted mean $\beta°$ results have large sample sizes which facilitate the calculation of confidence intervals and significance tests. The mean radar brightness values show that water is distinguishable from all other surfaces with a distinctively low $\beta°$ of ~-18 dB. $\beta°$ values for boulders, cobbles and pebble surfaces vary between -9 and -10 dB and are not significantly different, therefore confusion is likely. Bedrock and vegetation surfaces produce confused $\beta°$ values of ~-11 dB. Ice, sand and granules

produce similar $\beta°$ values of ~ -14 dB, thus one may predict classification confusion of these surfaces if using radiometric response alone. This confusion stems mainly from the fact that many of these surfaces are of mixed grain size composition, therefore both rough and smooth components are averaged over the pixel $\beta°$ value.

The surface roughness investigations proved to be less successful in the proglacial environment than for the lava flows and agricultural soils for which they were originally developed (Gaddis *et al.* 1990; Campbell and Garvin, 1993; Benallegue *et al.*, 1995). Lava flows have distinctive surface roughness on account of the thermal mechanics of lava cooling and agricultural soils are distinctive by the method of tillage. Proglacial landforms are the same materials arranged in different forms under the natural influences of gravity and waterflow. Consequently, the angles of rest for particles are limited and the range of surface roughness values is small, hence, proglacial landforms are indistinguishable on surface roughness alone.

The dominant grain size results are the most interesting. It is shown that while predominantly pebble, cobble and boulder surfaces are indistinguishable at the C-band wavelength, there is distinct separation between the sand, granule and smooth bedrock surfaces when one particular grain size dominates. Figure 6.4 shows non overlap of the 95% confidence intervals of these fine grain sizes and smooth terrestrial surfaces. There is still confusion with these surfaces and the ice cap, therefore this concept could only be exploited in areas where the ice is absent or has been masked. The detectable surface

composition is dependent on the radar wavelength. For the C-band, with a λ of 5.6 cm, the roughness criterion calculates smooth to be less than 0.28 cm, intermediate to be 0.28 to 1.27 cm and rough to be greater than 1.27 cm. These results show that separable surfaces are smooth bedrock, sand surfaces with grain sizes of up to 0.19 cm, and granule surfaces with grain sizes of between 0.2 and 0.59 cm. According to the roughness criterion both bedrock and sand would be considered as smooth and granules would be considered intermediate. Grain sizes greater than these are not separable and amalgamated in the rough class. From these results it is suggested that there are further subdivisions of the smooth category defined by the Rayleigh criterion. However, it is acknowledged that these results are tentative due to the small sample sizes and superficial nature of the data. Further studies are needed with larger sample sizes, a method of quantification other than subjective visual estimates, grain size class divisions designed for the particular radar wavelength and quantitative analysis of moisture content, in order to explore the possible relationship between radar backscatter and dominant grain size composition.

These results indicate that, in certain situations, it may be possible to identify dominant grain size composition for surfaces using $\beta°$ values. This is a complete contradiction to the statement of Sabins (1987) that radar brightness alone cannot determine surface composition. Sabins' comment was made with reference to Seasat SAR data with a relatively long radar wavelength of 23.5 cm. A shorter wavelength, such as the C-band may prove to be more successful for this application. The importance of

grain size composition has already been highlighted in agricultural applications using soil texture (Dobson and Ulaby, 1981) and in large scale geological applications of radar, for example, Hanks and Guritz (1997) and Rudant *et al.* (1994), but has yet to be exploited for use in medium and small scale geomorphology.

9. Conclusion

A new approach to remote ice margin mapping has been presented using the definition 'limit of active ice', which takes into account spatial variation in ice front morphology. This method produces more accurate estimates of contemporary ice extent, as stagnant masses of ice along the margin are excluded from ice mass balance. In order to identify the limit of active ice, the ice marginal dynamics and their surficial expression must be fully understood. Once the nature of the limit has been established then the orbit characteristics of the sensor may be selected to highlight the features of interest. It has been shown that it is possible to extract the limit of active ice from the Barnes Ice Cap, accurate to within 49 m, using only RADARSAT SAR imagery and a sequence of image processing, image classification and edge detection. For the Barnes Ice Cap the limit of active ice is characterised by interlinking sections of snowbed, ice cored debris ridge and supraglacial debris cover.

Overall classification accuracies for the ice marginal environment are between 43% and 57%, and kappa coefficients are on the border between good and poor. The radar imagery has success with the morphology of the ice front, overall accuracies of the ice marginal features are approximately 70%, but has difficulty identifying proglacial landforms. The classifier can distinguish between ice and rough terrestrial surfaces such as residuum, but is unable to differentiate ice from smooth terrestrial surfaces. Proglacial deposits such as kames and alluvium, and smooth bedrock surfaces are frequently

confused with each other, and with the ice surface. Despite this misclassification it is possible to delineate the limit of active ice as it is separated spatially from the smooth proglacial surfaces by other landcover classes such as snowbeds, supraglacial debris and an elevated ice-cored debris ridge.

Radar image processing used the enhanced Frost filter for the removal of image speckle in preparation for texture analysis. Investigations concluded that the texture window should be as large as the smallest feature it is hoped to detect for optimum class discrimination. For 25 m spatial resolution imagery this is a texture window of 87.5 x 87.5 m and for 8 m spatial resolution imagery this window is 84.5 x 84.5 m. Linear features of the ice marginal environment are much longer and so larger texture windows are used for the correlation measure, 187.5 x 187.5 m and 162.5 x 162.5 m, for the standard and fine mode images respectively. Of the six texture measures investigated it was found that second order mean was the most useful for class discrimination, correlation was the second most useful, contrast and homogeneity produced similar results and variance and ASM were poor. Input classification variables were chosen in order that they provide complementary information about features and the most normal training data distributions, as are required by the maximum likelihood classifier. The selected input variables were mean, correlation and homogeneity.

Comparisons of orbital characteristics reveal that 'downglacier' illumination conditions produce the highest classification accuracies of ice marginal features. The

only problem associated with this image is a small spurious ice polygon adjoined to the margin. This occurs where a large supraglacial stream cuts through the ice cored debris ridge, and links a section of misclassified alluvium and bedrock surfaces to the ice cap. The descending image with illumination from an 'off ice, upglacier' perspective, has higher classification accuracies of proglacial landforms and is not subject to this spurious ice edge, however, it has a slightly lower accuracy of supraglacial debris classification due to shadowing behind the ice cored debris ridge.

The classification accuracies show a decrease in the accuracy of the fine mode image compared to the standard mode imagery. It appears to be particularly difficult to classify the supraglacial debris cover in the fine image. The benefits of increased classification accuracy and greater areal coverage offered by the standard mode imagery make this the obvious choice for ice margin mapping studies using RADARSAT data.

A secondary objective of this study examined surface roughness and radar brightness differences between proglacial landforms. Terrain templet measurements were used with some success to quantify surface height variation of features. The results indicate overlap in the roughness of proglacial landforms composed of similar grain sizes, such as kames, the L&A moraines and alluvium and, surprisingly, ice surfaces which produce surface roughness values similar to those of residuum. An investigation of dominant grain size and radar brightness shows that surfaces which are predominantly smooth bedrock, sands or granules produce markedly different radar responses.

Therefore, although it is not possible to distinguish between landforms, it may be possible to make inferences about dominant surface grain size composition using radar brightness alone.

10. References

Adam, S., A. Pietroniro and M. Brugman, 1997, Glacier snow line mapping using ERS-1 SAR imagery, *Remote Sensing of the Environment*, 61:46-54

Alparone, L., G. Benelli and A. Vagniluca, 1990, Texture-based analysis techniques for the classification of radar images, *IEEE Proceedings*, 137, Part F(4):276-282.

Altese, E., O. Bolognani, M. Mancini and P. Troch, 1996, Retrieving soil moisture over bare soil from ERS-I synthetic aperture radar data: sensitivity analysis based on a theoretical surface scattering model and field data, *Water Resources Research*, 32(3):653-661.

Andrews, J. and D. Barnett, 1979, Holocene (neoglacial) moraine and proglacial lake chronology, Barnes Ice Cap, Canada, *Boreas*, 8:341-358.

Baird, P., W. Ward and S. Orvig, 1952, The glaciological studies of the Baffin Island expedition, 1950, *Journal of Glaciology*, 2:2-23.

Baraldi, A. and F. Parmiggiani, 1995, An investigation of the textural characteristics associated with grey level cooccurrence matrix statistical parameters, *IEEE Transactions on Geoscience and Remote Sensing*, 33(2):293-304.

Barber, D. and E. LeDrew, 1991, SAR sea ice discrimination using texture statistics: a multivariate approach, *Photogrammetric Engineering and Remote Sensing*, 57(4):385-395.

Barber, D., M. Shokr, R. Fernandes, E. Soulis, D. Flett and E. LeDrew, 1993, A comparison of second order classifiers for SAR sea ice discrimination, *Photogrammetric Engineering and Remote Sensing*, 59(9):1397-1408.

Barnett, D., 1967, Development, landforms and chronology of Generator Lake, Baffin Island, N.W.T., *Geographical Bulletin*, 9(3):169-188.

Benallegue, M., O. Taconet, D. Vidal-Madjar and M. Normand, 1995, The use of radar backscattering signals for measuring soil moisture and surface roughness, *Remote Sensing of the Environment*, 53:61-68.

Benson, C., 1962, Stratigraphic studies in the snow and firn of the Greenland Ice Sheet, *SIPRE Research Report*, 70.

Bindschadler, R., K. Jezek and J. Crawford, 1987, Glaciological investigations using the synthetic aperture radar imaging system, *Annals of Glaciology*, 9:11-19.

Bindschadler, R. and P. Vornberger, 1992, Interpretation of SAR imagery of the Greenland ice sheet using coregistered TM imagery, *Remote Sensing of the Environment*, 42:167-175.

Brugman, M., A. Pietroniro and J. Shi, 1996, Mapping alpine snow and ice using Landsat TM and SAR imagery at Wapta Icefield, *Canadian Journal of Remote Sensing*, 22(1):127-136.

Campbell, J. B., 1981, Spatial autocorrelation effects upon accuracy of supervised classification of land cover, *Photogrammetric Engineering and Remote Sensing*, 47:355-363.

Campbell, B. and J. Garvin, 1993, Lava flow topographic measurements for radar data interpretation, *Geophysical Research Letters*, 20(9):831-834.

Carr, J., 1996, Spectral and textural classification of single and multiple band digital images, *Computers and Geosciences*, 22(8):849-865.

Conners, R. and C. Harlow, 1980, A theoretical comparison of texture algorithms, *IEEE Transactions on Pattern Analysis and Machine Intelligence*, PAMI-2(3):204-222.

Davis, W. and F. Peet, 1977, A method of smoothing digital thematic maps, *Remote Sensing of the Environment*, 6:45-49.

Dillworth, M., 1991, Geographic windows in remote sensing: does window size matter?, *ASPRS/ACSM Annual Convention Technical Papers*, 3:122-128.

Dillworth, M., J. Whistler and J. Merchant, 1994, Measuring landscape structure using geographic and geometric windows, *Photogrammetric Engineering and Remote Sensing*, 60(10):1215-1224.

Dobson, M. and F. Ulaby, 1981, Microwave backscatter dependence on surface roughness, soil moisture, and soil texture: part III - soil tension, *IEEE Transactions on Geoscience and Remote Sensing*, GE-19(1):51-61.

Dodd, N., 1987, Multispectral texture synthesis using fractal concepts, *IEEE Transactions on Pattern Analysis and Machine Intelligence*, PAMI-9:703-707.

Donald, J., F. Seglenicks, E. Soulis, N. Kouwen and D. Mullins, 1993, Mapping partial snowcover during the melt season using C-band SAR imagery, *Canadian Journal of Remote Sensing*, 19(1):68-76.

Dreimanis, A., 1971, Procedures of till investigations in North America, in Goldthwait R. P. (ed), *Till, a symposium*, Ohio State University Press, :27-37.

Drewery, D. J., 1986, *Glacial Geologic Processes*, Edward Arnold, London, UK

Durand, J., B. Gimonet and J. Perbos, 1987, SAR data filtering for classification, *IEEE Transactions on Geoscience and Remote Sensing*, GE-25(5): 629-637.

Dyke, A. S., 1993, Landscapes of cold-centred late Wisconsinan ice caps, Arctic Canada, *Progress in Physical Geography*, 17(2):223-247.

Ehrhard, D. G., R. Easton Jr., J. Schott and M. Comeau, 1993, Frequency-domain texture features for classifying SAR images, *Proceedings of SPIE's OE/Aerospace and Remote Sensing, 1993, Orlando, Florida*, 1960(3):21-32.

Fahnestock, M. A. and R. A. Bindschadler, 1993, Description fo a SAR investigation of the Greenland ice sheet and an example of margin change detection using SAR, *Annals of Glaciology*, 17:332-336.

Fisher, P. and S. Pathirana, 1990, The evaluation of fuzzy membership of land cover classes in the suburban zone, *Remote Sensing of the Environment*, 34:121-132.

Fitzgerald, R. W. And B. G. Lees, 1994, Assessing the classification of accuracy of multisource remote sensing data, *Remote Sensing of the Environment*, 47:362-368.

Foody, G. and N. Trodd, 1993, Non-classificatory analysis and representation of heathland vegetation from remotely sensed imagery, *GeoJournal*, 29(4):343-350.

Foody, G., M. McCulloch and W. Yates, 1994, Crop classification from C-band polarimetric data, *International Journal of Remote Sensing*, 15(4):2871-2885.

Forster, R., A. Klein, T. Blodgett and B. Isacks, 1993, Glaciological studies in the Central Andes using AIRSAR/TOPSAR, *Summaries of the 4th Annual J.P.L. Geoscience Workshop Oct. 25th-29th*, AIRSAR Workshop, 3:13.

Franklin, S and D. Peddle, 1987, Texture analysis of digital image data using spatial cooccurrence, *Computers and Geosciences*, 13(3):293-311.

Frost, V. S., J. A. Stiles, K. S. Shanmugan and J. C. Holtzman, 1982, A model for radar images and its application to adaptive digital filtering of multiplicative noise, *IEEE Transactions Pattern Analysis and Machine Intelligence*, 4(2):157-166.

Frost, V. S. and L. S. Yurovsky, 1985, Maximum likelihood classification of synthetic aperture radar imagery, *Computer Vision, Graphics and Image Processing*, 32:291-313.

Gaddis, L., P. Mouginis-Mark and J. Hayashi, 1990, Lava flow surface textures: SIR-B radar image texture, field observations and terrain measurements, *Photogrammetric Engineering and Remote Sensing*, 56(2), p.211-224.

Galloway, M., 1975, Texture classification using grey level run lengths, *Computer Graphics and Image Processing*, 4:172-179.

Genderen, J. van, and U. Uiterwijk, 1987, A practical procedure for classifying digital imagery, *Proceedings of the 13th Annual Conference of the Remote Sensing Society*, University of Nottingham, 287-296.

Goldthwait, R. P., 1951, Development of end moraines in east-central Baffin Island, *Journal of Geology*, 59:567-577.

Gong, P. and P. Howarth, 1990, The use of structural information for improving land-cover classification accuracies at the rural-urban fringe, *Photogrammetric Engineering and Remote Sensing*, 56(1):67-73.

Gonzalez, R. and R. Woods, 1992, *Digital Image Processing*, Addison-Wesley Publishing Company, Reading, Massachusetts.

Gray, A. L., K. E. Mattar, P.W. Vachon, R. Bindschadler, K. Jezek,, R. Forster and J. P Crawford, 1998, InSAR results from the RADARSAT Antarctic Mapping Mission data: estimation of glacier motion using a simple registration procedure, in Jezek, K. (ed.), Early Results from the First RADARSAT Antarctic Mapping Mission, *BPRC Technical Report No. 98-02*, Byrd Polar Research Center, The Ohio State University, Columbus, Ohio, 10-11.

Hall, D. and J. Ormsby, 1983, Use of SEASAT synthetic aperture radar and Landsat Multispectral Scanner subsystem data for Alaskan glaciology studies, *Journal of Geophysical Research*, 88(C3):1597-1607.

Hall, D. J. Ormsby, R. Bindschadler and H. Siddalingaiah, 1987, Characterisation of snow and ice reflectance zones on glaciers using Landsat Thematic Mapper data, *Annals of Glaciology*, 9:104-108.

Hall, D., K. Bayr and W. Kovalick, 1989, Determination of glacier mass balance using Thematic Mapper data, *Proceedings of the Eastern Snow Conference*, Lake Placid, New York, 7th - 9th June :192-196.

Hall, D., R. Williams Jr. and K. Bayr, 1992, Glacier recession in Iceland and Austria, *Eos Transactions of American Geophysical Union*, 73(12):129-144.

Hall, D., D. Williams Jr. and O. Sigurdsson, 1995, Glaciological investigation of Brúarjökull, Iceland, using synthetic aperture radar and thematic mapper satellite data, *Annals of Glaciology*, 21:371-377.

Hambrey, M. and J. Alean, 1992, *Glaciers*, Cambridge University Press, Cambridge.

Hambrey, M., 1994, *Glacial Environments*, UCL Press, London.

Hanks, C. and R. Guritz, 1997, Use of Synthetic Aperture Radar (SAR) for geological reconnaissance in Arctic regions: an example from the Arctic National Wildlife Refuge, Alaska, *American Association of Petroleum Geologists Bulletin*, 81(1):121-134.

Haralick, R. M., 1979, Statistical and structural approaches to texture, *Proceedings of the IEEE*, 67(5):786-804.

Haralick, R. M., K. Shanmugan and I. Dinstein, 1973, Textural features for image classification, *IEEE Transactions on Systems, Man and Cybernetics*, 6:610-621.

Hart, J. K. 1994, Proglacial glaciotectonic deformation at Melabakkar-Asbakkar, west Iceland, *Boreas*, 23:112-121.

Hart, J. K. 1995, Drumlins, flutes and lineations at Vestari-Hagafellsjökull, Iceland, *Journal of Glaciology*, 41:596-606.

Hepner, G., T. Logan, N. Ritter and N. Bryant, 1990, Artificial neural network classification using a minimal training data set: a comparison to conventional supervised classification, *Photogrammetric Engineering and Remote Sensing*, 56(4):469-473.

Holdsworth, G., 1973, Evidence of a surge on Barnes Ice Cap, Baffin Island, *Canadian Journal of Earth Sciences*, 10:1565-1574.

Holdsworth, G., 1977, Surge activity on the Barnes Ice Cap, *Nature*, 269:587-590.

Holmes, Q., D. Nuesch and R. Schuchman, 1984, Texture analysis and real time classification of sea-ice types using digital SAR data, *IEEE Transactions on Geoscience and Remote Sensing*, GE-22:113-120.

Hooke, R. Le B, 1973, Flow near the margin of the Barnes Ice Cap, and development of ice cored moraines, *Geological Society of America Bulletin*, 84:3929-3948.

Hooke, R. Le B., G. Johnson, K. Brugger, B. Hanson and G. Holdsworth, 1987, Changes in mass balance, velocity and surface profile along a flow line on Barnes Ice Cap, 1970-1984, *Canadian Journal of Earth Sciences*, 24:1550-1561.

Houghton, J., L. Meira Filho, B. Callander, N. Harris, A. Kattenberg and K. Maskell (eds.), 1996, *Climate Change 1995: The Science of Climate Change*, Second Assessment Report of the Intergovernmental Panel on Climate Change, Cambridge University Press, Cambridge.

Hsu, S., 1978, Texture-tone analysis for automated land use mapping, *Photogrammetric Engineering and Remote Sensing*, 44(11):1393-1404.

Ives, J. D. and J. T. Andrews, 1963, Studies in the physical geography of north-central Baffin Island, N.W.T, *Geographical Bulletin*, 19:5-48.

Jacobs, J. D., R. Heron and J. E. Luther, 1993, Recent changes at the northwest margin of the Barnes Ice Cap, *Arctic and Alpine Research*, 25(4):341-352.

Jacobs, J. D., É. L. Simms and A. Simms, 1997, Recession of the southern part of the Barnes Ice Cap, Baffin Island, Canada, between 1961 and 1993, determined from digital mapping of Landsat TM, *Journal of Glaciology*, 43(143):98-102.

Jensen, J., 1996, *Introductory Digital Image Processing: A remote Sensing Perspective*, second edition, Prentice-Hall, Upper Saddle River, New Jersey.

Jezek, K., M. Drinkwater, J. Crawford, R. Bindschadler and R. Kwok, 1993, Analysis of synthetic aperture radar data collected over the southwestern Greenland Ice Sheet, *Journal of Glaciology*, 39(131):119-132.

Krimmel, R. and M. Meier, 1975, Glacier applications of ERTS images, *Journal of Glaciology*, 15:391.

Kuan, D. T., A. A. Sawchuk, T. C. Strand and P. Chavel, 1987, Adaptive restoration of images with speckle, *IEEE Trans. ASSP.*,35(3):373-383.

Kushwaha, S., S. Kuntz and G. Oesten, 1994, Applications of image texture in forest classification, *International Journal of Remote Sensing*, 15(11):2273-2284.

Landis, J. and G. Koch, 1977, The measurement of observer agreement for categorical data, *Biometrics*, 33:159-174.

Lee, J. S., 1980, Digital image enhancement and noise filtering by the use of local statistics, *IEEE Transactions on Pattern Analysis and Machine Intelligence*, PAMI-2(2), March.

Lillesand, T. M. and R. W. Kiefer, 1994, *Remote Sensing and Image Interpretation*, third edition, John Wiley & Sons, New York.

Lindholm, R., 1987, *A Practical Approach to Sedimentology*, Allen and Unwin, London.

Liu, S. and S. Chang, 1997, Dimension estimation of discrete-time fractal Brownian motion with applications to image texture classification, *IEEE Transactions on Image Processing*, 6(8):1176-1184.

Løken, O. H. and J. T. Andrews, 1966, Glaciology and chronology of fluctuations of the ice margin at the south end of the Barnes Ice Cap, Baffin Island, N.W.T., *Geographical Bulletin*, 8(4):341-359.

Loor, G. P., de, 1968, Dielectric properties of heterogeneous mixtures containing water, *Journal of Microwave Power*, 3:67-73.

Lopes, A, R. Touzi and E. Nezry, 1990, Adaptive speckle filters and scene heterogeneity, *IEEE Transactions on Geoscience and Remote Sensing*, 28(6):992-1000.

Lopes, A., E. Nezry, R. Touzi and H. Laur, 1993, Structure detection and statistical adaptive speckle filtering in SAR images, *International Journal of Remote Sensing*, 14(9):1735-1758.

Massom, R., 1991, *Satellite Remote Sensing of Polar Regions*, Belhaven Press, London.

Mastin, G., 1985, Adaptive filters for digital image noise smoothing: an evaluation, *Computer Vision, Graphics and Image Processing*, 31:103-121.

Mather, P., 1985, A computationally efficient maximum likelihood classifier employing prior probabilities for remotely sensed data, *International Journal of Remote Sensing*, 6(2):369-376.

Maxfield, A. W., 1994, Radar satellite snowmelt detection in the Canadian Rocky Mountains, in Stein, T. (ed), *Proceedings of IGARSS '94, Surface and Atmospheric Remote Sensing: Technologies, Data Analysis and Interpretation, Pasadena, California, August 8-12, 1994*, Institute of Technology, California, USA, 4:2074-2077.

Mohr, J. J., 1997, Repeat track SAR interferometry; an investigation of its utility for studies of glacier dynamics, *Ph.D. thesis, LD 125, Technical University of Denmark,* Copenhagen, Denmark.

Nezry, E., A. Lopes, D. Ducrot-Gambart, C. Nezry and J. Lee, 1996, Supervised classification of K-distributed SAR images of natural targets and probability of error estimation, *IEEE Transactions on Geoscience and Remote Sensing,* GE-34(5):1233-1242.

Nye, J. F., 1957, The distribution of stress and velocity in glaciers and ice sheets, *Royal Society of London Proceedings,* 239A:113-133.

Orheim, O. and B. K. Lucchitta, 1987, Snow and ice studies by thematic mapper and multispectral scanner Landsat images, *Annals of Glaciology,* 9:109-118.

Østrem, G., 1975, ERTS data in glaciology - an effort to monitor glacier mass balance from satellite imagery, *Journal of Glaciology,* 15(73):403-415.

Parrot, J., N. Lyberis, B. Lefaueonnier and G. Manby, 1993, SPOT multispectral data and digital terrain model for the analysis of ice-snow fields on arctic glaciers, *International Journal of Remote Sensing,* 14(3)425-440.

Paterson, W., 1994, *The Physics of Glaciers,* third edition, Pergamon Press, New York.

Peake, W. and T. Oliver, 1971, *The response of terrestrial surfaces at microwave frequencies,* Ohio State University Electroscience Laboratory, 2440-7, Technical Report AFAL-TR-70-301, Columbus, Ohio.

Pultz, T., and R. Brown, 1987, SAR image classification of agricultural targets using first- and second-order statistics, *Canadian Journal of Remote Sensing,* 13(2):85-91.

Rand, R., 1985, *Texture analysis and cartographic feature extraction,* US Army Corps of Engineer Topographic Laboratories, Technical Report ETL-0370, AD-A 159 220, Fort Belvoir, Virginia.

Rees, W. G., 1990, *Physical Principles of Remote Sensing,* Cambridge University Press, Cambridge.

Rees, W. and V. Squire, 1989, Review article: technological limitations to satellite glaciology, *International Journal of Remote Sensing,* 10(1):7-22.

Rees, W., J. Dowdeswell and A. Diament, 1995, Analysis of ERS-1 synthetic aperture radar data from Nordaustlandet, Svalbard, *International Journal of Remote Sensing*, 16(5):905-924.

Rignot, E., R. Forster and B. Isacks, 1996, Interferometric radar observations of Glacier San Rafeal, Chile, *Journal of Glaciology*, 42:279-291.

Rignot, E., S. Gogineni, W. Krabill and S. Ekholm, 1997, North and northwest Greenland ice discharge from satellite interferometry, *Science*, 276(May):934-937.

Rosenfield, G. and K. Fitzpatrick-Lins, 1986, A coefficient of agreement as a measure of thematic classification accuracy, *Photogrammetric Engineering and Remote Sensing*, 52(2):223-227.

Rott, H., 1984 Synthetic aperture radar capabilities for snow and glacier monitoring, *Advances in Space Research*, 4(11):241-246.

Rott, H. and C. Mätzler, 1987, Possibilities and limits of synthetic aperture radar for snow and glacier surveying, *Annals of Glaciology*, 9:195-199.

Rott, H. and T. Nagler, 1993, Snow and glacier investigations by ERS-1 SAR - first results, in Kaldeich B. (ed), *Proceedings of the First ERS-1 Symposium Space at the Service of our Environment, 4-6 November 1992, Cannes, France*, European Space Agency Special Publication SP-359, Paris, 2:577-582

Rotunno F., O., P. Treitz, E. Soulis, P. Howarth and N. Kouwen, 1996, Texture Processing of radar data using second-order spatial statistics, *Computers and Geosciences*, 22(1):27-34.

Rudant, J., J. Deroin and L. Polidori, 1994, Multi-resolution analysis of radar images and its application to lithological and structural mapping; Larzac (southern France) test site, *International Journal of Remote Sensing*, 15(12):2451-2468.

Sabins, F., Jr., 1987, *Remote Sensing Principles and Interpretation, Second Ed.*, W. H. Freeman and Company, New York.

Sagar, R., 1966, Glaciological and climatological studies on the Barnes Ice Cap, 1962 - 64, *Geographical Bulletin*, 8(1):3-47.

Schaber, G., G. Berlin and W. Brown, 1976, Variations in surface roughness within Death Valley, California: geologic evaluation of 25 cm wavelength radar images, *Geological Society of America Bulletin*, 87:29-41.

Schott, J., 1997, *Remote Sensing: The Image Chain Approach*, Oxford University Press, Oxford.

Schowengerdt, R. 1983, *Techniques for Image Processing and Classification in Remote Sensing*, Academic Press, New York.

Shanmugan, S., V. Narayanan, V. Frost, J. Stiles and J. Holtzman, 1981, Textural features for radar image analysis, *IEEE Transactions on Geoscience and Remote Sensing*, GE-19(3):153-156.

Shaw, J. 1994, A qualitative view of sub-ice-sheet landscape evolution, *Progress in Physical Geography*, 18(2):159-184.

Shi, J. and J. Dozier, 1993, Measurements of snow- and glacier-covered areas with single-polarisation SAR, *Annals of Glaciology*, 17:.72-76.

Shi, Z. and Ko. B. Fung, 1994, A comparison of digital speckle filters, *Proceedings of IGRASS 94*, August 8-12, IV:2129-2131.

Shi, J., J. Dozier and H. Rott, 1994, Snow mapping in alpine regions with synthetic aperture radar, *IEEE Transactions on Geoscience and Remote Sensing*, GE-32(1):152-157.

Shokr, M., 1991, An evaluation of second-order textural parameters for sea ice classification in radar images, *Journal of Geophysical Research*, 96(C6):10625-10640.

Skvarca, P., H. Rott and T. Nagler, 1995, Satellite imagery, a base line for glacier variation study on James Ross Island, Antarctica, *Annals of Glaciology*, 21

Small, A.J. 1983, Lateral moraines of Glacier Tsijore Nouve: form development and implications, *Journal of Glaciology*, 29:250 -259.

Smith, L., R. Forster, B. Isacks and D. Hall, 1997, Seasonal climatic forcing of alpine glaciers revealed with orbital synthetic aperture radar, *Journal of Glaciology*, 43(145):480-488.

Sohn, H-G., 1996, Boundary detection using multisensor imagery: application to ice sheet margin detection, *Ph.D. Thesis, Ohio State University*, Columbus, Ohio.

Sohn, H-G, and K. Jezek, 1996, Automatic approach to detect ice sheet margin using ERS-1 synthetic aperture radar imagery, *International Archives of Photogrammetry and Remote Sensing*, volume XXXI, part B7, Vienna.

Stewart, C., B. Moghaddam, K. Hintz and L. Novak, 1993, Fractal Brownian motion models for synthetic aperture radar imagery scene segmentation, *IEEE Proceedings*, 81:1511-1522.

Strahler, A., 1980, the use of prior probabilities in maximum likelihood classification of remotely sensed data, *Remote Sensing of the Environment*, 10:135-163.

Stromberg, W. and T. Farr, 1986, A Fourier-based textural feature extraction procedure, *IEEE Transactions on Geoscience and Remote Sensing*, GE-24(5):722-731.

Sugden, D. E., 1978, Glacial erosion by the Laurentide Ice Sheet, *Journal of Glaciation*, 20:367-391.

Sugden, D.E and B.S. John, 1976, *Glaciers and Landscape*, Edward Arnold, London, p.256.

Sun, C. and W. Wee, 1982, Neighbouring grey level dependence matrix for texture classification, *Computer Vision, Graphics and Image Processing*, 23:341-352.

Swain, P. and S. Davis, (eds), 1978, *Remote Sensing: The Quantitative Approach*, McGraw-Hill Inc., New York.

Swain, P. H., 1978. "Fundamentals of pattern recognition in remote sensing", In P. H. Swain and S. M. Davies, eds, *Remote Sensing: The Quantitative Approach*, McGraw-Hill, New York.

Tatenhove, F. G. van, 1996, Changes in morphology at the margin of the Greenland Ice Sheet (Leverett Glacier), in the period 1943-1992: a quantitative analysis, *Earth Surface Processes and Landforms*, 21:797-816

Thorsteinsson, R. and E. Tozer, 1976, Geology of the Arctic Archipelago, in Douglas, R. (ed) *Geology and Economic Minerals of Canada*, Part B (Chapters VIII - XIII and Index), Geological Survey of Canada, Department of Energy, Mines and Resources, Ottawa.

Thomas, R., 1983, Ice sheets, in, Gurney R., J. Foster and C. Parkinson (eds), *Atlas of Satellite Observations Related to Global Change*, Cambridge University Press, Cambridge, U.K.

Ulaby, F., P. Batlivala amd M. Dobson, 1978, Microwave backscatter dependence on surface roughness, soil moisture and soil texture: part 1 - bare soil, *IEEE Transactions on Geoscience and Remote Sensing*, GE-16(4):286-295.

Ulaby, F., F. Kouyate, B. Brisco and T. Lee Williams, 1986, Textural information in SAR images, *IEEE Transactions on Geoscience and Remote Sensing*, GE-24(2):235-245.

Vincent, R., 1997, *Fundamentals of Geological and Environmental Remote Sensing*, Prentice-Hall Inc., Upper Saddle River, New Jersey.

Vornberger, P. and R. Bindschadler, 1992, Multispectral analysis of ice sheets using co-registered SAR and TM imagery, *International Journal of Remote Sensing*, 13(4):637-645.

Wang, L. and D. He, 1990, A new statistical approach for texture analysis, *Photogrammetric Engineering and Remote Sensing*, 56(1):61-66.

Weeks, R., M. Smith, Kyung Pak, Wen-Hai Li, A. Gillespie and B. Gustafson, 1996, Surface roughness, radar backscatter, and visible and near-infrared reflectance in Death Valley, California, *Journal of Geophysical Research*, 101(E10):23,077 -23,090.

Weertman, J., 1961, Mechanism for the formation of inner moraines found near the edge of cold ice caps and ice sheets, *Journal of Glaciology*, 3(30):965-978.

Weska, J. S., C. R. Dyer and A. Rosenfeld, 1976, A comparative study of texture measures for terrain classification, *IEEE Transactions on Systems, Man and Cybernetics*, SMC-6 (4):269-285.

Williams, R. S. Jr, D. K. Hall and C. S. Benson, 1991, Analysis of glacier facies using satellite techniques, *Journal of Glaciology*, 37(125) :120-127.

Wilson, J. D., 1992, A comparison of procedures for classifying remotely-sensed data using simulated data sets incorporating autocorrelations between spectral responses, *International Journal of Remote Sensing*, 13(14):2701-2725.

Wong, Y. and Posner, E. C., 1993, A new clustering algorithm applicable to multispectral and polarimetric SAR images, *IEEE transactions on Geoscience and Remote Sensing*

Woodcock, C. and A. Strahler, 1987, The factor of scale in remote sensing, *Remote Sensing of the Environment*, 21(3):311-322.

11. Data source list

Aerial Photographs, 1958, Flight line A-16344, #63-66, Department of Energy, Mines and Resources, Ottawa, Ontario.

Aerial Photographs, 1961, Flight line A-17043, #18-32, Department of Energy, Mines and Resources, Ottawa, Ontario.

Atmospheric Environment Service, 1996 and 1997, Surface Analysis Charts (Daily, 12Z), A.E.S Atlantic Region, Bedford, Nova Scotia.

NTS Map Sheet, Gee Lake, District of Franklin, NWT., 1967, UTM Zone 18 W, NAD 27, Sheet #37 D/16, Surveys and Mapping Branch, Department of Energy, Mines and Resources, Ottawa, Ontario.

NTS Map Sheet, Sam Fiord River, District of Franklin, NWT., 1967, UTM Zone 19 W, NAD 27, Sheet #27 C/13, Surveys and Mapping Branch, Department of Energy, Mines and Resources, Ottawa, Ontario.

RADARSAT Image, 1996, Barnes Ice Cap, Baffin Island, Aug. 6th, S4 DESC., Product ID # M0062745, ADRO project #303, RADARSAT International, Richmond, BC; CD-ROM.

RADARSAT Image, 1997, Barnes Ice Cap, Baffin Island, July 26th, S4 ASC., Product ID # M0122606, ADRO project #303, RADARSAT International, Richmond, BC; CD-ROM.

RADARSAT Image, 1997, Bight, Aug. 12th, F1 ASC., Product ID # M0126935, ADRO project #303, RADARSAT International, Richmond, BC; CD-ROM.